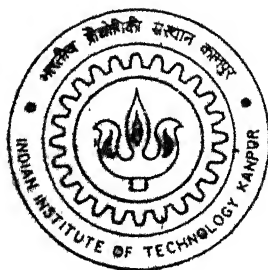


SINTERING AND ELECTROCHEMICAL CHARACTERIZATION OF YTTRIA-DISPERSED AUSTENITIC AND FERRITIC STAINLESS STEELS

By

SHANKAR. J



DEPARTMENT OF MATERIALS AND METALLURGICAL ENGINEERING

Indian Institute of Technology Kanpur

MARCH, 2002

SINTERING AND ELECTROCHEMICAL CHARACTERIZATION OF YTTRIA-DISPERSED AUSTENITIC AND FERRITIC STAINLESS STEELS

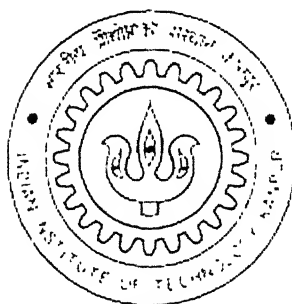
A Thesis Submitted

In Partial Fulfillment of the Requirements
For the Degree of

MASTER OF TECHNOLOGY

by

**SHANKAR. J
(YO10636)**



to the

**DEPARTMENT OF MATERIALS AND METALLURGICAL
ENGINEERING**

**INDIAN INSTITUTE OF TECHNOLOGY
KANPUR**

4 FEB 2003 / NME

पुरुषोत्तम काशीनाथ केसकर पुस्तकालय

भारतीय प्रौद्योगिकी संस्थान कानपुर

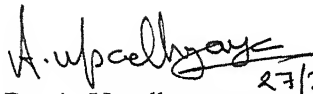
अवाप्ति क्र० A **141869**



A141869

CERTIFICATE

It is certified that the work contained in the thesis entitled “**SINTERING AND ELECTROCHEMICAL CHARACTERIZATION OF YTTRIA-DISPERSED AUSTENITIC AND FERRITIC STAINLESS STEELS** ” by **Shankar. J (Roll No. Y010636)**, has been carried out under our supervision and to the best of our knowledge this work has not been submitted elsewhere for a degree.

 27/2/02

Dr. A. Upadhyaya


Assistant Professor

Department of Materials and

Metallurgical Engineering.

Indian Institute of Technology,

Kanpur.

 27 Feb 02

Dr. R. Balasubramaniam

Professor

Department of Materials and

Metallurgical Engineering.

Indian Institute of Technology,

Kanpur.

Abstract

Present work is focused on sintering of stainless steels and their particulate composites containing yttria as the particulate particles. The research is mainly focused on the ferritic stainless steels (434L) and austenitic stainless steels (316L). Sintering is carried out by two techniques, solid state sintering and supersolidus liquid phase sintering. Supersolidus liquid phase sintering is a novel method of sintering applicable to this system to get certain properties, which are not achieved by normal solid state sintering. P/M stainless steels are used mainly in automotive industry for making corrosion resistant products. This work is carried out to improve the mechanical properties of the automotive components by mixing yttria particulate particles. Moreover the properties of ferritic and austenitic stainless steels were compared in the research. The composites were pressed at 600MPa pressure, which was selected by earlier research on the effect of pressure. Characterization of the sintered product was carried out by metallography (both optical and scanning electron microscopy) and electrochemical studies. During characterization main emphasis was given to the effect of temperature and yttria content in the sintering behavior and microstructural evolution of the composites.

As mentioned earlier these materials are used in automotive components where the corrosion atmosphere is mild. Hence the electrochemical studies were carried out in 0.05 mol/l ($\text{pH} = 1$) sulfuric acid. Potentiodynamic polarization was carried out in order to understand the passive film properties. More emphasis was given to study the passive film nature and hence the samples were subjected to electrochemical impedance spectroscopy (EIS). Tafel extrapolation was carried out to determine the corrosion rate of the P/M samples. Finally cyclic polarization experiments were carried out in 3.56 weight percent sodium chloride solution (sea water) in order to determine the pitting resistance of the sample.

Table of Contents

List Of Figures	vi
List Of Tables	ix
Acknowledgement	x
1. INTRODUCTION	1
2. BACKGROUND	3
2.1. Stainless Steel	3
2.1.1. Selection Of Stainless Steel	9
2.1.2. Corrosion Of Stainless Steel	9
2.2. Electrochemical Corrosion	12
2.3. Polarization	13
2.3.1. Linear Polarization	17
2.3.2. Tafel Extrapolation	20
2.3.3. Potentiodynamic Polarization	21
2.3.4. Cyclic Polarization	25
2.4. Powder Metallurgy	27
2.4.1. Advantages Of Powder Metallurgy	28
2.4.2. Limitations Of Powder Metallurgy	30
2.4.3. Applications Of Powder Metallurgy	31
2.5. Sintering	31
2.6. Solid State Sintering	35
2.7. Liquid Phase Sintering	42
2.8. Supersolidus Liquid Phase Sintering	47
2.8.1. Previous Research On Slps	50

2.8.2. Parameters Affecting Slps	52
2.9. P/M Stainless Steels	55
2.10. Corrosion Of P/M Stainless Steels	60
2.11. A Review Of P/M Stainless Steels	63
2.12. Staniless Steel Based Particulate Composites	67
3. SCOPE OF THE PRESENT WORK	70
4. EXPERIMENTAL PROCEDURE	72
4.1. Raw Materials	72
4.1.1. Stainless Steel Powders	72
4.1.2. Yttria Powder	73
4.2. Powder Characterization	73
4.2.1. Particle Size And Size Distribution	73
4.2.2. Particle Shape	74
4.3. Premix Preparation	74
4.4. Compaction	79
4.5. Sintering	79
4.6. Densification Behavior	82
4.6.1. Density And Densification Parameter	82
4.6.2. Linear And Radial Shrinkage	82
4.7. Microstructural Studies	83
4.7.1. Optical Microscopy	83
4.7.2. Scanning Electron Microscopy	83
4.8. Electrochemical Studies	85
4.8.1. Polarization Experiments	85

4.8.2. Tafel Extrapolation	86
4.8.3. Potentiodynamic Polarization	86
4.8.4. Cyclic Polarization	86
 5. EXPERIMENTAL RESULTS	 88
5.1. Sintering	88
5.1.1. Results	88
5.1.1.1. Densification Behavior	88
Density And Densification Behavior	88
Axial And Radial Shrinkage	92
Weight Loss	98
5.1.1.2. Microstructural Results	98
Optical Micrographs	98
Sem Micrographs	104
5.1.2. Discussions	110
5.1.2.1. Variation In Densification Behavior	116
5.1.2.2. Microstructural Studies	117
5.2. Corrosion	119
5.2.1. Potentiodynamic Polarization	119
5.2.2. Tafel Extrapolation	135
 6. CONCLUSIONS	 140
 REFERENCE	 142
 APPENDIX I	 146

APPENDIX II	147
APPENDIX III	148
APPENDIX IV	149
APPENDIX V	150
APPENDIX VI	153
APPENDIX VII	154
APPENDIX VIII	155
APPENDIX IX	156

List of Figures

- 1) Figure 2.1. Fe-Cr phase diagram [2].
- 2) Figure 2.2. Fe-Ni phase diagram [2].
- 3) Figure 2.3. Fe-Mo phase diagram [2].
- 4) Figure 2.4. Ternary phase diagram of stainless steel.
- 5) Figure 2.4. Various types of stainless steel [4].
- 6) Figure 2.5. Thermodynamic energy profile for metals and their compounds [8].
- 7) Figure 2.6. Basic wet corrosion cell [8].
- 8) Figure 2.7. Evans diagram for an active metal [1].
- 9) Figure 2.8. Various types of polarization methods [11].
- 10) Figure 2.9. Schematic diagram of a linear polarization plot [10].
- 11) Figure 2.10. Schematic diagram showing the potentiodynamic polarization for an active-passive metal [12].
- 12) Figure 2.11. Anodic polarization curves for hypothetical alloy A,B,C,D in 1) reducing 2) moderately oxidizing 3) highly oxidizing environments [1].
- 13) Figure 2.12. The schematic diagram of a cyclic polarization plot showing (a) negative hysteresis and (b) positive hysteresis [5].
- 14) Figure 2.14. Densification during compaction by changes in particle arrangement and shape [15].
- 15) Figure 2.15. Ideal application areas using P/M [17].
- 16) Figure 2.16. Map to various sintering processes [21].
- 17) Figure 2.17. Two sphere sintering model [17].
- 18) Figure 2.18. Possible sintering mechanisms at the neck area [15].
- 19) Figure 2.19. Schematic sketch showing various stages of sintering [15].
- 20) Figure 2.20. Three-sphere sintering models. (a) Original point contacts. (b) Neck growth. (c) and (d) Pore rounding [19].
- 21) Figure 2.21. Microstructure of sintered molybdenum showing internal porosity [19].
- 22) Figure 2.22. Ideal phase diagram for liquid phase sintering [21].
- 23) Figure 2.23. A map of density versus liquid content with indications of the dominant regions [21].
- 24) Figure 2.24. Microstructural evolution of classical liquid phase sintering [21].
- 25) Figure 2.25. SLPS of a prealloyed polycrystalline powder [21].
- 26) Figure 2.26. SEM micrograph of (a) Ni-base superalloy and (b) stainless steel showing liquid formation sites [24].
- 27) Figure 2.27. Variation of sintered density with temperature in a Ni based super alloy during supersolidus liquid phase sintering [22].
- 28) Figure 2.28. Binary phase diagram showing desired features for SLPS processing at composition X_A and temperature T [21].
- 29) Figure 2.29. Effect of holding time on sintered density during SLPS [21].
- 30) Figure 2.30. Typical examples of P/M stainless steel parts [37].
- 31) Figure 2.31. Surface of a P/M Stainless Steel Sample [29].
- 32) Figure 2.32. Possible corrosion mechanism in P/M stainless steels [55].
- 33) Figure 2.33. Microstructure showing (a) 316L stainless steel and (b) 316L/SiC composite [65].

- 34) Figure 4.1. Particle size analysis of Y_2O_3 .
- 35) Figure 4.2. Particle size analysis of 316L.
- 36) Figure 4.3. Particle size analysis of 434L.
- 37) Figure 4.4. SEM Picture of (a) Y_2O_3 agglomerate (b) single particle.
- 38) Figure 4.5. SEM micrograph of (a) 316L powder and (b) 434L powder.
- 39) Figure 4.6. Schematic diagram of a horizontal tubular furnace.
- 40) Figure 4.7. Schematic diagram showing the connections in the potentiostat.
- 41) Figure 4.8. Schematic Representation of (a) Flat Cell and (b) Round Cell.
- 42) Figure. 5.1. Variation of green density with compaction pressure.
- 43) Figure 5.2. Variation of sintered density with compaction pressure and sintering temperature.
- 44) Figure 5.3. Variation of densification parameter with compaction pressure and sintering temperature.
- 45) Figure 5.4. Variation of sintered density with addition of Y_2O_3 and temperature.
- 46) Figure 5.5. Variation of densification parameter with addition of Y_2O_3 and temperature.
- 47) Figure 5.6. Radial vs axial shrinkage with variation in pressure and temperature for 316L stainless steel samples.
- 48) Figure 5.7. Radial vs axial shrinkage with variation in pressure and temperature for 434L samples.
- 49) Figure 5.8. Radial vs axial shrinkage with variation in Y_2O_3 content and temperature of 316L composite samples.
- 50) Figure 5.9. Radial vs axial shrinkage with variation in Y_2O_3 content and temperature for 434L composite samples.
- 51) Figure 5.10. Variation Weight loss with compaction pressure and sintering temperature for 316L and 434L stainless steels.
- 52) Figure 5.11. Variation of weight loss with temperature and Y_2O_3 content for 316L and 434L stainless steel composites.
- 53) Figure 5.12. Optical micrograph of 316L P/M stainless steels sintered at (a) $1250^\circ C$ and (b) $1400^\circ C$ at 200X magnification. The samples were compacted at 600MPa.
- 54) Figure 5.13. Optical micrograph of 316L P/M stainless steels sintered at (a) $1250^\circ C$ and (b) $1400^\circ C$ at 500X magnification. The samples were compacted at 600MPa.
- 55) Figure 5.14. Optical micrograph of 316L+10-weight % Y_2O_3 P/M composite sintered at (a) $1250^\circ C$ and (b) $1400^\circ C$. The samples were compacted at 600MPa pressure.
- 56) Figure 5.15. Optical micrograph of 316L+10-weight % Y_2O_3 P/M composite sintered at (a) $1250^\circ C$ and (b) $1400^\circ C$. The samples were compacted at 600MPa pressure.
- 57) Figure 5.16. Optical micrographs of 434L stainless steels sintered at (a) $1250^\circ C$ and (b) $1400^\circ C$. The samples were compacted at 600 MPa pressure.
- 58) Figure 5.17. Optical micrograph of 316L+10% Y_2O_3 sintered at (a) $1250^\circ C$ and (b) $1400^\circ C$.

- 59) Figure 5.18. SEM micrograph of 316L+10% Y_2O_3 stainless steel composite sintered at 1250°C in (a) SE mode and (b) BSE mode showing the surface porosity.
- 60) Figure 5.19. SEM micrograph of 316L+10% Y_2O_3 stainless steel composite sintered at 1400°C in (a) SE mode and (b) BSE mode showing the surface porosity.
- 61) Figure 5.20. SEM micrograph of 316L+10% Y_2O_3 stainless steel composite sintered at (a) 1250°C and (b) 1400°C showing arrangement of Y_2O_3 at the surface.
- 62) Figure 5.21. SEM micrograph of 434L+10% Y_2O_3 sintered at 1250°C showing Y_2O_3 dispersions in (a) SE mode and (b) SE and BSE modes.
- 63) Figure 5.22. SEM micrograph of 434L+10% Y_2O_3 sintered at 1400°C showing Y_2O_3 dispersions in (a) SE mode and (b) BSE mode.
- 64) Figure 5.23. SEM micrograph of 434L+10% Y_2O_3 sintered at (a) 1250°C and (b) 1400°C showing the dispersion of Y_2O_3 on the surface.
- 65) Figure 5.24. Three different experiments of variation of ZCP vs time in 0.05 mol/l H_2SO_4 solution for 316L standard.
- 66) Figure 5.25. Potentiodynamic polarization curves for 430L standard, 434LP/M and 434L composites sintered at 1250°C.
- 67) Figure 5.26. Bode frequency plot at various potentials for 434L P/M stainless steel sintered at 1250°C.
- 68) Figure 5.27. Potentiodynamic polarization curves for 430L, 434L and 434L composites sintered at 1400°C.
- 69) Figure 5.28. Potentiodynamic polarization plots for 316L wrought, 316L P/M and 316L P/M composites sintered at 1250°C.
- 70) Figure 5.29. Potentiodynamic polarization plots for 316L wrought, 316L P/M and 316L composites sintered at 1400°C.
- 71) Figure 5.30. Estimation of Tafel slopes and corrosion rate, i_{corr} from the experimental data of the Tafel experiment.

List of tables

- 1) Table 2.1. Galvanic series of various metals and alloys in seawater [6].
- 2) Table 2.2. Standard reference electrode potentials [1].
- 3) Table 2.3. Comparison of P/M and competitive production techniques [19].
- 4) Table 2.4. Applications of powder metallurgy [19].
- 5) Table 2.5. Comparison of LPS and SLPS [25].
- 6) Table 2.6. Compositions of standard powder metallurgy stainless steel [14].
- 7) Table 2.7. Characteristics of various grades of P/M stainless steel [14].
- 8) Table 2.8. Applications of various grades of P/M stainless steel [14].
- 9) Table 4.1. The experimental variants used during compaction.
- 10) Table 5.1. Passivity parameters obtained for potentiodynamic polarization curves for 434L samples sintered 1250°C.
- 11) Table 5.2. Passivation parameters obtained for potentiodynamic polarization curves for 434L samples sintered at 1400°C.
- 12) Table 5.3. Passivation parameters obtained for potentiodynamic polarization curves for 316L wrought, 316L P/M and 316L P/M composites sintered at 1250°C.
- 13) Table 5.4. Potentiodynamic polarization data for 316L wrought, 316L P/M and 316L P/M composites sintered at 1400°C.
- 14) Table 5.5. Tafel extrapolation data for 430L wrought, 434L P/M and 434L P/M composites sintered at 1250°C.
- 15) Table 5.6. Tafel extrapolation data for 430L wrought, 434L P/M and 434L P/M composites sintered at 1400°C.
- 16) Table 5.7. Tafel extrapolation data for 316L wrought, 316L P/M and 316L P/M composites sintered at 1250°C.
- 17) Table 5.8. Tafel extrapolation data for 316L wrought, 316L P/M and 316L P/M composites sintered at 1400°C.

Acknowledgements

I would like to express my sincere gratitude to Dr. R. Balasubramaniam and Dr. A. Upadhyaya for their able guidance and support throughout my graduate study at Indian Institute of Technology. Their leaderships were immeasurable help to my early identification of an industrially significant area of research.

Special thanks are due to Dr. A.V. Ramesh Kumar, Electrochemistry and Corrosion Division, Defense Materials Stores Research and Development Establishment (DMSRDE), Kanpur for conducting the electrochemical impedance spectroscopic studies.

I would like to thank Dr. Mungole and Mr. Soni of the MME Department for their technical assistance and guidance during the present research work.

My time at IIT Kanpur was enriched by my laboratory mates Laha, Pawan, Sukanta, Rout, Maya, Kausik, Chiru and Amit. I would also like to thank my friends Hari, Krishnan, Aathi, Srivatsan, Bala, Bhoomi, Ganesh and Balaji, all of whom made my stay at IIT a pleasant one.

At this time I would like to express my deep sense of gratitude to my beloved parents for their immense patience, moral support, courage and inspiration during this research programme.

Last but not the least, I would like to thank the MME departmental staff and ACMS staff, who helped me in many occasions.

Shankar. J

27th February 2002

IIT, Kanpur

Chapter 1

INTRODUCTION

Stainless steels are defined as iron-based alloys containing at least 10.5% Chromium [1]. In certain stainless steels, the chromium percentage is more than 30%. Stainless steel attains its superior corrosion resistance due to the formation of an invisible but adherent and continuous chromium oxide surface layer. The oxide layer forms and heals itself in the presence of oxygen. In addition to chromium some additional elements such as nickel, molybdenum, nitrogen and sulfur are also added to improve specific characteristics such as repassivation, pitting resistance and mechanical properties. Depending upon the percentage and type of alloying addition, stainless steel is classified into five major categories namely, martensitic, ferritic, austenitic, duplex (ferritic-austenitic) and precipitation-hardening stainless steels. Among these, duplex, ferritic and austenitic stainless steels are noted for their corrosion properties. Stainless steels find a number of applications including aerospace, automotive, chemical processing, medical and recreational fields.

Despite its applications in various fields, processing of wrought stainless steel suffers from several limitations. Wrought stainless steel is normally processed by casting and requires machining to achieve the desired dimensional precision in the final products. Hence, there is a continued thrust for finding a newer method for processing stainless steel to obtain near net shaped products. The powder metallurgy (P/M) route is one of the best processing technique to obtain near net shaped products for the applications. Powder metallurgical stainless steels are a relatively small, but rapidly growing, segment of P/M market. The P/M stainless steel, like its wrought counterpart derives its corrosion resistance from the protective chromium oxide layer. However, the P/M stainless steel microstructure usually contains inherent pores. Depending on their dimensions, these pores/crevices act as initiation sites for breakdown of the passive layer due to accumulation of corrosion products within. Passivity enhancing elements like nickel, molybdenum or more of chromium is added in order to increase the corrosion resistance of P/M stainless steel. Nowadays, P/M Stainless steels with improved corrosion properties are gaining wide popularity. However, compared to the wrought stainless steel

their applications are limited due to their poor density, corrosion resistance and mechanical properties.

The present work was undertaken to improve the properties of P/M 316L (austenitic) and 434L (ferritic) stainless steel by reinforcing them with oxide dispersions of yttrium. The reinforced stainless steels are said to be as oxide dispersion strengthened (ODS) stainless steel, which, have better mechanical properties and corrosion resistance than the normal P/M stainless steels. The better mechanical properties can be attributed to the oxide dispersoids, which act as pinning centers for dislocation motion and grain boundary sliding. The oxide dispersoids act as initiating sites for the formation of protective chromium oxide layer and also act as pinning centers between the oxide layer and the metal surface, thereby giving better mechanical strength to the oxide layer formed. Moreover, sintering is done by two sintering processes namely, solid state sintering and supersolidus liquid phase sintering. The supersolidus liquid phase sintering is a novel method for producing stainless steel as they impart better properties to the sample than normal liquid phase sintering.

In this thesis, Chapter 2 provides a brief introduction about stainless steels and its types. The chapter further describes about corrosion and the various types of corrosion that are possible in stainless steel. A brief background about the P/M processing and the need for P/M processing with specific applications is also discussed. The chapter also briefs about sintering and the types of sintering that are adopted in the present work. The chapter further discusses about P/M stainless steel, their applications and corrosion of P/M stainless steel. Chapter 3 presents the scope of the present work, which includes the rationale for selecting the type of P/M stainless steels and Y_2O_3 as the oxide dispersoid. It further describes the work done on P/M stainless steel and the particulate composites of P/M stainless steel with emphasis on the corrosion resistance of sintered stainless steel.

Chapter 4 describes the experimental procedures that are involved in the thesis. It includes the characterization of the powder, preparation of the powder, compaction. It describes in detail the sintering procedures used for the present study. This is followed by a description about characterization of the powder, metallographic procedures and corrosion measurements. Chapter 5 presents the experimental results of the current work. Chapters 6 and 7 consist of the discussion and conclusion, respectively.

Chapter 2

BACKGROUND

2.1. Stainless Steel

Stainless steels are as defined earlier iron based alloys containing approximately 11% to 30% chromium. Steel becomes stainless due to the formation of a thin, adherent and invisible layer of chromium oxide, which is formed on the surface of the steel in the presence of oxygen. The oxide forms and heals itself in the presence of oxygen. The carbon content in stainless steel is usually less than 0.03% to over 1.0% in certain grades. Other elements that are added to improve the characteristics include nickel, molybdenum, copper, titanium, aluminum, silicon, niobium, nitrogen, sulfur, and selenium. Nickel and nitrogen are used as austenite stabilizers, to achieve a balance of ferrite plus austenite [1]. Molybdenum strengthens the passive film and improves pitting resistance. Copper, titanium and aluminum are added to lower the rate of corrosion. Titanium and niobium are added to reduce the susceptibility of the alloy to intergranular corrosion.

The phase diagrams of Fe-Cr, Fe-Ni and Fe-Mo are shown in Figures 2.1 to 2.3 [2]. In Figure 2.1, the Fe-Cr phase diagram shows the formation of two loops, namely the γ -loop and σ -loop. Since Cr has a BCC structure it acts as a ferrite stabilizer and extends the α -phase, while suppressing the γ -phase, resulting in γ -loop. This divides the Fe-Cr phase diagram into FCC and BCC regions. When Cr is less than 12-13%, an austenite to ferrite transformation occurs on cooling within the loop. But when the Cr content is greater than 13% no transformation occurs [3]. The Fe-Cr phase diagram at low temperatures is not a complete range of solid solution. There is an intermediate phase formed at 821°C called σ -phase. This phase has a tetragonal structure and is hard and brittle. Presence of this phase will lead to embrittlement of the alloy [3]. Nickel is added to iron to stabilize the austenitic phase, since it has the same FCC structure. The phase diagram of Fe-Ni in Figure 2.2 shows that the γ -loop is formed at less than 5% nickel. Molybdenum is added to increase the pitting resistance of stainless steel. Since it is added in very less amount it does not significantly affect the formation of γ -loop. The Fe-Mo

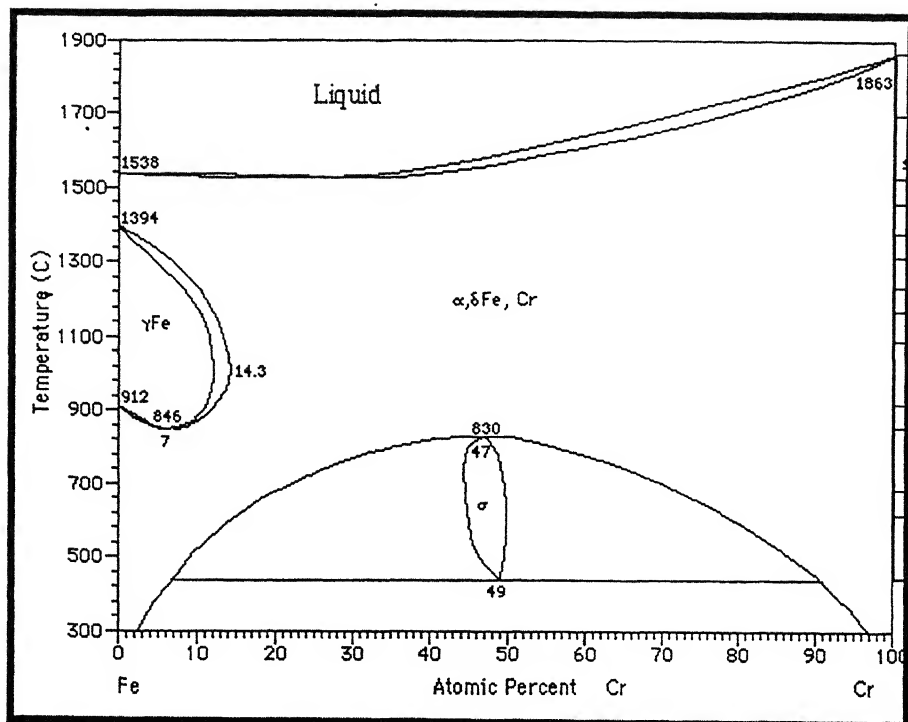


Figure 2.1. Fe-Cr phase diagram [2].

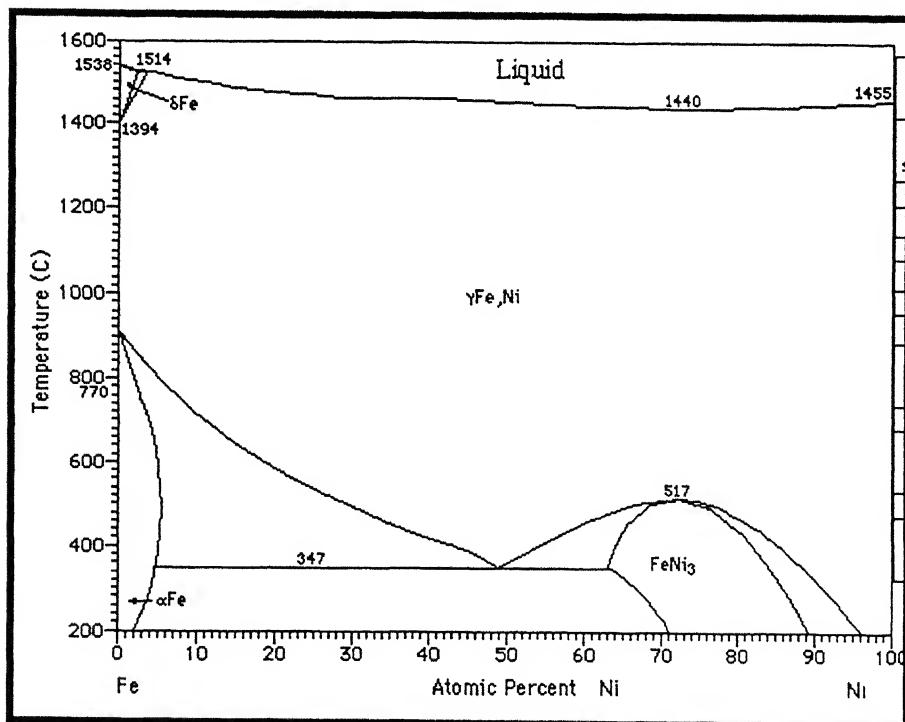


Figure 2.2. Fe-Ni phase diagram [2].

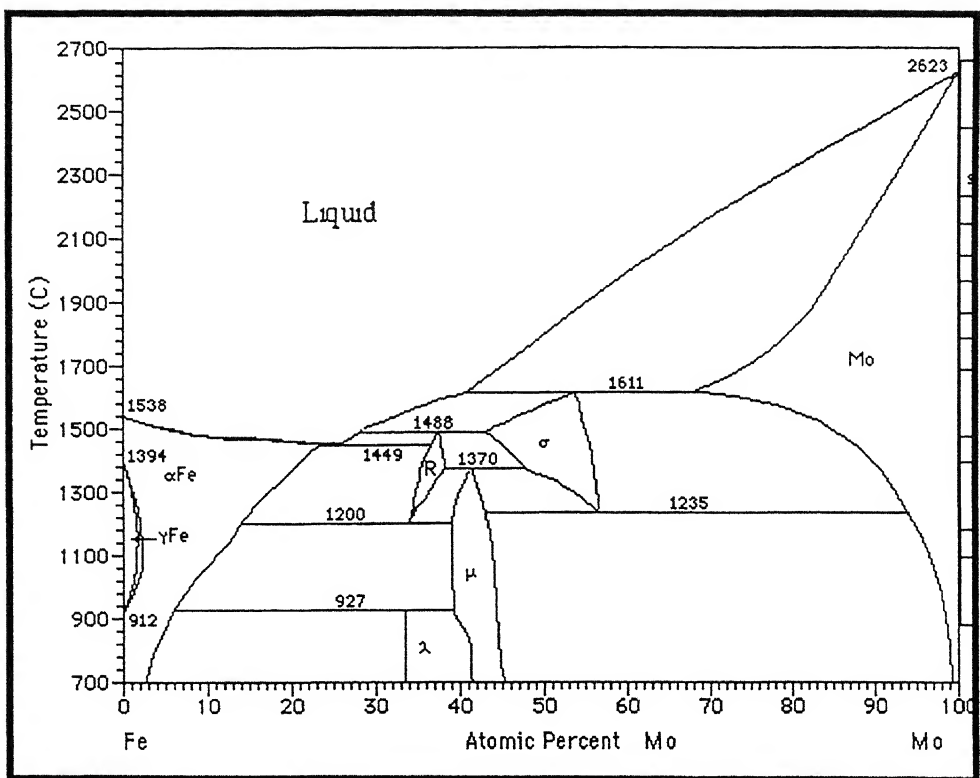


Figure 2.3. Fe-Mo phase diagram [2].

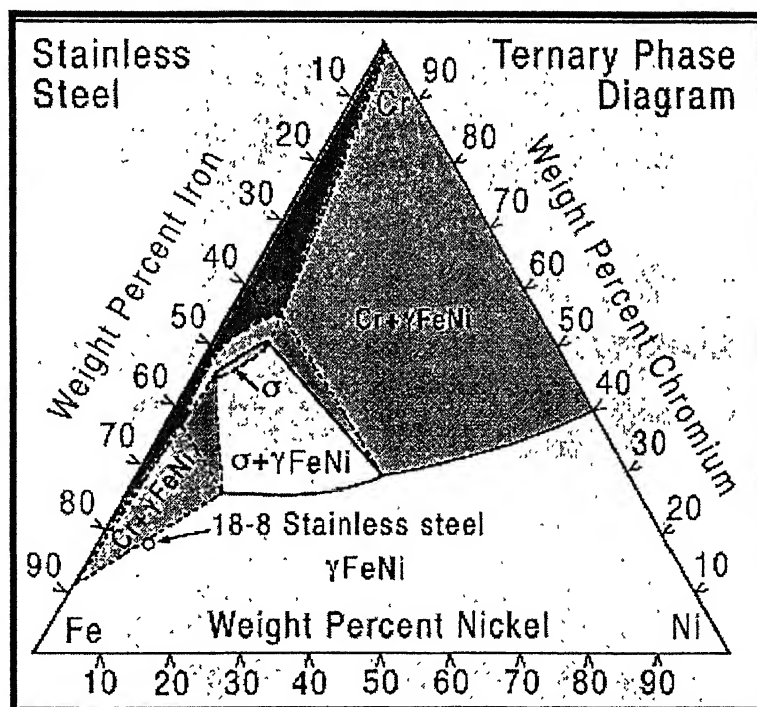


Figure 2.4. Ternary phase diagram of stainless steel.

phase diagram is shown in Figure 2.3. The ternary phase diagram of stainless steel is shown in Figure 2.4, which shows the critical composition for stainless steel.

The various types of stainless steel according to the additive added and grades are shown in Figure 2.4 [4]. Though there are many grades of stainless steel available in the market, stainless steel is commonly divided into five groups: martensitic, ferritic, austenitic, duplex and precipitation-hardening stainless steel.

- Martensitic stainless steels are essentially alloys of chromium and carbon with a distorted body centered cubic (bcc) structure in hardened condition. The content of chromium in this type of steel is 10.5% to 18% and the carbon content may exceed 1.2% [3]. Apparently this type of stainless steel is corrosion resistant only in relatively mild environments i.e., around 4-6 pH. The chromium and carbon content must be balance to ensure the martensitic structure after hardening. These alloys are magnetic and their heat-treated structure is body centered tetragonal (bct). Increased carbon content in these alloys increases the strength but decreases ductility and toughness. Usually molybdenum and nickel are added to improve the corrosion resistance and toughness. Sulfur or selenium is added in some cases to improve machinability of martensitic stainless steels. Excess carbides may be added to increase wear resistance but as mentioned earlier the toughness will be lowered. These steels are applicable for machine parts, shafts, cutlery, vegetable tools, bolts, nozzles and valve parts.
- Ferritic stainless steels are named so because of their body centered cubic (bcc) structure is the same as that of iron at room temperature. The ferritic alloys are ferro-magnetic and have good ductility and formability. Ferritic stainless steels have chromium content varying between 11 to 30%; with only a small amount of austenitic forming elements like carbon, nitrogen and nickel. Their high temperature strength is poor when compared to austenitic grades. Their main advantages are their resistance to chloride stress corrosion-cracking, atmospheric corrosion and oxidation at a relatively low cost. Sulfur or selenium may be added to some grades to improve machinability. These alloys can be hardened by heat treatment. The ferritic alloy that is used in the present work is 434L, which has a

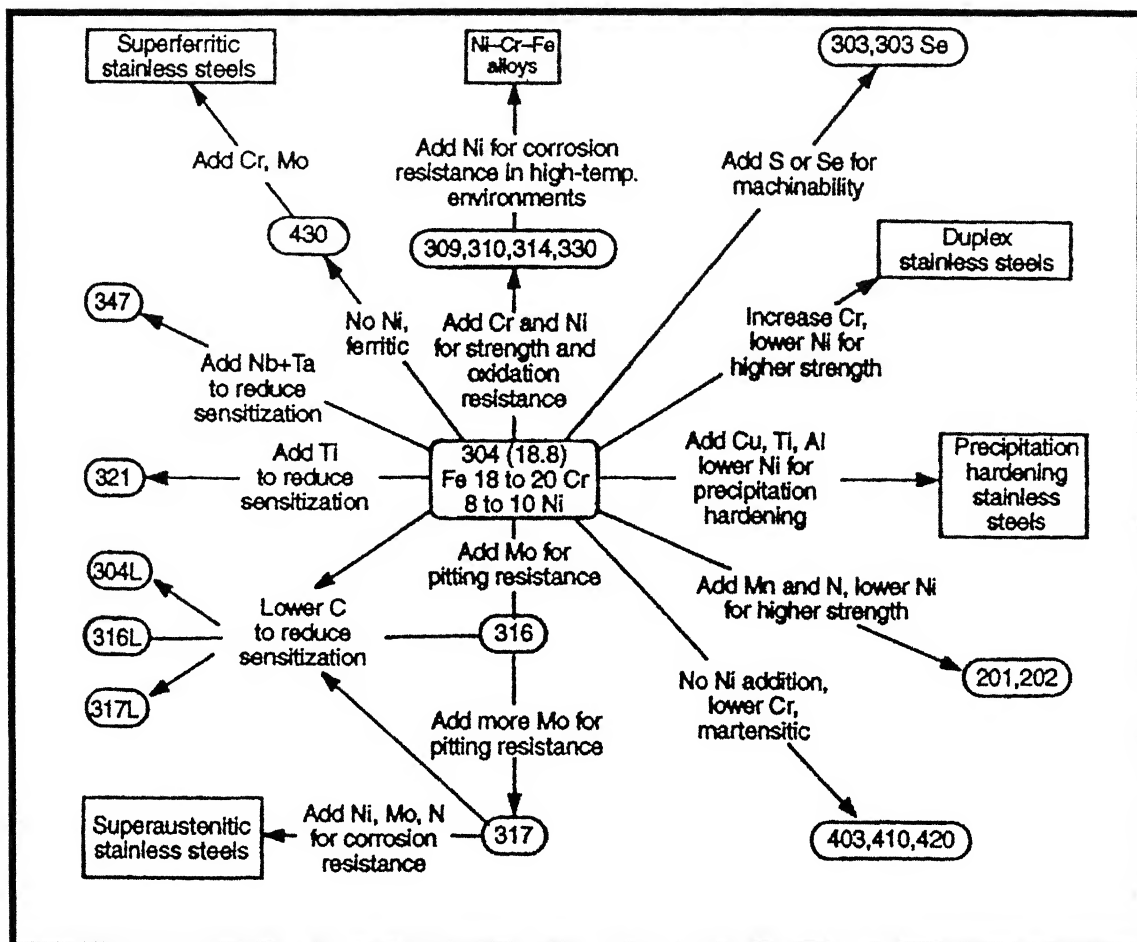


Figure 2.4. Various types of stainless steel [4].

chromium content of 16-18% and are used for automotive trims and household utensils.

- Austenitic stainless steels are noted for high toughness, strength, ductility and formability. This constitutes the largest stainless steel family in terms of number alloys and usage. Austenitic stainless steels have face centered cubic structure and are non-magnetic. Adding austenizing agents like nickel, nitrogen and manganese develops the face centered cubic structure. Like the ferritic alloys the austenitic alloys can be hardened through heat treatment. The usual composition of austenitic stainless steels contains chromium about 16 to 26%, nickel upto 35% and manganese upto 15%. There are two basic categories of austenitic stainless steels, the 3xx series having chromium-nickel alloys such as 316, 304 etc and the 2xx alloys containing manganese-nitrogen alloys such as 201, 241 etc. The alloys having nitrogen will have higher strength when compared to the other alloys. Molybdenum, copper, silicon, aluminum, titanium and niobium may be added to improve specific properties like pitting resistance or oxidation resistance.
- Duplex stainless steels are chromium-nickel-molybdenum alloys that are balanced to contain a mixture of austenitic and ferritic mixture [5]. The exact amount of the phases is a function of composition and heat treatment. The principal alloying elements in duplex stainless steels are chromium and nickel, but nitrogen, molybdenum, copper, silicon and tungsten are added to control structural balance and thereby impart corrosion resistance characteristics. Duplex stainless steels have better stress-corrosion cracking resistance than austenitic and improved toughness and ductility compared to ferritic stainless steels. Nitrogen can be added to duplex stainless steels to improve as-welded corrosion properties, chloride corrosion resistance and toughness.
- Precipitation hardened stainless steels are chromium-nickel alloys containing precipitation-hardening elements like copper, aluminum or titanium. The precipitation-hardened stainless steels are either martensitic or austenitic in annealed condition. The precipitation-hardened stainless steels have good ductility and toughness with moderate to good corrosion resistance. The well-

known precipitation hardened stainless steel is S17400 grade, which is a chromium-nickel alloy containing copper as the aging element.

2.1.1. Selection of Stainless Steel

The selection of the type of stainless steel used depends upon various factors and the environment and type of application for which it is to be used. Martensitic stainless steels are used only in mild environments when compared to the other stainless steels, but it has higher strength and wear resistance. Austenitic stainless steels have good ductility, formability and corrosion resistance. Ferritic stainless steels have lesser corrosion resistance than austenitic stainless steels, but are preferred relatively because of their low cost. Precipitation hardened stainless steels have better mechanical properties than other types of stainless steels but their corrosion resistance is moderate. Duplex stainless steels have improved corrosion resistance than austenitic stainless steels and exhibit higher toughness and ductility than ferritic alloys. The general characteristics that are to be considered while selecting a type of stainless steel for an application are

- Corrosion resistance
- Resistance to oxidation and sulfidation
- Strength and ductility at ambient and service temperatures
- Fabrication characteristics
- Stability of the properties for various service conditions
- Physical property characteristics such as magnetic properties, thermal conductivity, electrical resistance
- Toughness and rigidity
- Resistance to abrasion, galling and seizing
- Surface finish and/or reflectivity.

2.1.2. Corrosion in Stainless steels

Stainless steel owes its corrosion resistance to the protective, adherent and invisible layer of chromium oxide, which is formed on its surface when exposed to atmospheres containing oxygen. This chromium oxide layer makes steel as stainless steel. Though stainless steel has very good corrosion resistance in mild environments, it suffers

from various forms of corrosion depending upon the aggressiveness of the environment [1]. The general types of corrosion and their effect on stainless steel are mentioned below.

- General or uniform corrosion is defined as attack in uniform fashion over the entire exposed area of the surface [6]. But this mode of attack is not severe since the surface gets corroded uniformly. Moreover in stainless steel, the chromium oxide layer is formed which protects the surface from uniform corrosion. Hence stainless steels are usually highly resistant to this mode of corrosion.
- Galvanic corrosion occurs when two dissimilar metals are electrically connected and exposed to an electrolyte, then the more electrochemically active metal gets corroded at an increased rate. The galvanic series for various metals in seawater is given in Table 2.1 [6], which can be used as a guide to determine which type of metals, or alloys are more susceptible to galvanic corrosion. Stainless steels show active-passive behavior and hence there are two places that it occupies in the galvanic series according to its nature. Generally from the table stainless steels are treated as noble alloys and are resistant to this form of an attack.
- Pitting and Crevice Corrosion comes under localized corrosion attack. When the localized areas of the surface passive layer are damaged, it is no longer able to protect the surface from corrosion [7]. This type of attack is called as localized attack and is more dangerous than uniform attack, in the sense that attack is concentrated at a specific location and complete penetration into the metal surface in a short time leading to catastrophic failure.
- Stress Corrosion Cracking occurs when a stressed metal is exposed to a typical corrosive environment. Stress corrosion cracks initiate at the surface of the metal and propagates by means of tensile stress and chemical reactions at the crack tip. Hot concentrated chloride solutions and chloride-contaminated steam can cause stress corrosion cracking in stainless steel [6].
- Inter-Granular Corrosion is a localized attack that is seen frequently in stainless steel. In stainless steels having carbon content more than 0.2% will react with chromium to form chromium carbide (Cr_7C_3) [1]. Hence the grain boundaries

Table 2.1. Galvanic series of various metals and alloys in seawater [6].

	<u>Active</u>
Magnesium alloys	
Zinc	
Aluminum and aluminum alloys	
Mild steel	
Wrought iron	
Cast iron	
<i>13% Chromium stainless steel, type 410 (active)</i>	
<i>Lead-tin solder (50-50)</i>	
<i>18-8 Stainless steel, type 304 (active)</i>	
<i>18-8, 3% Mo stainless steel, type 316 (active)</i>	
Lead	
Tin	
Nickel (active)	
Aluminum bronze	
Red brass	
Copper	
Silicon bronze	
70Cu-30Ni	
Nickel (passive)	
70Ni-30Cu (Monel)	
Titanium	
<i>18-8 Stainless steel, type 404 (passive)</i>	
<i>18-8, 3% Mo stainless steel, type 316 (passive)</i>	
	<u>Noble</u>

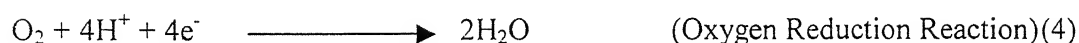
become depleted of chromium and a galvanic couple is formed and the regions near the grain boundaries get corroded leading to inter-granular corrosion. This type of corrosion can be reduced by reducing the amount of carbon less than the critical amount or by adding some carbide forming elements like Mo in 316L so that the formation of chromium carbide is avoided. These kinds of stainless steels are called stabilized stainless steels.

2.2 Electrochemical Corrosion

Corrosion can be defined as the degradation of a metal by an electrochemical reaction with its environment [8]. All metals are found in their low energy state ores, in the form of their oxides, sulfides, carbonates or more complex compounds. Large amount of energy is supplied in order to extract a pure metal from its ore. This pure metal is a high energy state of the metal and hence they try to come back to the low energy state by recombining with the environment. This process is called corrosion. Figure 2.5 shows the thermodynamic energy profile for metals and their compounds. The thermodynamic aspects of corrosion will be briefly discussed. All the interactions between elements and compounds are governed by the free energy changes (ΔG). Any reaction is said to be spontaneous when ΔG for the reaction is negative. At room temperature most of the chemical compounds of metals have lower free energy than the pure metals and hence most of the metals have an inherent tendency to corrode.

In all kinds of aqueous corrosion, there are two reactions occurring at the metal/liquid interface; an electron producing reaction (anodic or oxidation reaction) and an electron consuming reaction (cathodic or reduction reaction). The corrosion reaction for the creation of a wet electrochemical cell requires four basic requirements, the cathode on which the reduction reaction occurs, an anode on which oxidation occurs, an electrolyte to act as the conducting medium for ions and a electrical connection for electron to flow between the anode and cathode. The anodic reaction is invariably corrosion of the metal as shown in equation 1. Several cathodic reactions can occur during corrosion [1]. The simplest of them is reduction of hydrogen ions (equation 2). Another is reduction of an oxidized ion in solution (redox reaction) as in equation 3.

Another reaction is reduction of dissolved oxygen as in equation 4. In the absence of any of these reactions water reduction will occur as in equation 5.



A basic wet corrosion cell is shown in the Figure 2.6. The potential difference between the anode and the cathode could be measured by using a voltmeter in the circuit. But this gives only the potential difference between the electrodes and in order to measure the absolute potential we need a third electrode. This third electrode is called as the standard electrode against which all the measurements can be made. The standard hydrogen electrode, saturated calomel electrode (SCE) etc are usually used as the standard electrodes. The Table 1 gives some commonly used standard electrodes and their potentials.

2.3. Polarization

When a metal is not in equilibrium with the solution of ions, the electrode potential differs from the free corrosion potential by an amount known as the polarization [8]. It can also be said as overpotential or overvoltage. Polarization is a very important corrosion parameter as it is useful in calculating the rates of the corrosion process. The deviation of the equilibrium potential is a combination of an anodic polarization of metal and a cathodic polarization of the environment. If the electrons are made available as in equation 2, the potentials at the surface becomes more negative, suggesting that excess electrons with their negative charges accumulate at the metal/solution interface waiting

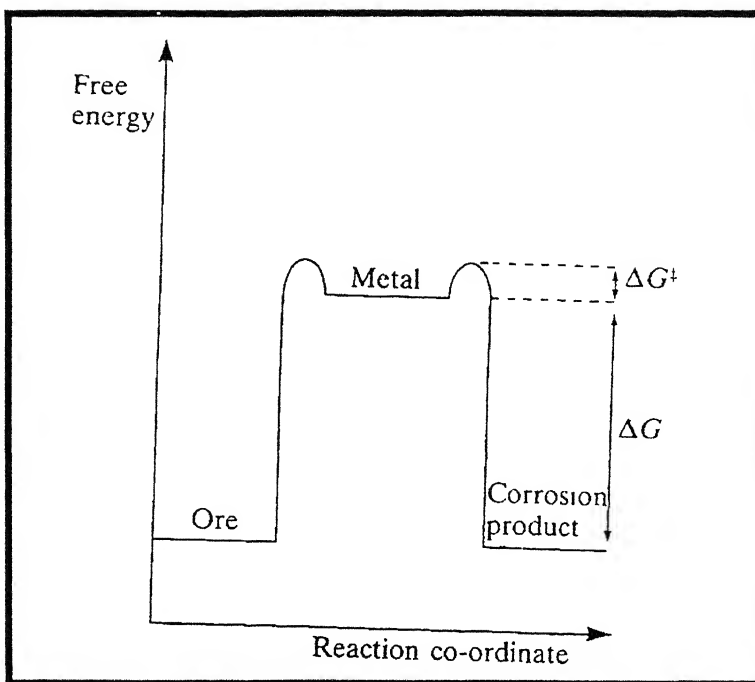


Figure 2.5. Thermodynamic energy profile for metals and their compounds [8].

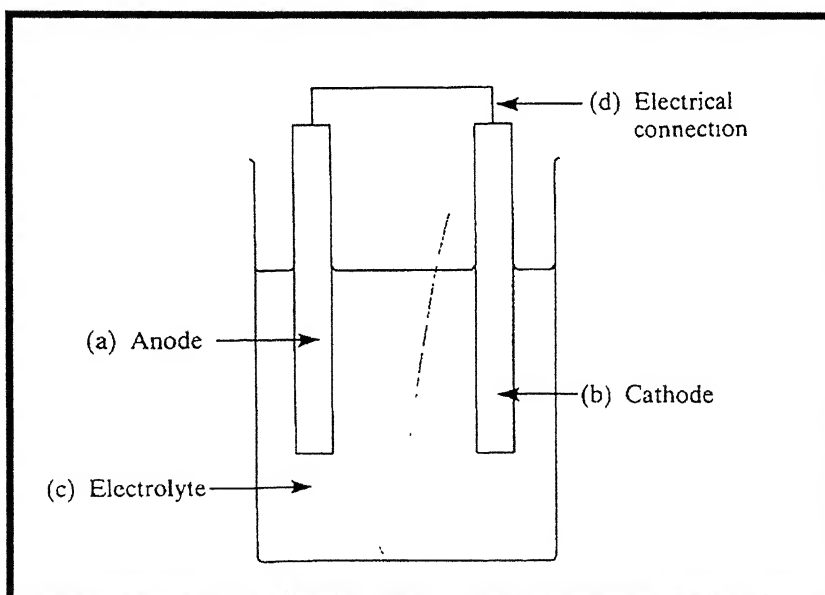


Figure 2.6. Basic wet corrosion cell [8].

Table 2.2. Standard reference electrode potentials [1].

Electrode	Electrolyte	Potential (V)
Calomel (SCE)	Saturated KCl	+0.2420
Calomel (NCE)	1.0 M KCl	+0.2810
Calomel	0.1 M KCl	+0.3335
Silver/Silver Chloride (SSC)	1.0M KCl	+0.2224
SSC	Sea Water	+0.25 (approx)
Copper/Copper sulphate (CSE)	Sea Water	+0.30 (approx)
Zinc	Sea Water	-0.79

for the reaction. This negative potential charge is called as cathodic polarization. Similarly, there will be a deficiency of electrons on the metal surface interface by the reaction shown in equation 1, which produces a positive potential change called anodic polarization [1]. In an aqueous electrolyte solution the surface will reach a steady potential, E_{corr} , which depends on the ability and rate at which electrons can be exchanged by the anodic and cathodic reactions. When the surface potential increases above the E_{corr} value, to a value E , then the anodic polarization is given by the difference between E and E_{corr} . At equilibrium the forward anodic reaction, i_a is equal to the reverse cathodic reaction, i_c . Hence the rate of the reaction can be given by,

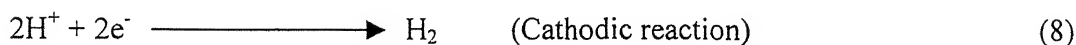
$$i_a = i_c = i_0 = A_0 \exp[-\Delta G/RT] \quad (6)$$

There are two methods available for measurement of corrosion rate using polarization methods, namely Tafel extrapolation and polarization resistance. The polarization methods to measure corrosion rates have their inherent advantages. The main advantage of these methods is that the time taken for conducting experiments is relatively short, whereas the conventional weight loss methods require several days. The polarization methods are highly sensitive, and accelerating factors such as elevated temperature, to increase rates is generally not necessary. Moreover these methods are non destructive and several repetition experiments can be carried out using the same sample.

The mixed potential theory forms a basic for explaining the polarization techniques. The mixed potential theory consists of two simple hypothesis:

1. Any electrochemical reaction can be divided into two or more partial oxidation and reduction reactions.
2. There cannot be net accumulation of electrical charge during an chemical reaction i.e., corrosion reaction the sum of the anodic oxidation currents should be equal to the sum of the cathodic reduction currents. In other words the total rate of oxidation should be equal to total rate of reduction [9].

Consider the reactions for zinc getting corroded in an acid solution. Then the anodic and cathodic reactions are given by,



These reactions are called as the half-cell reactions and the potential corresponding to them are called cell potential. The potentials cannot coexist separately on an electrically conducting surface. The potentials will polarize to an intermediate value called as the corrosion potential or mixed potential (E_{corr}). When there is no external current flowing into the system, then the equilibrium potential attained is called open current potential (OCP) or free corrosion potential (E_{corr}). As the reactions polarize on the same surface the change in potentials is given by,

$$\eta_a = \beta_a \log (i_a/i_o) \quad (9)$$

$$\eta_c = \beta_c \log (i_c/i_o) \quad (10)$$

where η_a and η_c are anodic and cathodic polarization, β_a and β_c are the Tafel constants, I_a and i_c are the anodic and cathodic currents respectively. At E_{corr} the rate of anodic and cathodic reactions are equal and is equal to the current density, i_{corr} . The half-cell reactions for dissolution of Zn in acid are shown in the Figure 2.7 [8]. This figure is called as Evans diagram and represents an active material.

The various polarization techniques that are commonly used are linear polarization, Tafel extrapolation, potentiostatic polarization and cyclic polarization. These four polarization techniques are summarized in the Figure 2.8 [11].

2.3.1. Linear Polarization

The linear polarization uses the smallest potential spectrum of all the polarization techniques. Linear polarization is measured at approximately ± 20 mV from the open current potential. Consequently it allows repeated measurements on the same electrode, enabling it to be used for long term corrosion monitoring and for determining the steady state corrosion rate. A typical linear polarization curve is shown in the Figure 2.9 [11]. The slope of the polarization curve gives the polarization resistance, R_p . From the value of R_p the i_{corr} value is calculated using the formula,

$$i_{\text{corr}} = [1/(2.303R_p)] [(\beta_a\beta_c)/(\beta_a + \beta_c)] \quad (11)$$

where $R_p = (\Delta E/\Delta i)$

The corrosion rate is directly proportional to the corrosion current and can be converted into corrosion rate using the formula,

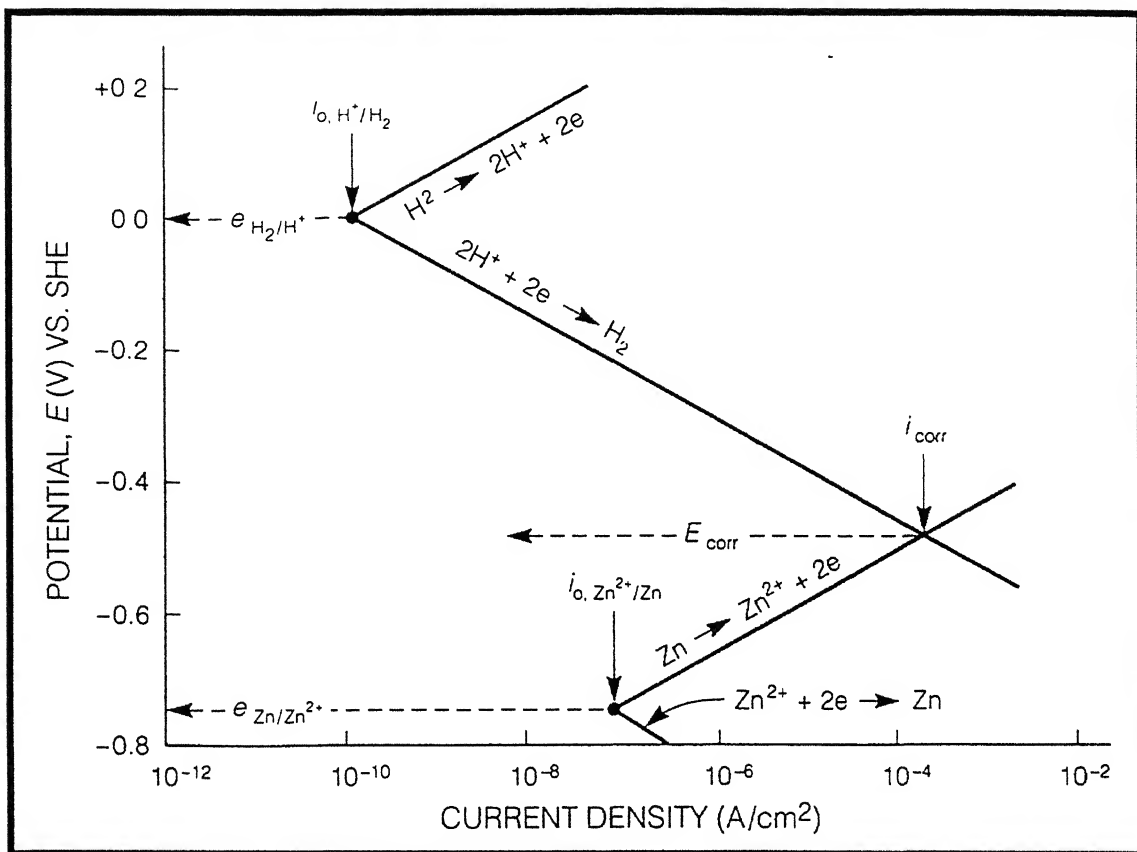


Figure 2.7. Evans diagram for an active metal [1].

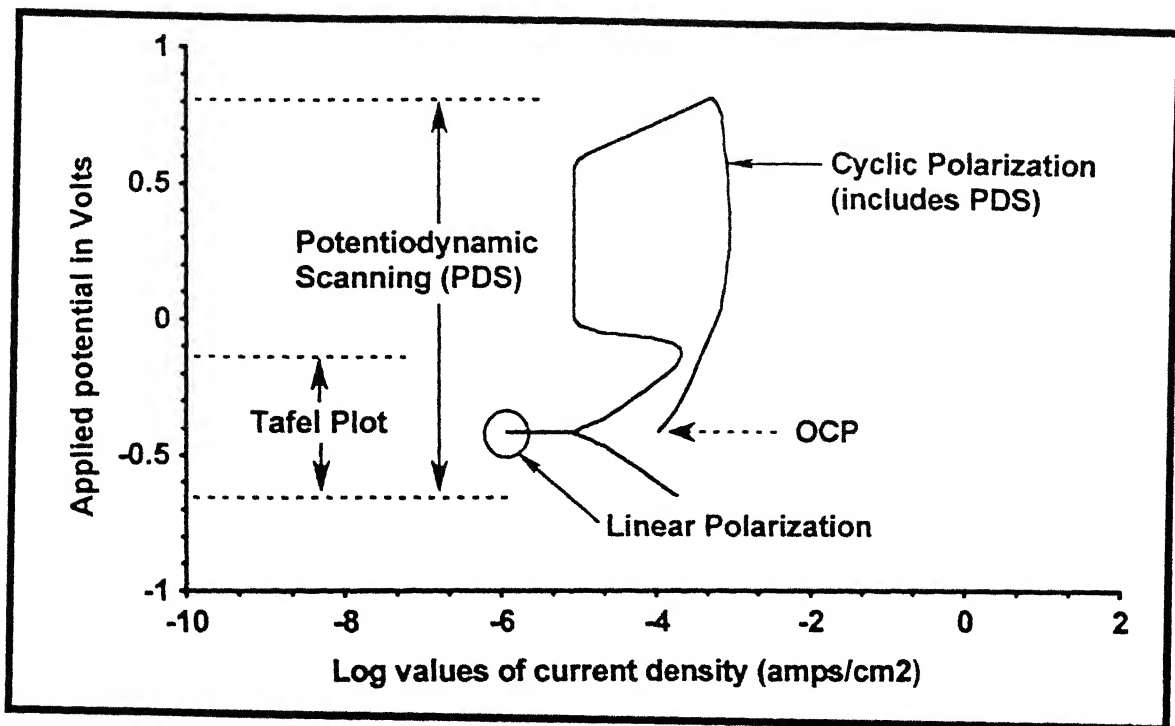


Figure 2.8. Various types of polarization methods [11].

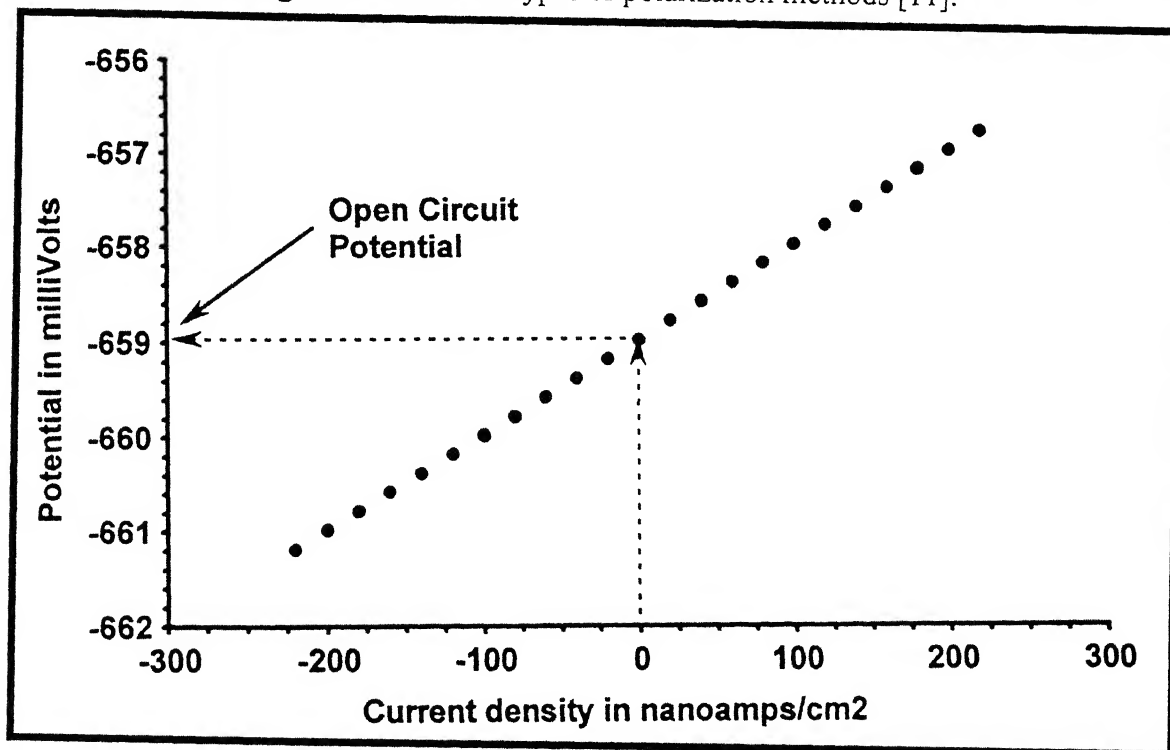


Figure 2.9. Schematic diagram of a linear polarization plot [10].

$$\text{Corrosion rate in miles/year (MPY)} = i_{\text{corr}} (\Lambda) (1/\rho) (\epsilon) \quad (12)$$

where the value of Λ is 1.2866×10^5 [equivalents.sec.mils]/[columbs.cm.years], ρ is the metal density in g/cm^3 and ϵ is the equivalent weight. There are various assumptions made in the equation (12) which are listed below,

- 1) The reactions of the systems are reversible
- 2) The corrosion reaction is controlled by the activation energy
- 3) There is no change on the electrode surface during polarization
- 4) Polarization is due to corrosion
- 5) The energy barrier for the forward and reverse reactions are symmetrical.

The linear polarization suffers from a lot of limitations. It is difficult to obtain linear data in high resistance solutions or when the metals having extremely low corrosion rates. This method cannot determine the type of kinetics that control the corrosion rate.

2.3.2. Tafel Extrapolation

The Tafel extrapolation method was introduced to illustrate the application of mixed potential theory. The Tafel extrapolation method uses a wider potential spectrum than linear polarization and hence provides more information. The linear polarization plot provides information about the corrosion rate, whereas the Tafel plot provides information about the corrosion rate as well as the kinetic data. The Tafel plot is carried out normally in a potential range of $\pm 250\text{mV}$ from OCP. An idealized Tafel plot is shown in the Figure 2.10 [11]. The figure shows distinct anodic and cathodic polarization regions and the inflection point of the two curves gives the OCP. The linear region in the graph is extrapolated and the slopes of the linear regions are calculated. These are called as Tafel slopes. The linearity over which the Tafel slope are calculated should have one decade of magnitude. A vertical line is drawn from the inflection point to the X-axis to give the corrosion current. From the value of corrosion current the rate of corrosion can be calculated using equation (12). In certain cases, where dilute solutions are used, concentration polarization and ohmic resistance effects are likely at higher current densities. Hence the magnitude of the Tafel slope is not equal to one decade, Tafel extrapolation is carried out only in the cathodic region. The cathodic polarization slope is

extrapolated and is allowed to intersect the corrosion potential E_{corr} . From this inflection point the corrosion current is calculated [8].

The main limitation of Tafel extrapolation when compared with the linear polarization is that the test electrode can be polarized only for a limited number of times. This is due to the surface roughening that takes place with each polarization. Moreover the Tafel plot cannot predict about the passive behavior of the system studied. It cannot be used for studying the localized corrosion behavior of the system.

2.3.3. Potentiodynamic Polarization

The potentiodynamic polarization is carried out in a wider range of potential spectrum and gives much more details about the samples response to the environment. The potentiodynamic polarization provides data about the metal behavior i.e., whether the metal is active or passive or active passive in the given environment. The plot elucidates the properties of the passive film and the effect of inhibitors on the corrosion behavior of the metal. Depending upon the nature of potentiodynamic polarization curve, alloys can be divided into active alloys and active-passive alloys. For an active metal the corrosion rate increases linearly with increase in the anodic polarization potential. This is due to the non-protective oxide layer, which forms on the metal surface. For an active passive metal the corrosion rate increases with polarization potential upto a critical current density, (i_{crit}) after which it falls down rapidly due to the formation of a protective passive film.

A typical potentiodynamic polarization plot is shown in Figure 2.10 for an active passive metal [12]. The figure shows the various regions of a potentiodynamic plot for an active-passive metal. The first two regions are the normal cathodic and anodic polarization regions that were discussed for the Tafel plot. The anodic region is widened to show the passive film formation. The anodic region can be subdivided into three main regions namely, the active region, the passive region and the transpassive region. The active region and the cathodic curve can be extrapolated to extract the values of E_{corr} and i_{corr} . The active region ends at the primary passivation potential (E_{pp}) at which the passive film becomes stable and the corrosion rate falls rapidly. The current corresponding to this value is called as critical current density (i_{crit}). As the potential is increased beyond this value, the current density decreases until it reaches a steady current called as the passive

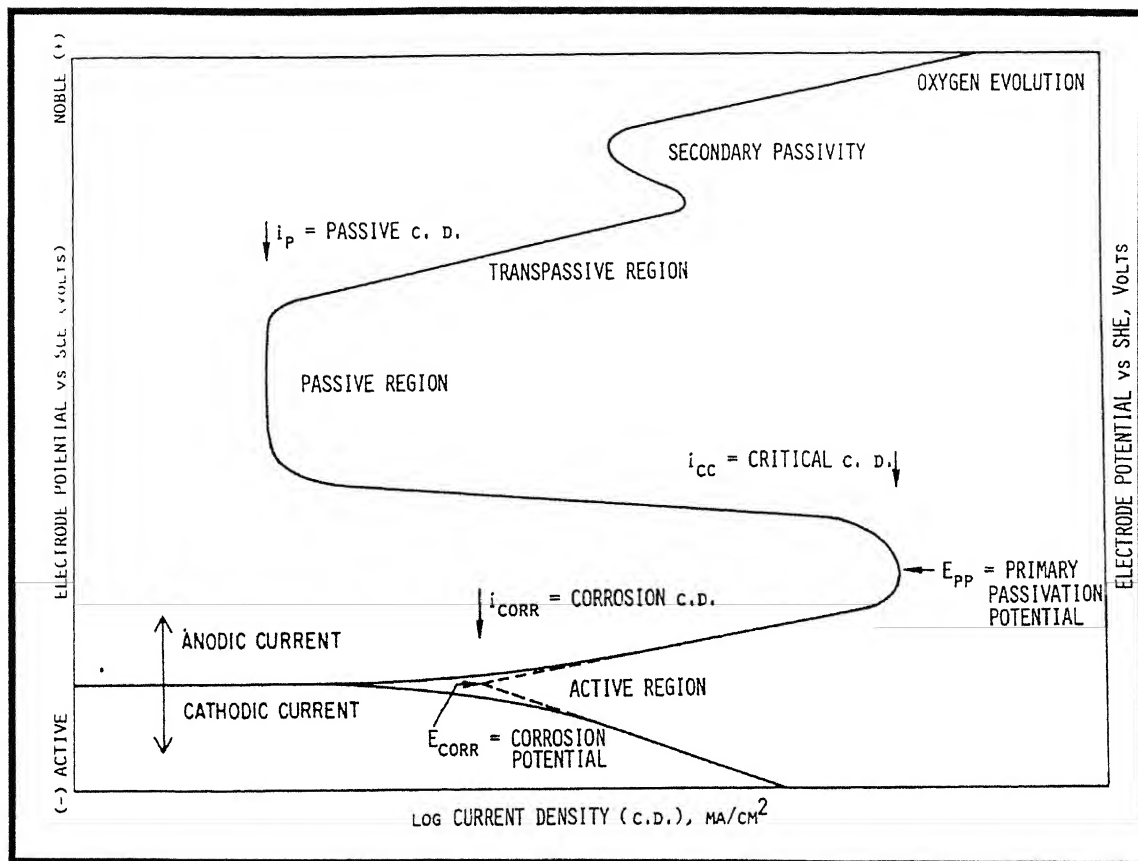


Figure 2.10. Schematic diagram showing the potentiodynamic polarization for an active-passive metal [12].

current density (i_{pass}). The range over which the steady current is maintained is known as the passive range and it relates to the stability of the passive film. As the potential is increased further the passive layer breaks down and the anodic rate increases in the transpassive region. This breakdown in passivity can be attributed to the oxygen evolution or due to localized mechanisms such as pitting. In certain kind of alloys like stainless steel, there will be an additional region showing secondary passivity. This results due to the formation of some secondary oxide layer, which ultimately breaks leading to increase in the corrosion rate. The potential at which the passive film breaks is known as pitting potential (E_{pitt}) and the potential at which the oxide film completely breaks apart and is called the breakdown potential (E_{break}).

The schematic diagram in Figure 2.11 shows the type of alloy that can be used depending upon the nature of the environment. The figure shows four types of alloys and three environments that are commonly used. For a reducing atmosphere, as in 1, either the non-passivating alloy A or the partially passivating alloy B is superior because they have better corrosion resistance in the active conditions. The alloys C and D produce strong passivity and hence alloying elements like chromium should be added. This makes the alloys more expensive and thus unjustifiable for the service condition [1]. For a moderately oxidizing atmosphere, number 2, the alloy C would be recommended because the reduction curve exceeds the critical current density and it is the only alloy showing stable passivity. In alloy B, the reduction curve exceeds critical current density, but the passive region is not broad enough to ensure good passive resistance. Alloy D is in a state of borderline passivity, with both active and passive states possible. For strong oxidizing condition in 3, alloy D is recommended as the reduction curve exceeds critical current density and the corrosion rate is low. In alloy C, the passivity breaks in this condition and it is in the transpassive region. Alloys A and B are not resistant to high oxidizing conditions.

The main limitation of potentiodynamic polarization is that the sample surface gets disturbed after the experiment is completed. Hence the test can be conducted only once at a time. Moreover the exact corrosion rate cannot be predicted accurately by this method.

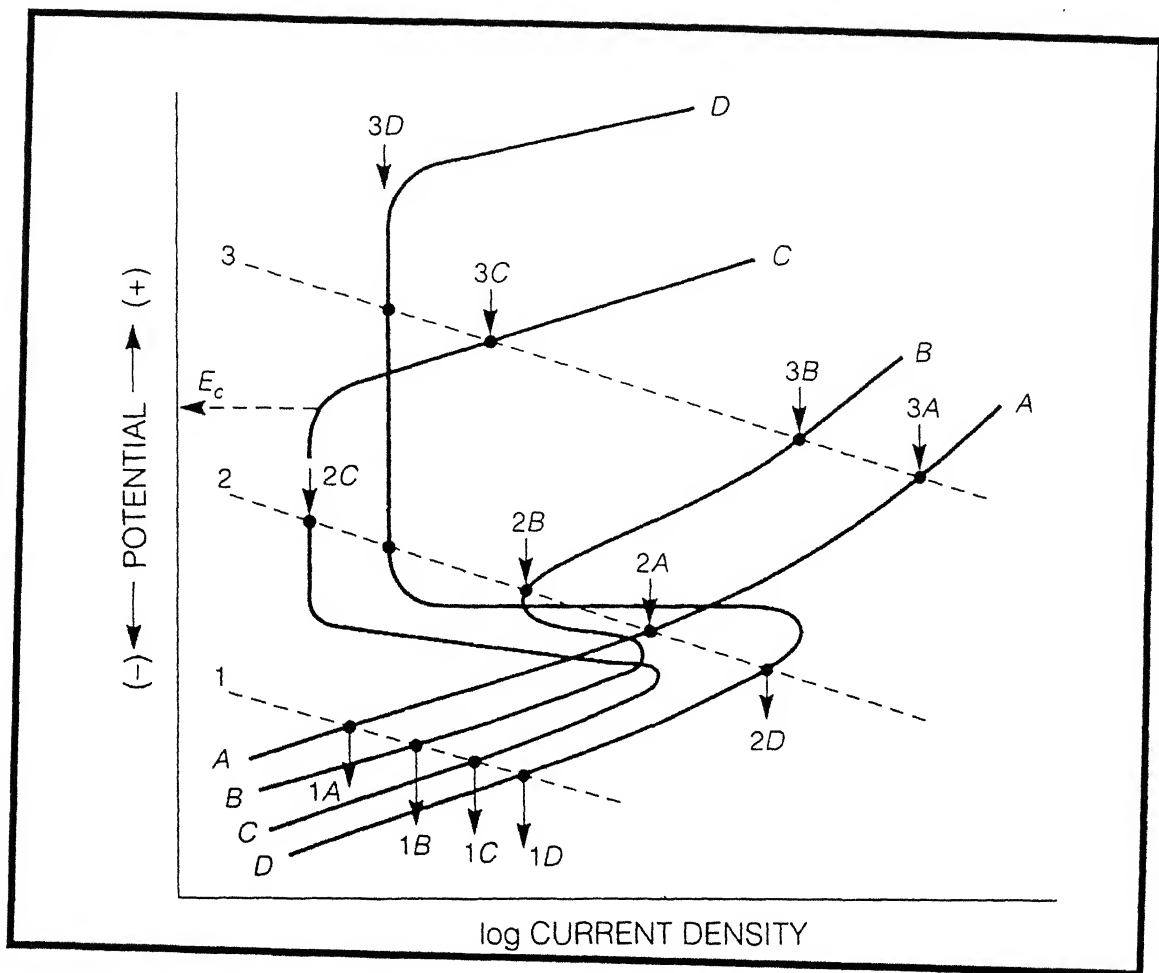
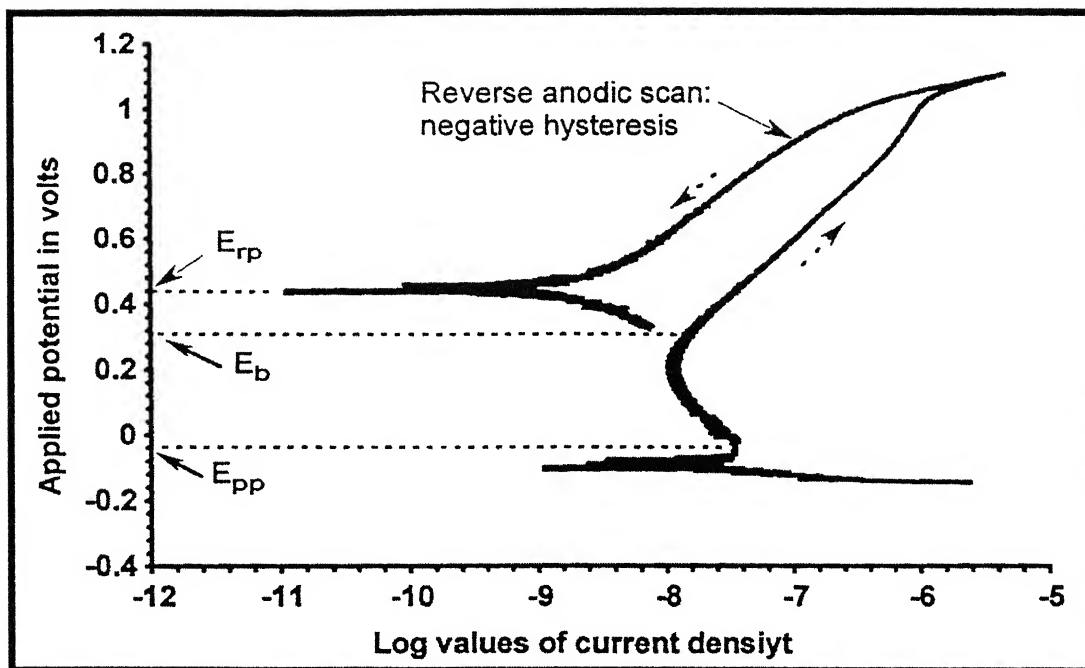


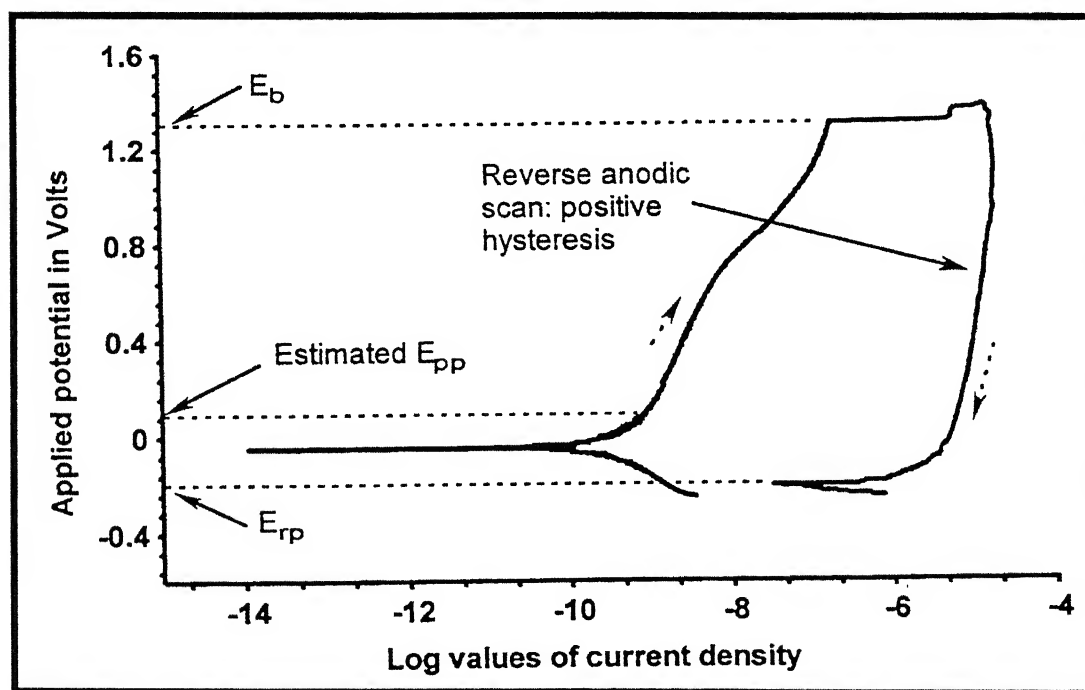
Figure 2.11. Anodic polarization curves for hypothetical alloy A,B,C,D in 1) reducing 2) moderately oxidizing 3) highly oxidizing environments [1].

2.3.4. Cyclic Polarization Method

Cyclic polarization technique is an extension of the potentiodynamic polarization technique and can be used for determining the susceptibility of the alloy to localized corrosion [13]. The potentiodynamic polarization scan is carried out till the pitting potential and the scan is reversed. This reverse scanning does not follow the forward scan and hence forms a hysteresis loop. The loop can be a negative loop or a positive loop and depending upon the nature of the loop the susceptibility of the alloy to localized corrosion can be determined. A typical cyclic polarization plot is shown in Figure 2.12, where (a) represents negative loop and (b) positive loop. The negative hysteresis occurs when the reverse scan current density is less than that for the forward scan, and positive hysteresis occurs when reverse scan current density is greater than that for the forward scan [11]. This hysteresis can provide information regarding the pitting corrosion rates and the ability of the passive film to repair itself. A positive hysteresis occurs when the passive film is not repaired and the negative hysteresis occurs when the passive film repairs itself after pitting has taken place. The potential E_{rp} shown in Figure 2.12, is called the repassivation potential. The passive film on the alloy will be damaged when the potential is raised to the transpassive region and pits can form at discrete locations on the surface. It is generally believed that pits will continue to grow when the OCP is greater than E_{rp} and pit growth will be inhibited when it is the other way [11].



(a)



(b)

Figure 2.12. The schematic diagram of a cyclic polarization plot showing (a) negative hysteresis and (b) positive hysteresis [5].

2.4. Powder Metallurgy

Powder metallurgy by definition, is a process whereby a solid metal, alloy or a ceramic in the form of a mass of dry particles, normally less than 150 μm in diameter, is converted into an engineering component of pre-determined shape and processing properties which allows it to be used in most of the cases without further processing [15]. There are three important steps while processing a powder metallurgical product. They are, powder production; compaction of the powders and sintering the product to obtain near net shape condition.

The metal powders can be divided into two main divisions namely, ferrous powders that include iron and its alloys and non-ferrous powders that include metals like copper, tin, tungsten, aluminum etc. Metal powders can be produced by physical, chemical and mechanical methods. Atomization is the important process by which metal powders are prepared. The dispersion of a molten metal into particles by a rapidly moving gas or liquid stream or by mechanical means is called as atomization. In this process the metal is melted, atomized and then allowed to solidify by cooling [15]. Powders of high purity are produced electrolytically. The behavior of powder during the subsequent consolidation process is determined by both particle and bulk properties. A powder is characterized, therefore, not only by chemical composition but also through particle shape, size and surface chemistry and in bulk by compressibility. Stainless steel powders are produced normally in the prealloyed form since it has heavy alloying additions. Producing stainless steel by premixed powders will result in a non-homogenous mixture. Stainless steel powders are produced by water atomization and gas atomization technique.

The metal powder produced is compacted into required shape and size in a die. The powders are transferred into a die and uniaxial pressure is applied on the die to produce a green compact. In case of hot compaction technique, temperature is applied to the powder during compaction and the end product will be completely sintered. In cold compaction techniques the part is formed during compression which is then subjected to sintering. During compaction the powders get compressed and attain a certain density called the green density. A lubricant is used in order to reduce the friction by the die walls

and for easy removal of the compressed sample. The densification of the powders during the compaction is shown in the Figure 2.14 [15].

The compacted green sample is then subjected to a thermal treatment called sintering in air or in reducing atmosphere or in vacuum. Atmospheric sintering is used only in case of ceramics as most of the metals get oxidized if sintered in atmosphere. For metals a reducing atmosphere or vacuum or an inert atmosphere is used. A reducing atmosphere is usually preferred as the oxides that are present on the surface of the atomized powders get reduced during sintering. Depending upon the sample the sintering temperature, time and atmosphere are selected. During sintering the lubricant evaporates and there is reduction in the surface area of the sample. The pores in the green sample get reduced and this occurs through inter-particle bonding brought about by the atomic motion at the sintering temperature. As sintering proceeds, the original inter-connected porosity is reduced, closed pores are formed, and the overall shrinkage is controlled to ensure the final dimensions of the compact come within the required engineering tolerances.

2.4.1. Advantages of Powder Metallurgy

Powder metallurgical process is used widely because of its advantages over the other processing methods that are available. The P/M processing is competitive to other commercial fabrication technique like casting, stamping, or machining [16]. The Venn diagram shown in the Figure 2.15 shows the ideal areas where P/M process is advantageous over the other techniques [17]. The P/M process can produce simple or complex parts that are close to the final dimensions at a production rate which can range from a few hundred to a few thousand parts per hour. As a result, the final product requires only minor, if any, machining is required. Depending upon the application the P/M parts may require be sizing or coining for closer dimensional control and for both higher density and strength. Also, during production one must take care of the productivity, tolerances and automation. Through the P/M technique, it is possible to

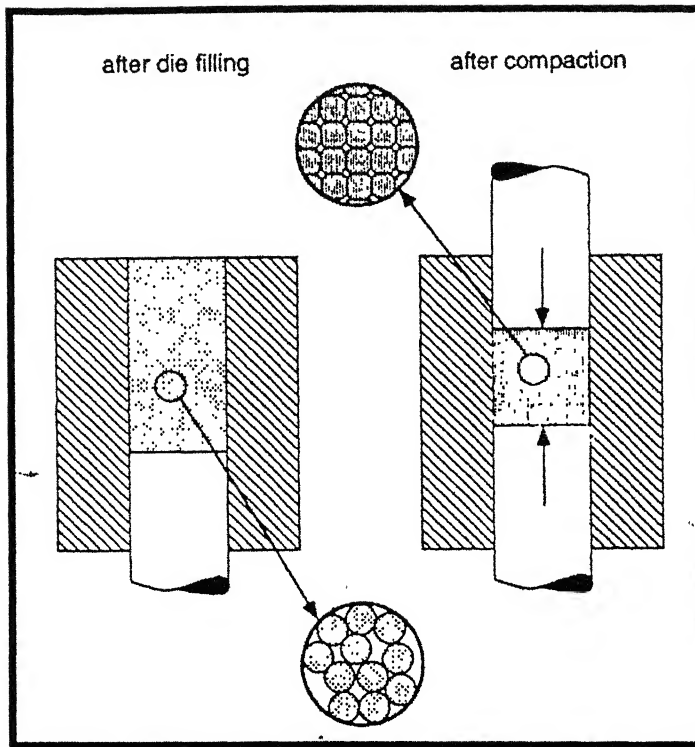


Figure 2.14. Densification during compaction by changes in particle arrangement and shape [15].

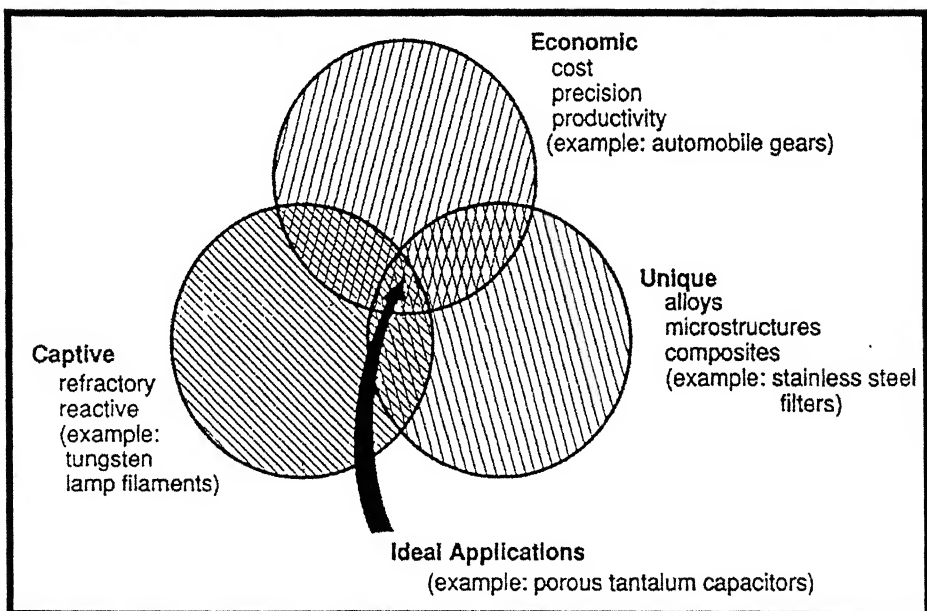


Figure 2.15. Ideal application areas using P/M [17].

process all the alloys, which are not possible by other techniques. The segregation and machining problems that are there in casting are also removed by P/M technique. The main advantages of P/M processing are summarized below:

- Minimizes or almost eliminates machining
- Material loss is eliminated or is very less
- Production cost is less
- Maintains close dimensional tolerances
- Allows the production of a variety of alloys
- Produces good surface finishes
- Provides materials which may be heat-treated for increased strength or increased wear resistance
- Provides controlled porosity for self-lubrication or filtration
- Facilitates manufacture of complex or unique shapes which would be impractical or impossible with other metalworking processes
- Suited to moderate to high volume components production requirements
- Offers long-term performance reliability in critical applications [18].

2.4.2. Limitations of P/M

There are some drawbacks of P/M processing which should be mentioned along with the various advantages that are mentioned. The main drawback of the P/M process is the production of high purity metal powders. The lack of simple methods of obtaining alloys powders of steels, bronzes, brasses, etc. also impose some restriction in the use of P/M. The P/M components that are fabricated have inherent pores in them and this leads to the degradation of the corrosion and oxidation properties. P/M products possess comparatively poor mechanical properties such as, impact strength, and elongation etc because of the presence of porosity. Hence, selection of the sintering temperatures becomes very critical to achieve high density. This requires high precision furnace that add to the cost of the process [19]. Hence for acquiring the economic benefit of P/M process it is essential to have a large volume production. The shape and size of the end products depends on the die and hence controlling the shrinkage in the sample during sintering is difficult. Also this technique can be used in applications where the quantity of

production is more. If the quantity of production is less, then the die cost and other conditions will increase the cost of productivity. The comparison of the P/M process with the other processes is mentioned in the Table 2.3 [19].

2.4.3. Application of P/M

The P/M products find a variety of applications including structural components, controlled porosity applications, electrical and magnetic applications, thermal and high temperature applications, corrosion resistant applications etc. P/M parts are used widely in aerospace and automotive application. As discussed before, the reasons for using P/M parts so widely are because of good tolerance, low cost, net shaping, high production rates, and controlled properties. The various applications of P/M technique, the product requirements and the material and processing technique are given in the Table 2.4 [19].

2.5. Sintering

Sintering is binding the particles together at high temperatures. Sintering may be considered the process by which an assembly of particles, compacted under pressure or simply confined in a container, chemically bond themselves into a coherent body under the influence of an elevated temperature. The temperature is usually below the melting point of the major constituent [20]. Sintering can be understood as a thermally activated material transport in a powder mass or porous compact, decreasing the specific surface by growth of contacts, shrinkage of pore volume and change of pore geometry [15]. Sintering can also be defined as a thermal treatment for bonding of particles into a coherent predominately solid structure by mass transfer events that usually occur on the atomic levels [21]. The driving force for any solid state sintering is the decrease in the total surface energy, which occurs by reduction in surface area with concomitant formation of inter-particle bonds. Accompanying the inter-particle bonding are significant changes in the pore structure and compact properties such as strength, ductility, conductivity, magnetic permeability, and corrosion resistance. There are several variants that affect a sintering process such as the presence of multiple phases, application of pressure, sintering time, sintering temperature, particle size, presence of activators etc. Based on

Table 2.3. Comparison of P/M and competitive production techniques [19].

Technique	Advantages versus P/M	Disadvantages versus P/M
Cold forming	Faster production Higher strength Good surface finish	Lower precision Shorter tool life Limited materials
Extrusion	Long parts Smooth surface Rapid production	Constant cross section Lower precision High energy consumption
Stamping	Flat, high precision High production rates Large area parts Precise feature location	Single level, thin parts only Limited materials Waste, rough edges Small features are difficult
Casting	Widely employed technique Small to large size range Low set-up cost	Not useful for refractories Flashing, parting line Heterogeneous, pores, defect
Hot forging	High mechanical properties Complex shapes and large sizes Fast production	Flash and material waste Poor dimensional control Inclusions and blemishes
Machining	Most all materials and shapes Used for wide size range High precision Short lead time, no tooling	Waste Low productivity Non uniform properties Costly, labor intensive

Table 2.4. Applications of powder metallurgy [19].

Applications	Materials	Requirements
Automotive	Fe-C-Cu, Fe-C, Fe-C-Ni, Fe-C-Ni-Mo	Light weight, precise dimension, shape complexity
Electrical: (i) <i>Electrodes</i> (ii) <i>Electrical contacts</i> (iii) <i>Superconductor</i>	Cu-Al ₂ O ₃ , Cu-Cr, W-Cu, WC-Cu Ag-W, Ag-Mo, Ag-Ni, Ag-Ni-C, Ag-WC, Ag-CdO Nb ₃ Sn, Nb ₃ Al, Nb-Ti, Nb ₃ Ge	Tailored thermal properties, good conductivity
Magnetic	Fe-Si, Fe-P, Fe-Ni, Ni-Fe-Mo, SmCo ₅	Magnetic performance, environmental resistance
Aerospace	<i>Superalloy:</i> IN-100, Rene 95, MA 754, MA 6000, MA 956 <i>Aluminum:</i> Al-Cu-C, Al-Mg-C, Al-Li-Cu, Al-Fe-Cr, Al-Ni-Co <i>Titanium:</i> Ti, Ti-6Al-4V, Ti-6Al-6V-2Sn, Ti ₃ Al	High specific modulus, fatigue and fracture strength, light weight, shape complexity, creep resistance, dimensional precision
Medical	Co-Cr-Mo, Ti-6Al-4V, 316L	Uniform alloying, corrosion resistance, light weight
Dental	Ag-Sn-Cu, Co-Cr-Mo	Aesthetics, shape complexity

Nuclear	Zr-Sn-O-Fe-Cr-Ni, Zr-O-Sn-Fe-C, B ₄ C, Eu ₂ O ₃	Low absorption coefficient
Cutting tools	WC-Co, Wc-TiC-Co, HSS, Si ₃ N ₄	High wear resistance, high abrasion resistance
Porous Parts: (i) <i>Filters</i> (ii) <i>Bearings</i>	Cu-Sn, 316L, Monel Cu-Sn, Cu-Sn-P	Small pore size, uniform pore distribution, corrosion resistance
Ordnance: (i) <i>Missile nose cones</i> (ii) <i>Kinetic Energy Penetrator</i> (iii) <i>Military vehicles</i>	Ti, Ti-6Al-4V W-Ni-Fe, W-Ni-Cu-Fe AISI 1340, AISI 4600	Full density, net shaping

the application of pressure sintering is divided into two major classes as pressure assisted and pressureless sintering. Most of the sintering operations are performed in the absence of external pressure called pressureless sintering. But for many high performance applications, high densities are attained by means of an external pressure during sintering. The Figure 2.16 shows the various types of sintering operations that are used [21].

For understanding the basic concepts of sintering, let us consider the simplest approach of two spherical particles that are in contact with each other as shown in Figure 2.17 [17]. In the powder compact, there will be many such contacts as shown in the figure. As the sintering process progresses the bonds at the contacts enlarge and at each contact a grain boundary grows to replace the solid-vapor interface. If the process prolongs for a longer time then these two particles will coalesce to form as a single particle of 1.26 times the original diameter.

There are various mechanisms proposed for the particle diffusion at the neck area. The various processes that can occur at the neck area during sintering are shown in the Figure 2.18 [15]. There are three main stages that take place during a normal sintering operation. During the initial stage point contacts in the particles are transformed into sintered bridges called as necks. After sometime the neck growth takes place and the grain boundaries are formed between two adjacent particles in the plane of contact. In the second stage the pore structure becomes smoother and has an interconnected, cylindrical nature as the properties of the compacts develop. A coherent network of pores is formed at the grain boundaries and a new microstructure develops. In the final stage of sintering, the isolated pores become spherodised. The places where the gases cannot be diffused out are enclosed and further densification becomes impossible as soon as the gas pressure reaches equilibrium with the surface tension. The various stages of sintering are shown in the Figure 2.19 [15].

2.6. Solid-State Sintering

The driving force for solid state sintering is excess surface free energy. Sintering is a complex process and for any given metal and set of sintering conditions there are likely to be different stages, driving forces and material transport mechanisms associated with the process.

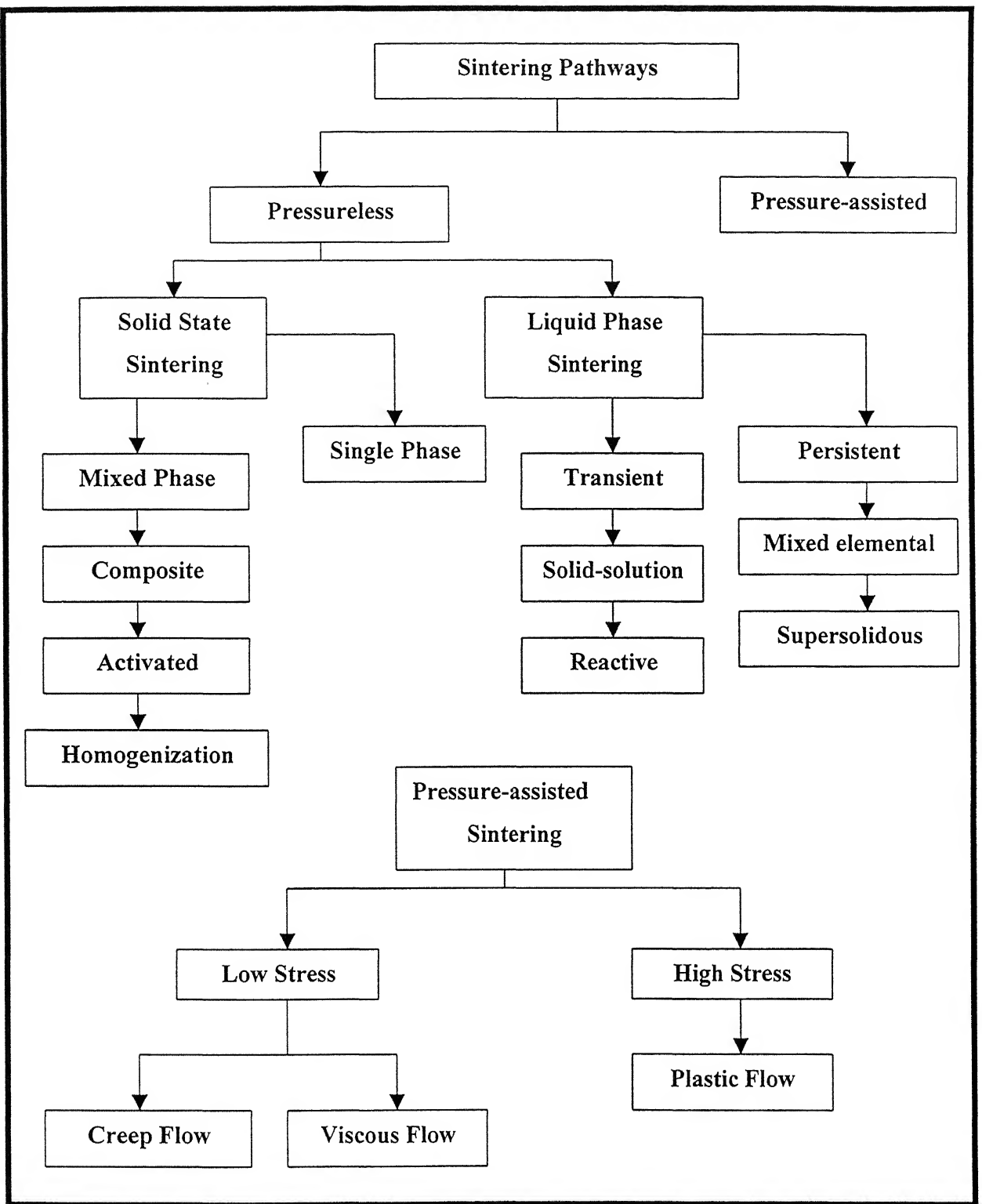


Figure 2.16. Map to various sintering processes [21].

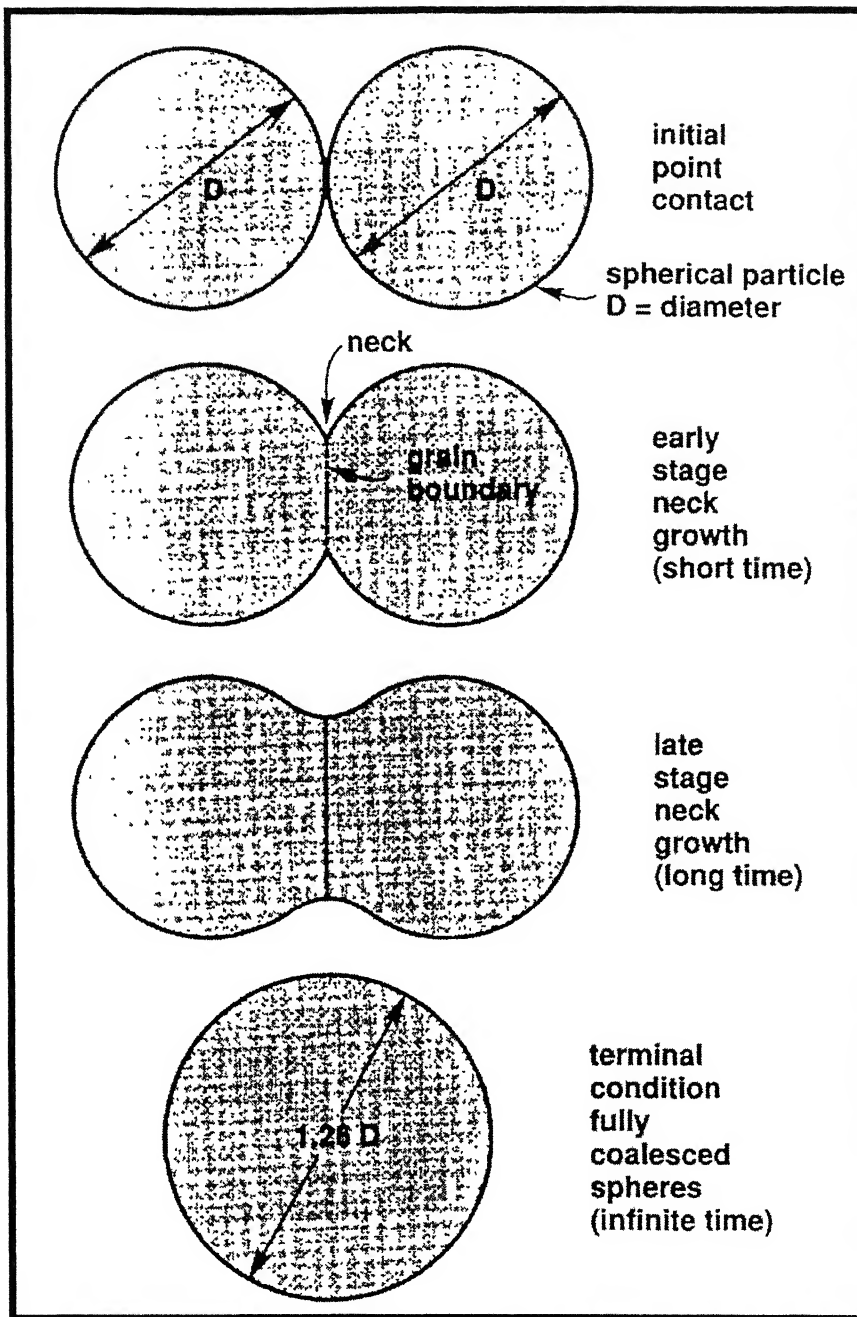


Figure 2.17. Two sphere sintering model [17].

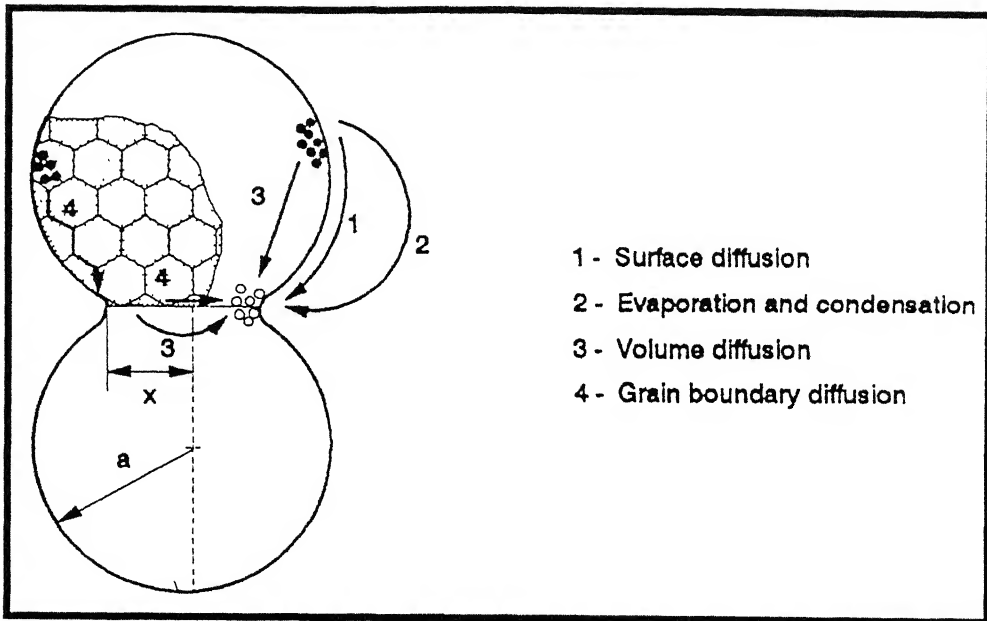


Figure 2.18. Possible sintering mechanisms at the neck area [15].

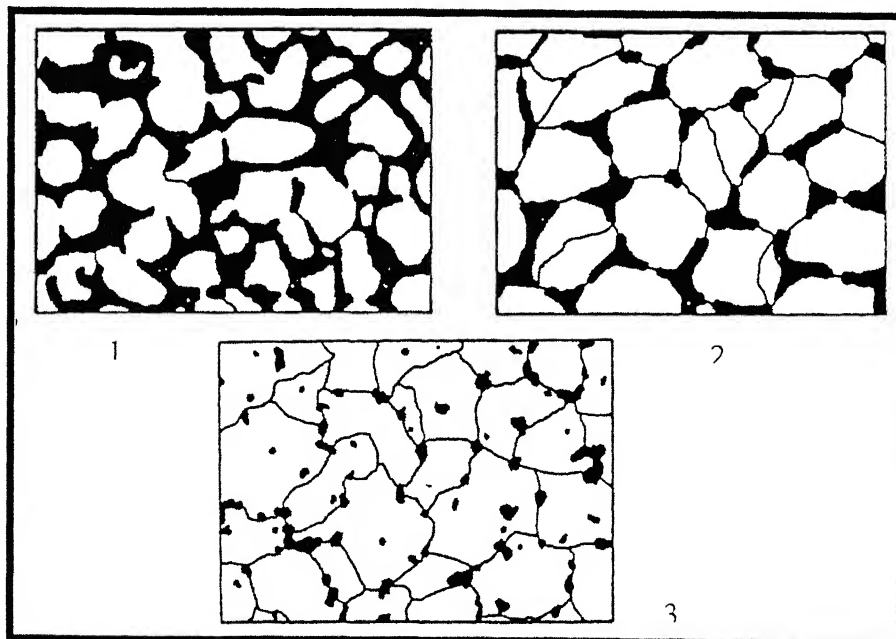


Figure 2.19. Schematic sketch showing various stages of sintering [15].

2.6.1. Different Stages of Solid-State Sintering

One of the basic aspects of sintering is that it usually takes place at a constant temperature (or at least a major part of it) and the time is varied to achieve certain result. Consequently, it becomes useful to attempt to describe the stages of sintering in terms of their relative order with respect to time. In Hrischhorn's [20] discussion of this subject, sintering is divided into six stages:

- (i) Interparticle bonding among particles
- (ii) Neck growth
- (iii) Closure of pore channels
- (iv) Rounding of pores
- (v) Pore shrinkage (densification)
- (vi) Pore coarsening.

However, the problem in describing the different stages is that, the sequence and extent of the stages depends on the green compact. Green compact may contain high amount of porosities where the pores are interconnected or they may be near to theoretical density. In the second case the pores are isolated. As a result of that the stage two and three would be minimized or entirely absent. We will now describe the six stages individually in some details.

Interparticle Bonding

Bonding takes place very early in the sintering process as the material heats up. Transport of atoms at particle contact points leads to the establishment of physical bonding and grain boundaries at these points. The essential condition for this bonding is the intimate contact between the particles. However, there are, of course, many such place in a pressure formed compact, but even in a mass of loose powder there is contact between particles sufficient in magnitude to allow bonding. These initial bonds are developed very rapidly – even as the compact is being heated to temperature. This stage of sintering does not lead to any dimensional change of the material. But bonding in this stage imparts a high degree of coherency and integrity to the material, which is extremely important. This can be proved by the achievement of high strength and hardness even after relatively short exposures to an elevated temperature. It is quite obvious that, greater the original

density of the material, the greater the amount of contact area and potential grain boundary area. Moreover, this stage plays an important role in the production of high porosity material. It should be remembered that in such case, the sintering process might only lead to this one stage of sintering only.

Neck Growth

It is the second stage of sintering and is related to the first stage of initial bonding. Continuing mass transport leads to the development of distinct “necks” between particles, growing from the initial bonds. The newly formed bond areas are termed necks. In the second stage, the neck grows in size. This stage greatly increases the strength of the compact but does not involve any densification. The interconnected porosities, which are present as somewhat irregular channels are turned into smooth channels after this stage. Although neck growth is generally accepted to take place rather rapidly and early in the sintering process, in fact its continuation may lead to its overlap in some later stages. This is generally seen in stage three and five. Though spherical particle model is assumed for simplification, it is to be remembered that, the original powder systems are much more complex. Neck growth is also illustrated in terms of a three-sphere model in Figure 2.20.

Pore Channel Closure

This stage represents the major change in the nature of the porosity in the sinter mass. Continued neck growth can cause pore channels within the compact to be closed, leading to isolated porosity. It is very important to control this event in sintering powder metallurgy products, which utilized interconnected porosity – for example, filters, self-lubricating bearing, etc. However, pore shrinkage in stage five can also lead to channel closure by causing new contacts to be formed among pore surfaces. As a result, this stage may proceed for some time and overlap stage four and five.

Pore Rounding

Pore rounding may be considered a natural consequence of neck growth. As neck growth reaches an advanced stage, the material transported from the general particle surfaces to the neck regions results in a smoothing of the pore walls (reduction of surface

area). No pore shrinkage is necessary for pore rounding, although it too may be taking place during the same time. Though the rounding process pertains both to isolated and interconnected porosity; however it is usually considered with respect to the former. It is possible to achieve almost perfectly spherical pores by allowing sufficient time at suitable temperature. This can be an important structural change with respect to improving the ductility and toughness of the sintered compact. This stage of sintering is illustrated by the idealized three-sphere models in Figure 2.20. But, it should be noted that, it is possible to carry out sintering for a given material without this stage taking place to any significant degree.

Pore Shrinkage

As sintering progresses, the pores in the compact may begin to shrink in size and decrease in number, resulting in densification. This stage must involve extensive diffusion and annihilation of vacancies. Not all porosity can be eliminated during this stage of sintering; some residual pores will be left (particularly inside of grains) even after very long sintering times. For single component systems, densification may be equivalent to pore shrinkage, but in more complex materials other processes can lead to both shrinkage and expansion. Densification in this process involves the movement of solid into the porosity and movement of any gas in the porosity to the external surfaces. Pore shrinkage becomes less important as a stage of sintering with increasing density of the green compact. An example of a sintered structure in which significant pore shrinkage has occurred is shown in Figure 2.21. This material is Mo whose green density after isostatic compaction was 70% theoretical. After sintering at 1850°C for 9 h, the density increased to 98% of its theoretical density. Note that most of the residual porosity is in the interior of grains and that the grain size is about 30 μm , which is an order of magnitude larger than the average particle size (3 μm) of the starting powder.

Pore Coarsening

This stage is not considered to be very important in most commercial sintering operations. When it occurs, it involves an increase in the size of some of the larger pores and concurrent elimination of some smaller pores. No net change in the pore volume

fraction is involved, so the average distance between the pores is increased. Hence, no densification of the material is associated with this stage. In many respects, this microstructural change is analogous to the precipitate coarsening, which occurs during severe overaging of conventional age-hardening alloys [19]. We have discussed the sintering stages based on the three-sphere model so far. But in many case, for simplification, different sintering stages are shown based on the two-sphere sintering model. We have to remember that, a two-sphere geometry is a starting point for many sintering models [16]. Figure 2.17 illustrates the neck profiles for two spheres initially in point contact at various levels of densification [15]. Volume conversion and surface energy minimization dictate a final geometry of one sphere with a diameter 1.26 times the initial diameter. The bonds between contacting particles enlarge and merge as sintering progresses. At each contact, a grain boundary grows to replace the solid-vapour interface as shown in Figure 2.17 [15].

2.7. Liquid Phase Sintering

Liquid phase sintering is a widely used fabrication process in powder metallurgy for both metallic and ceramic products. Pressureless sintering often requires the presence of liquid to eliminate all porosity or to achieve a desired amount of chemical homogenization. In liquid phase sintering, one of the phases in the two phase sintering system has lower melting point inorder to form liquid. In such a system the liquid formed will enhance mass transport and therefore rapid sintering. Liquid phase sintering may be defined as sintering involving a coexisting liquid and particulate solid during some part of the thermal cycle [22]. The liquid phase during sintering can be obtained by two different ways, one by melting one of the component during sintering or by formation of a eutectic. Also the liquid phase formed may be transient or persistent during sintering depending upon the solubility relationship. Beyond this a prealloyed powder can be sintered by having the sintering temperature between the solidus and liquidus temperatures. This is called as supersolidus liquid phase sintering. The ideal phase diagram for liquid phase sintering is shown in the Figure 2.22 [20]. The main requirements for liquid phase sintering are high melting point difference between the solid phase and the forming liquid phase and there should not be any high temperature

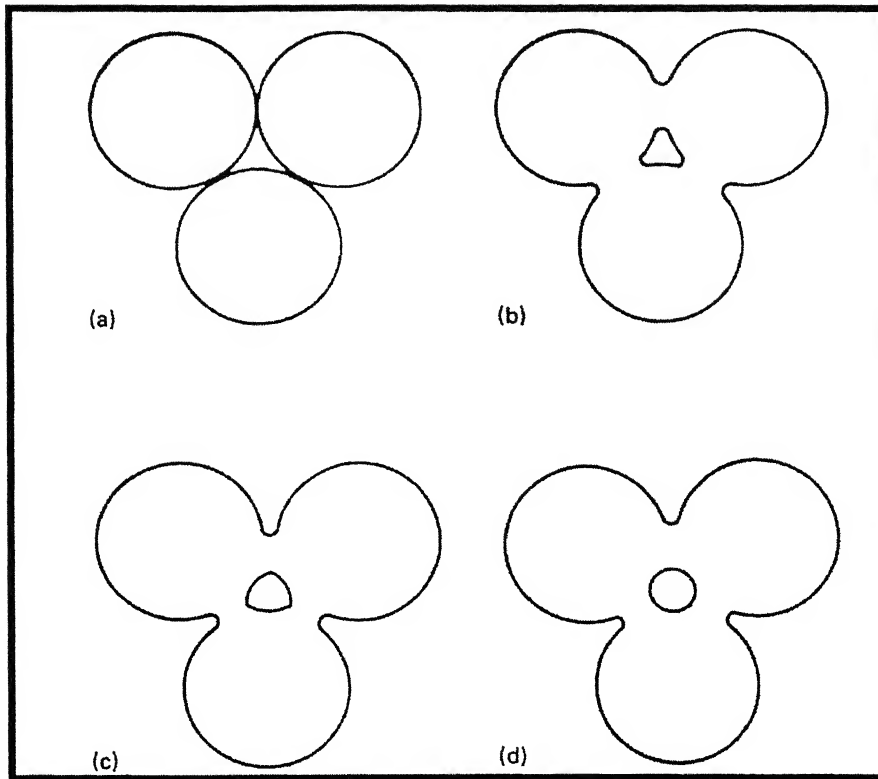


Figure 2.20. Three-sphere sintering models. (a) Original point contacts. (b) Neck growth. (c) and (d) Pore rounding [19].

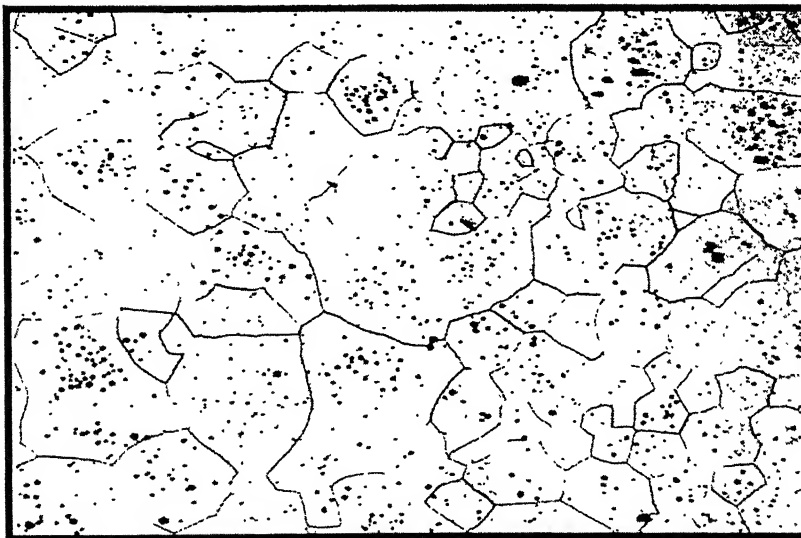


Figure 2.21. Microstructure of sintered molybdenum showing internal porosity [19].

intermediate formation. In order to avoid swelling, the solubility of the solid phase in the liquid phase should be higher than the solubility of liquid phase in solid. The driving force for liquid phase sintering is the reduction in interface energy. The effect of liquid phase on the densification in liquid phase sintering is shown in the Figure 2.23 [21]. The figure shows the stages of liquid phase sintering and the effect of liquid volume on the sintered density. Huppmann et.al studied the elementary stages of liquid phase sintering and reported in detail [23]. In the absence of any liquid, sintering takes place by solid state sintering. On the other hand if there is excess of liquid phase then the compact may not hold its shape and slumping of the sample may occur. When the liquid content is intermittent, then the compact holds the shape but the liquid is not enough to fill the void spaces. In this case densification is increased by rearrangement of particles due to capillary force and then by solution reprecipitation.

The various stages of the evolution of a classical liquid phase sintering microstructure are shown in the Figure 2.24 [21]. The three main stages of liquid phase sintering are: rearrangement, solution-reprecipitation, and final-stage sintering through particle rearrangement. During the initial stages the densification takes place by solid state sintering of the solid particles. As the temperature is further increased, the low melting phase forms liquid and the liquid fraction increases until it gets saturated with the solid phase. The solid particles will move within the liquid and rearrangement process occurs leading to shrinkage. The liquid phase formed acts as a carrier for the solid particles in solution reprecipitation stage, wherein the smaller grains get preferentially dissolved in the liquid and gets reprecipitated on the larger grains. The last stage will be densification of the solid skeleton formed and pore rounding takes place resulting in the final product.

Despite the various advantages of liquid phase sintering, it suffers from certain limitations. Due to the formation of the liquid phase, there is a large change in the final dimensions of the compact and this puts a limitation to dimensional control of the sample during sintering [20]. In addition, the gravity induced microstructural gradients results in non-uniform properties of the sintered products.

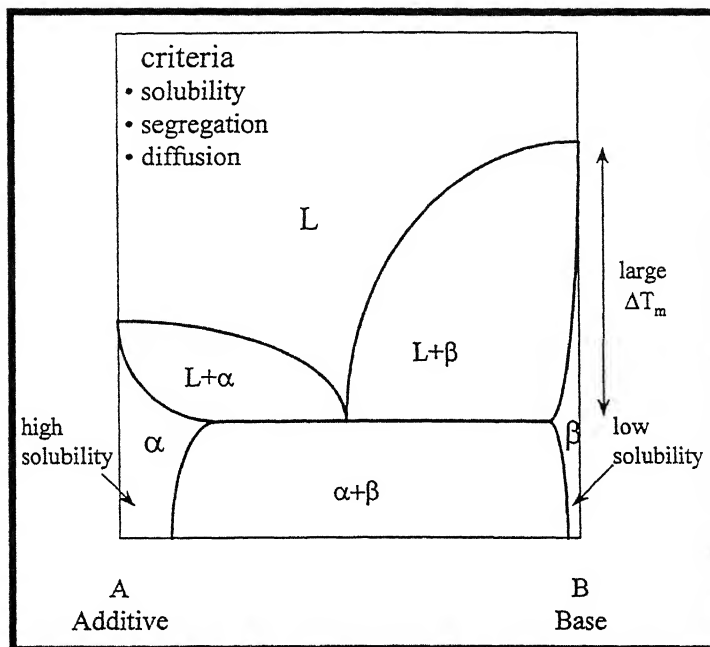


Figure 2.22. Ideal phase diagram for liquid phase sintering [21].

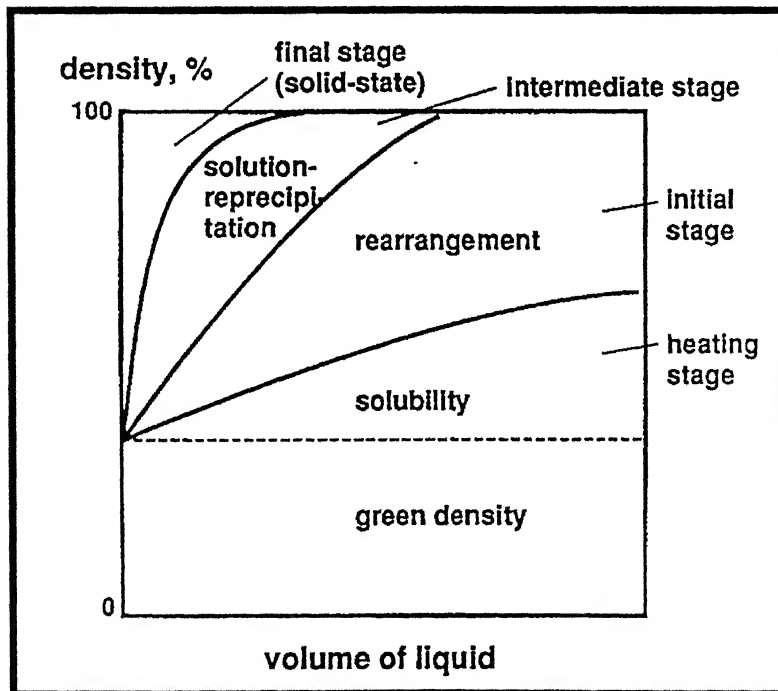


Figure 2.23. A map of density versus liquid content with indications of the dominant regions [21].

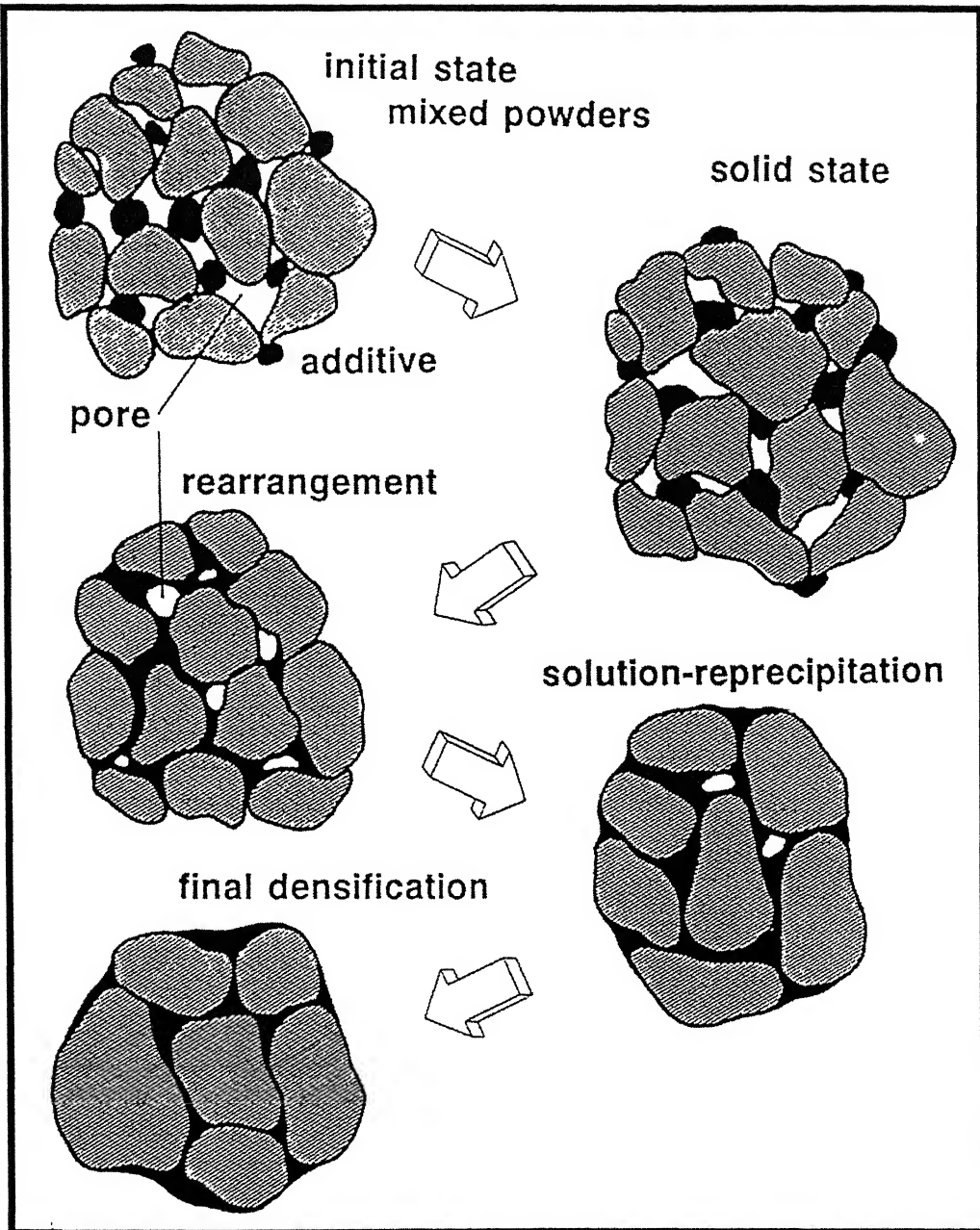


Figure 2.24. Microstructural evolution of classical liquid phase sintering [21].

2.8. Supersolidus Liquid Phase Sintering

There is always a continual move to improve the processing and properties of sintered products. The main driving force for this is to attain lower processing cost and improved products. In case of liquid phase sintering the final properties of the product rely upon the liquid phase and lots of research has been made to improve the properties by altering the properties of liquid phase. The use of prealloyed powders led to the new process in liquid phase sintering called as supersolidus liquid phase sintering (SLPS). SLPS involves heating a prealloyed powder between the solidus and liquidus temperature to form liquid phase [24-25]. SLPS is similar to that of transient liquid phase sintering, but the major difference is the use of prealloyed powders. During SLPS the liquid phase forms within the particles, causing each particle to split into individual grains [21]. The fragmented particles undergo repacking, giving a homogenous distribution of liquid. The resulting sintering rate is rapid once the liquid is formed due to capillary action.

The various stages of densification during SLPS of a prealloyed polycrystalline powder are shown in Figure 2.25 [21]. The steps of SLPS are liquid formation, particle fragmentation, fragment rearrangement, grain packing and sliding, coarsening, and eventual pore elimination by solution-reprecipitation. In the first stage, the melt formation occurs as the prealloyed powder is heated above the solidus temperature. The liquid is formed commonly at the grain boundaries within the particles, in the inter-particle neck region and the grain interior. The liquid volume increases with temperature and at a critical temperature above solidus, the threshold amount of liquid exists along the grain boundaries of a polycrystalline particle [26]. Above the threshold the grain possess enough mobility to rearrange. The rearrangement of solid grains occurs under the influence of the capillary force by the wetting liquid. The second stage of SLPS involves solution-reprecipitation, wherein the small grains dissolve and re-precipitate on larger grains. In the final stage the solid skeleton forms and densification is slow as it is controlled by solid-state diffusion. The increase in liquid phase formation will reduce the viscosity of the solid liquid mixture and hence densification increases. But the main problem in increasing the liquid fraction too high is loss of dimensional precision.

When compared with conventional liquid phase sintering (LPS) supersolidus liquid phase sintering (SLPS) shows improved properties. Table 2.5 [28] presents

Table 2.5. Comparison of LPS and SLPS [25].

Feature	LPS	SLPS
Powder type	Elemental powder mixture	Prealloyed
Melting	One elemental powder melts or melting by reaction between constituents	Partial melting of alloy particles
Liquid location	Between particles	Mainly within polycrystalline particles (results in fragmentation)
Dihedral angle	Variable system dependent	Low
Liquid volume fraction	Mainly determined by composition not temperature	Depends on both temperature and composition according to lever rule
Solid-liquid segregation	Solid grains settle in heavy alloys like tungsten	Negligible settling

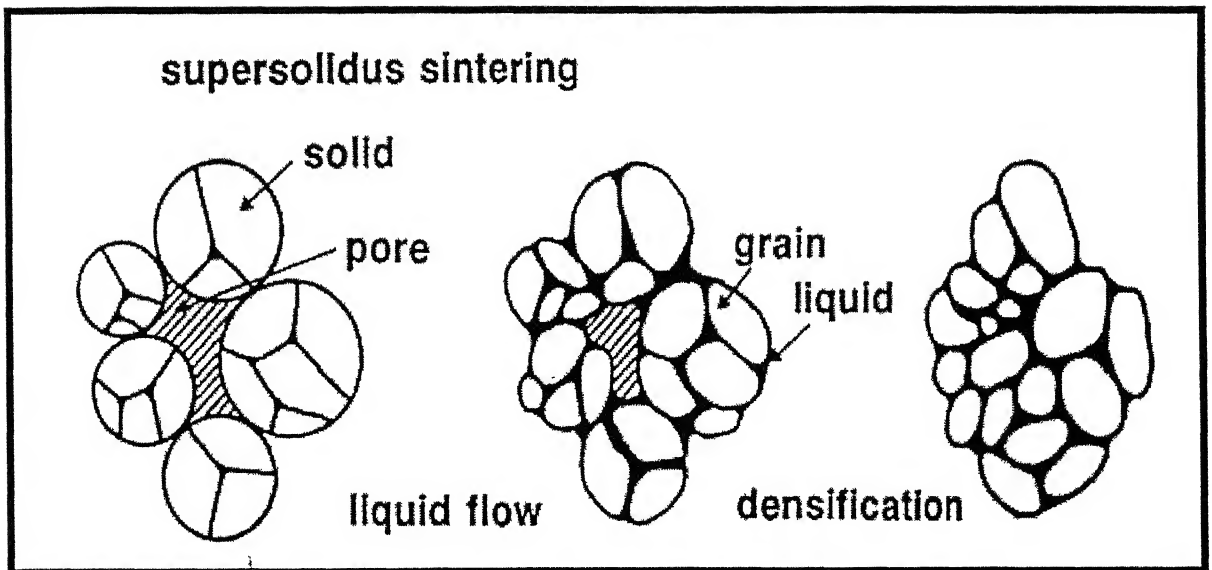


Figure 2.25. SLPS of a prealloyed polycrystalline powder [21].

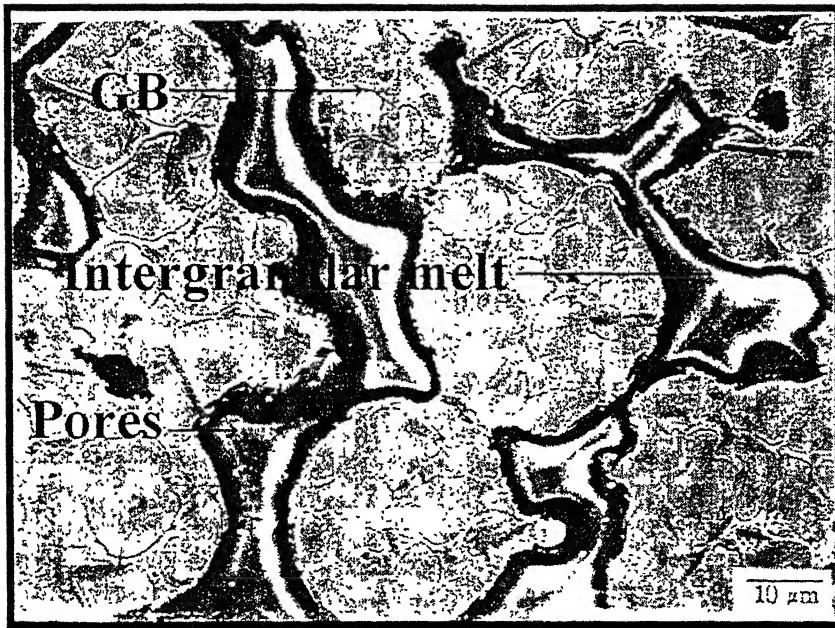
the comparison of SLPS with LPS. SLPS is possible only with two-phase or multiphase systems using prealloyed powders, while in LPS elemental powders are used. The liquid is formed between particles in conventional LPS while it is formed within the particles in SLPS. The SLPS systems show lower dihedral angles than most of LPS systems. This can be attributed to the similar compositions of solid and liquid phases and low solid-liquid interfacial energy.

2.8.1. Previous Research on SLPS

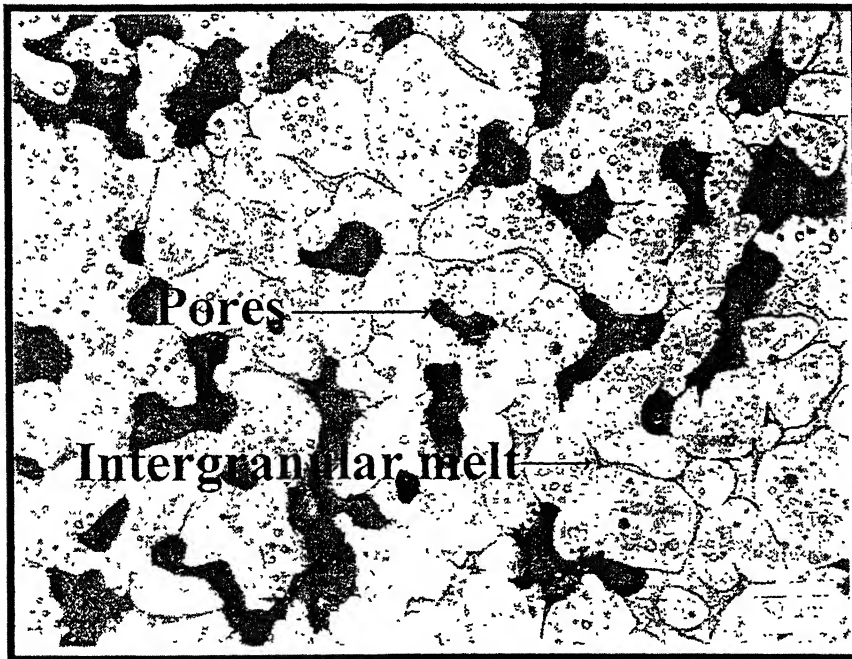
The first work on SLPS was reported by Westerman [29] on prealloyed nickel-base superalloy. He noticed that near theoretical densities were obtained by incipient melting of grain boundaries. The mechanism of SLPS was explained by Lund and Bala [27]. They suggested that mechanisms responsible for densification included,

- (i) redistribution of liquid formed due to melting at particle contacts
- (ii) flattening of the wetted particle contacts by a solution-precipitation mechanism
- (iii) grain growth due to solution-precipitation leading to release of intergranular liquid
- (iv) pore elimination due to the escape of the entrapped gas by diffusion.

Extensive work on densification mechanisms and microstructural evolution during SLPS of prealloyed powders was carried out by Tandon [24]. He worked on sintering mechanisms used for a wide range of alloys like Ni-based super alloys, austenitic stainless steel and bronze powders. The SEM micrograph of a Ni-based superalloy after showing liquid formation sites is shown in Figure 2.26. The same author interfaced the effect of boron additions in Ni-based superalloy and obtained sintered densities upto 96% theoretical [30]. Lal worked on mechanisms and mechanics of shape loss during SLPS on various prealloyed powders, including bronze, 316L stainless steel and T15 tool steel. He investigated the shape loss during SLPS and rationalized the processing and material factors with regard to distortion [28]. The same author studied the microstructural evolution and the sintering response of powder mixtures of low and high melting alloys. The role of alloying elements, composition, sintering time and temperature on the extent of homogenization and densification were observed. The effect of brazing temperature



(a)



(b)

Figure 2.26. SEM micrograph of (a) Ni-base superalloy and (b) stainless steel showing liquid formation sites [24].

पुरुषोत्तम काशीनाथ केकर पुस्तकालय

भारतीय प्रौद्योगिकी संस्थान कानपुर

141869

अवाप्ति क्र० A-----

and weight ratio of the constituent alloys were studied and compared with the effects seen during sintering [31].

Lal *et al.* [32] examined densification during SLPS of a mixture of two Ni-base superalloys. To one of the mixtures boron is added and it was observed that it had a lower melting temperature. This enhanced the densification of the sintered component. German examined the interplay of processing variables to obtain full-density, distortion-free shapes from prealloyed powders [33]. Extensive research has been carried out in order to understand the densification during SLPS by modeling. Liu *et al.* [34,35] modeled for capillary action and densification for supersolidus liquid phase sintering [34,35].

2.8.2. Parameters affecting SLPS

The key parameters that affect SLPS are temperature and powder characteristics, as these two parameters dictate the amount of liquid that is formed during sintering. Temperature is the main parameter that determines the density of the product after SLPS. Unlike solid state sintering, SLPS is a very temperature sensitive process. Even a small fluctuation in the temperature may lead to excess of liquid formation and increased shrinkage in the sample. The effect of temperature on sintering of nickel-based superalloy is shown in the Figure 2.27 [22]. It is seen from the figure that densification takes place immediately after the critical temperature is reached and prolonged temperature after that leads to minor change in sintering and often leads to decrement in properties. Also while selecting the critical temperature care should be taken, so that the temperature is within the solidus and liquidus temperature. The binary phase diagram shown in Figure 2.28 [21] shows the effect of temperature on the liquid phase formation and how to calculate the critical temperature of sintering. The sintering temperature T should be between the solidus temperature T_S and liquidus temperature T_L , so that the liquid formed can be calculated through Lever rule. By knowing the composition X_L and X_S , the amount of liquid phase can be calculated by finding X_A , the composition of solid and liquid phases at temperature T . The holding time during sintering is another parameter, which determines the final properties of the sintered sample. Figure 2.29 [21] shows the effect

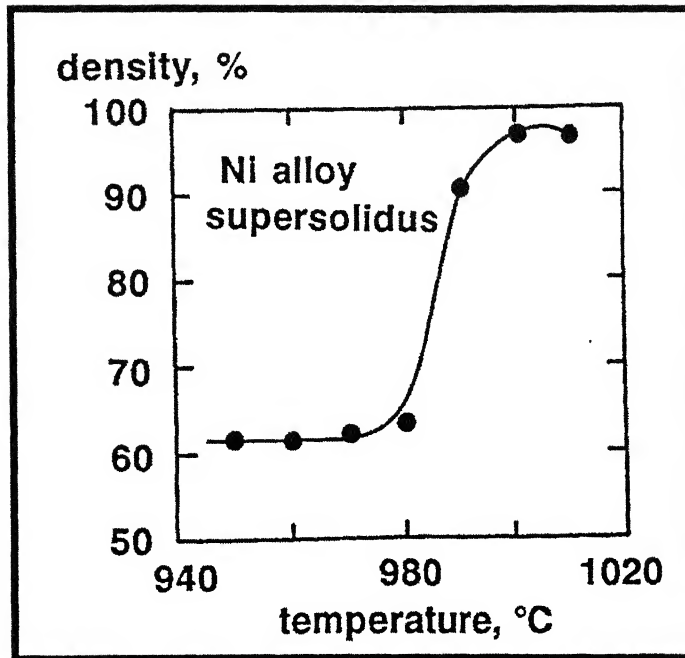


Figure 2.27. Variation of sintered density with temperature in a Ni based super alloy during supersolidus liquid phase sintering [22].

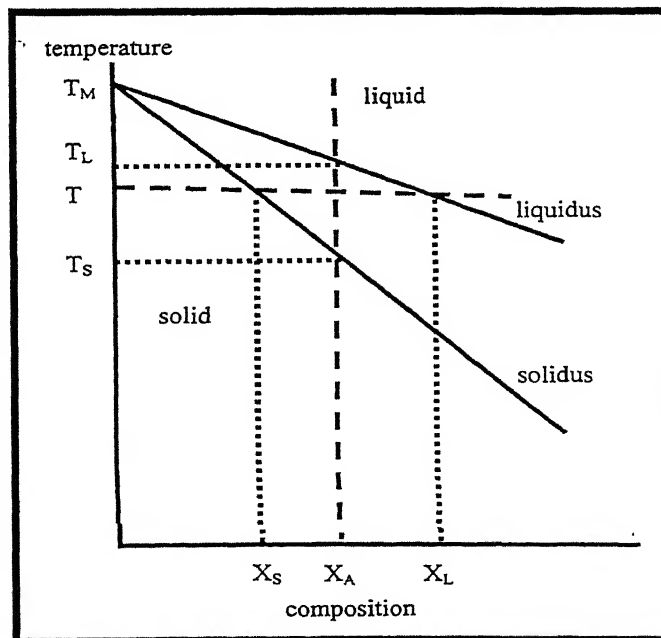


Figure 2.28. Binary phase diagram showing desired features for SLPS processing at composition X_A and temperature T [21].

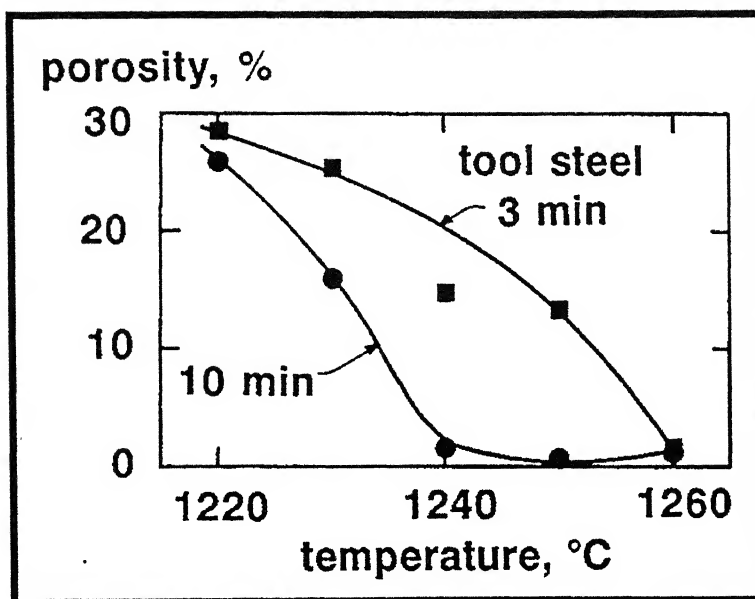
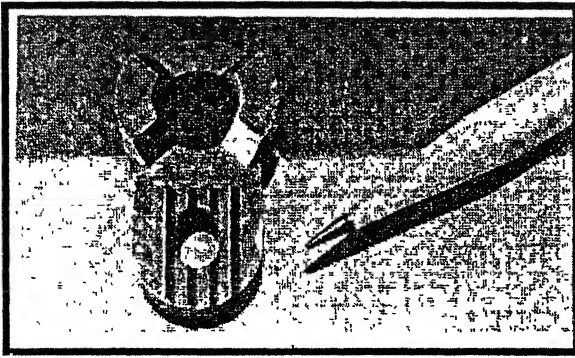


Figure 2.29. Effect of holding time on sintered density during SLPS [21].

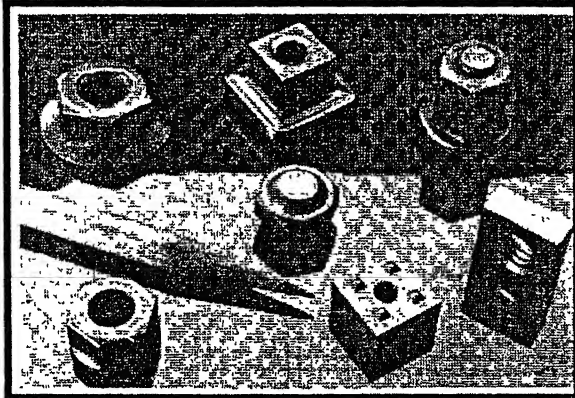
of holding time during SLPS on tool steel. It is seen that holding for 3 mins or 10mins does not have any effect on the sintered density. If the holding time is more than the required the grain coarsening may occur leading to decrement in the sintered properties. SLPS works with relatively coarser grains. This is an advantage when compared with classical LPS, which requires grains of average size 1 μm . Coarser grains have less contamination and are easier to handle. However, smaller particle size gives better densification, especially at temperatures below the optimal temperature. But once the optimal temperature is reached particle size hardly plays a role on densification. Particles as large as 80 μm can be used for SLPS [21]. Another parameter affecting the SLPS is the alloy modifications and additives. The additives will segregate in the grain boundaries and alter the liquid formation temperature and liquid quantity. They may be utilized to improve the sinterability of alloys. The addition often broadens the sintering temperature window and thereby helping in controlling the sintering [19].

2.9. P/M Stainless Steel

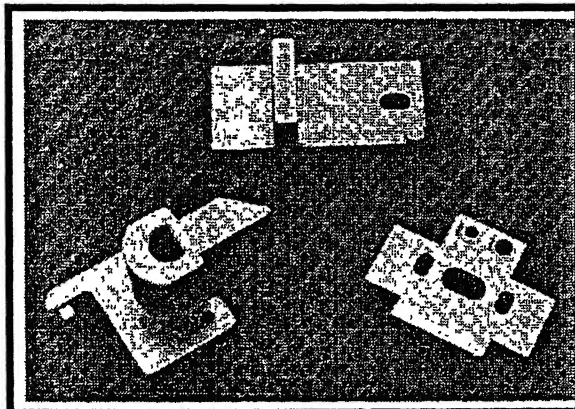
There has been an enormous increase in the requirement of P/M stainless steel as it finds various applications. The growth rate of P/M stainless steel has increased from 4500 short tons in 1996 to 8157 short tons in 2000 [36]. Still this is only a small fraction when compared with the use of wrought stainless and hence the powder producers are still working on the further development of P/M stainless steel. Optimum sintering parameters are also being developed, as stainless steel part producers continue to improve the control of their sintering operations. The various grades of stainless steel powders and their compositions are shown in the Table 2.6 [14]. Among the various grades most widely used P/M stainless steel parts are made up of 300 (austenitic) series and 400 (ferritic) series. The 300 series are typically used in applications that require good corrosion resistance, while the ferritic grades are used in applications that require good magnetic properties and thermal conductivity. The characteristics of various grades of P/M stainless steel, their description and designation are shown in the Table 2.7 [14]. The selection of various grades for the applications is based on a number of considerations. Corrosion resistance is the key property for majority of applications as in the case of



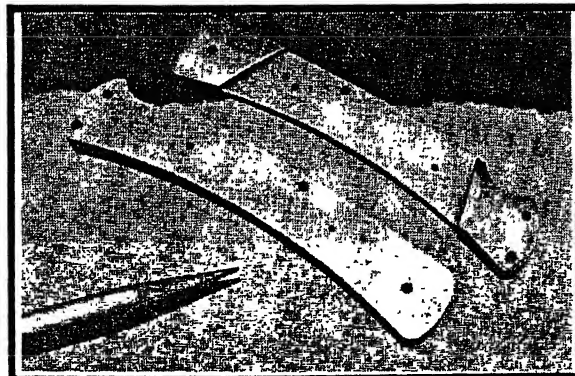
Appliance Parts



Hardware Parts



Office-machine Parts



Miscellaneous Parts

Figure 2.30. Typical examples of P/M stainless steel parts [37].

Table 2.6. Compositions of standard powder metallurgy stainless steel [14].

Grade	Chemical Composition, wt %									
	Fe	Cr	Ni	Mn	S	Si	C	P	Mo	N
303L	Bal	17-19	8-13	0-2	0.15-0.30	0-1	0-0.15	0-0.2	-	0.2-0.6
304L	Bal	18-20	8-12	0-2	0-0.30	0-1	0-0.03	0-0.45	-	0-0.03
316L	Bal	16-18	10-14	0-2	0-0.30	0-1	0-0.03	0-0.45	2-3	0.2-0.6
409L	Bal	10.5-11.75	-	0-1	0-0.30	0-1	0-0.30	0-0.04	-	0-0.03
410L	Bal	11.5-13.5	-	0-1	0-0.30	0-1	0-0.30	0-0.04	-	0-0.03
430L	Bal	16-18	-	0-1	0-0.30	0-1	0-0.30	0-0.04	-	0-0.03
434L	Bal	16-18	-	0-1	0-0.30	0-1	0-0.30	0-0.04	0.75-1.25	0-0.03

Table 2.7. Characteristics of various grades of P/M stainless steel [14].

Designation	Description	Characteristics
303L	Free machining austenitic grade	Designed for parts that require secondary machining operations. It has Strength and hardness. This alloy has marginal corrosion resistance. Sulfur is added for machinability.
304L	Basic Austenitic grade	Most economical of austenitic grades. Used where material cost is the major part of production cost. It has good corrosion resistance than 303L.
316L	Standard Austenitic grade	This offers better machinability and corrosion resistance than 304L. With careful processing it can meet the corrosion resistance of most applications.
317L	Premium Austenitic grade	Has larger content of Mo than in 316L and hence has better crevice corrosion resistance.
409L	Weldable Ferritic grade	A weldable grade of stainless steel having Nb which prevents sensitization. It is a magnetic alloy with good ductility and fair corrosion resistance.
410L	Standard Ferritic grade	It can be readily converted to martensitic grade by addition of C prior to processing. Ductile and machinable in ferritic form, while hard with reduced ductility in martensitic form. Magnetic alloy.
434L	Premium Ferritic grade	Used in applications requiring some corrosion resistance but where economics is the main concern. Better corrosion resistance and machinability than 410L grade.

Table 2.8. Applications of various grades of P/M stainless steel [14].

Application Area	Alloy Grade
<i>Automotive applications</i>	
Exhaust systems, Sensor blades, and Sensor rings Rearview mirror mounts, Brake components, Seat belt locks, Windshield wiper pinions, Manifold heat control valves.	409L, 410L, 430L and 434L
Windshield wiper arms	316L
<i>Hardware</i>	
Lock components, Threaded Fasteners, Fasteners, Quick disconnect levers, Spacers and washers	303L, 304L and 316L
<i>Electrical and Electronic applications</i>	
Limit switches, Magnetic clutches	410L and 440L
G-frame motor sleeves, Rotatory switches, Electrical testing probe jaws	303L and 316L
Battery nuts	430
<i>Industrial applications</i>	
Water and Gas meter parts, Filters, Fuel meters, Clamps, Fixtures, nozzles, shower heads and Window hardware.	303L, 303L, 316L and 316L-SI
<i>Official Equipment</i>	
Nonmagnetic card stops, computer knobs	316L
<i>Miscellaneous</i>	
Coins, Dental equipments, Watchcases, Cam cleats, Can opener gears, Dishwasher components	304L, 316L and 410L

wrought stainless steel. The other additional properties that are considered include magnetic characteristics, mechanical properties (both room temperature and elevated temperatures), machinability and hardenability. The least the raw material cost and ease of production are also taken into consideration. The Figure 2.30 [37] shows some of the sintered stainless steel parts that are used. Automotive parts are the most significant application sector for P/M stainless steel. A substantial quantity is used for making parts possessing controlled interconnected porosity for filtration, flanges and sound attenuation. Also sintered stainless steel parts are used in hardware, appliances and electrical systems. The various areas where the ferritic and austenitic grades are used are shown in the Table 2.8 [14]. The first automotive part made of P/M stainless steel was the rearview mirror bracket, which still holds 15% of the total production of P/M stainless steel. The 430L and 434L alloys were employed for this purpose. The other P/M components that are used in automotive industry include flanges, antilock brake system sensor rings and exhaust systems.

2.10. Corrosion of P/M Stainless Steel

P/M components produced from corrosion resistant alloys such as stainless steels, nickel based alloys and super alloys constitute a small, but rapidly growing segment of the P/M market [38]. These corrosion resistant alloys are used for various applications in aerospace, petrochemical, automotive, chemical processing, medical and recreational fields. The corrosion resistance of these alloys is attributable to the thin, protective oxide layer that is formed on the surface of these alloys when exposed to corrosive atmospheres. Among the various P/M corrosion resistant alloys, stainless steel finds the widest range of applications. There has been a steady increase in the shipment of stainless steel powders [38]. This growth can be attributed to the increasing demand for stainless steel products in making automotive parts, crucibles, lock hardware, appliance parts and filters. The stability of the protective chromium oxide layer depends on the surface morphology of the sample. In the case of P/M stainless steel samples, the surface has many pores and depending on the dimensions of these pores, they act as sites for initiation of pitting/crevice and lead to the breakdown of the surface film. The micrograph of a typical P/M stainless steel sample with pores on the surface is shown in

the Figure 2.31 [39]. In order to reduce pitting and crevice corrosion additions like molybdenum are added. Moreover the corrosion resistance of P/M stainless steels depends upon the processing conditions of the sample. There are several processing parameters that affect the corrosion properties of P/M stainless steel and some of them are summarized below [40]:

- *Influence of iron and steel contamination:* Iron and steel contamination degrades the corrosion resistance of P/M stainless steel. The potential difference between iron or steel and stainless steel results in the establishment of micro galvanic cells. The contamination can take place during mixing/blending, pressing operations, through airborne particles or through inadequate furnace cleaning. Maintaining the furnace clean and having dedicated equipments can avoid this contamination.
- *Influence of carbon and lubricant:* Carbon contamination in the sample will lead to sensitization of stainless steel. When the carbon content increases more than 0.03%, it leads to the formation of chromium carbide precipitates at the grain boundaries. This results in depletion of chromium at the grain boundaries and results in intergranular corrosion. This can be minimized by using proper lubrication, clean furnace and low initial carbon content.
- *Influence of nitrogen and sintering atmospheres:* Dissociated ammonia is used as the sintering atmosphere in several situations, because of its lower cost. This leads to pickup of nitrogen in the sample, leading to sensitization. Chromium nitride is formed at the grain boundaries. This can be minimized by using vacuum sintering or sintering in a reducing atmosphere.
- *Influence of oxygen and water vapor/dew point:* The as received powders contain oxygen, which reside on the surface of the powders. If this is not reduced during sintering, these oxides will provide an easy path for corrosion. Researches [40-41] have carried out work on the influence of oxygen content in the corrosion resistance of stainless steel. It has been concluded that the pitting resistance of the sample degrades due to the contamination of oxygen.
- *Influence of sintering temperature, time and cooling rate:* It has been noted that the corrosion resistance of stainless steel increases with sintering time [39]. This

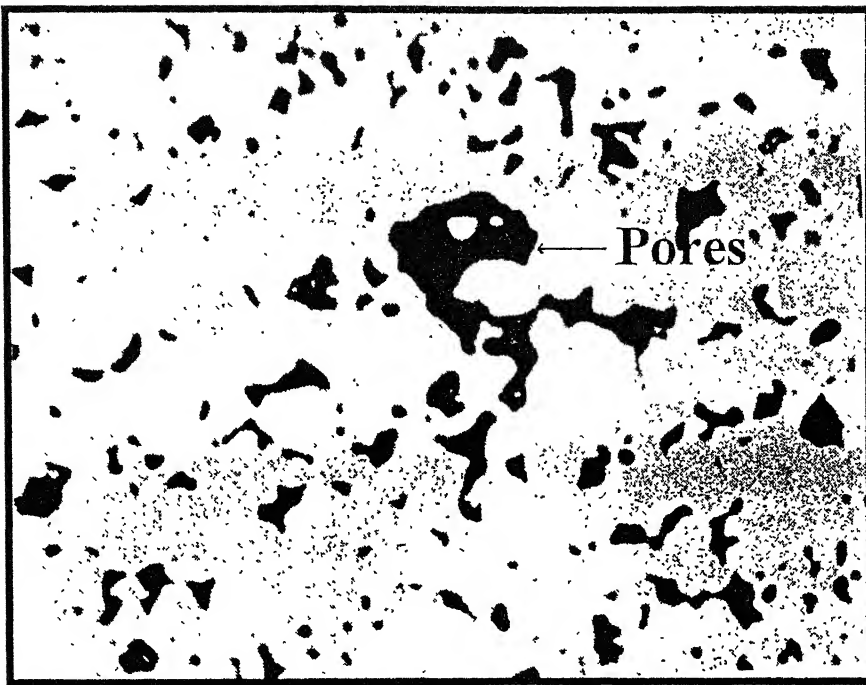


Figure 2.31. Surface of a P/M Stainless Steel Sample [29].

improvement is attributed to the reduced oxygen, nitrogen and carbon levels as the specimen is sintered for a longer time.

Among the various alloys of stainless steel for producing corrosion resistant products, the austenitic and ferritic stainless steel find wide range of applications. The austenitic stainless steel owes its corrosion resistance to chromium, nickel and other passivity enhancing elements. Chromium is the primary element that forms the protective Cr_2O_3 layer, while Ni stabilizes the austenitic phase and promotes repassivation, especially in reducing atmospheres. These alloys are used in applications, which require corrosion resistance and machinability. The ferritic stainless steel is comparatively less heavily alloyed than austenitic stainless steel and usually has inferior corrosion resistance. But these are used in applications where economics preclude use of the austenitic stainless steel. Moreover ferritic stainless steel has better mechanical properties and can also be used in applications that require magnetic properties. Ferritic stainless steels are used extensively in automotive industry for manufacturing components such as mirror mounts, sensor rings, exhaust flanges, support brackets and seals.

2.11. A Review of P/M Stainless Steels

Extensive research has been carried out on P/M stainless steel regarding their sintered density mechanical, corrosion and oxidation properties [42-61]. Tiziani *et al.* [42] studied liquid phase sintering of 316L stainless steel with 20% copper using $\text{N}_2\text{-H}_2$ atmosphere. Copper additions improved the compressibility, sinterability and dimension control of the final component. They reported that the corrosion properties of the sintered component also enhanced due to the addition of copper. Wang and Su [43] added silicon powder to 304L stainless steel and studied the liquid phase sintering behavior of the component. Silicon additions profoundly activated the sintering process by the formation of a eutectic ferrite. They reported that the final product was a duplex stainless steel product with austenite-ferrite structure. P/M Stainless steel components from prealloyed water atomized powders produced by injection molding were investigated by German [44]. The main drawback of injection molding method was that it required rounded particles, for improved packing and sintered density. Sharon *et al.* [45], investigated the corrosion behavior of austenitic stainless steel by adding nickel-based additives. The

corrosion resistance of the sintered stainless steel increased substantially by the addition of 1-5% nickel based brazing powder. This was attributed to the reduction of open interconnected porosity due to the formation of transient liquid phase.

Lei *et al.*[46] examined the effect of oxygen, carbon and nitrogen contents on density, strength and corrosion resistance of 316L prealloyed powders. The corrosion resistance of 304L with tin and copper additives were also studied. Their results suggested that presence of nitrogen in the sintering atmosphere increases the strength but the corrosion properties were degraded. Nayar *et al.*[47] did extensive work on the effect of sintering parameters on the corrosion behavior of 316L stainless steel. The sintering was carried out in three dew points, five hydrogen-nitrogen atmosphere mixtures and three post sintering cooling rates. Based on the studies, the authors defined an optimal sintering atmosphere in nitrogen. Minimum corrosion was reported for sintering in nitrogen atmosphere at high temperatures followed by rapid cooling. Ro and Klar [48] investigated the effect of sintering atmosphere on the corrosion resistance of austenitic stainless steels. They used three atmospheres of dissociated ammonia, hydrogen and vacuum. The maximum corrosion resistance was obtained for the sample sintered in low dew-point hydrogen. Tandon *et al.*[49] studied the mechanical and corrosion properties of nitrogen alloyed stainless steel. The yield and tensile strengths were increased by 2 to 3.5 times compared to the wrought counterpart, with not much degradation in the corrosion resistance. Shay *et al.*[50] studied the corrosion behavior of sintered austenitic stainless steels in hydrogen-nitrogen atmosphere and concluded that presence of nitrogen in sintering atmospheres resulted in the formation of chromium nitride, which resulted in the degradation of corrosion resistance. The authors suggested that for safer option sintering should be carried in a 100% hydrogen atmosphere. Tunberg and Nyborg [51] analyzed the surface reactions during sintering of water atomized stainless steel powders. Surface oxides were formed during atomization and sintering. These oxides were reduced when sintered in a reducing atmosphere or in vacuum.

Smith [52] provided a complete insight on the effect of sintering variants on the material properties of stainless steels. The samples were tested in the sintering atmosphere containing hydrogen-nitrogen and was reported that increase in the content of nitrogen in the atmosphere resulted in increased corrosion rate in the components. The

variation of corrosion resistance with increase in sintering temperature was studied and concluded that the corrosion rate decreases with increase in temperature. Lei and German [53] studied the corrosion behavior of sintered stainless steel with copper and tin additions in sodium chloride solution. They compared the corrosion resistance of premixed and prealloyed samples and reported that the prealloyed samples possessed better corrosion resistance. The corrosion resistance of sintered stainless steels were carried out in various inorganic acids like sulfuric acid, phosphoric acid and nitric acid by Otero *et al.* [54,55]. They proposed a possible mechanism for corrosion of P/M stainless steel and the mechanism of corrosion is shown in Figure 2.32. The same authors also studied the influence of microstructure on the corrosion resistance of austenitic stainless steel exposed to ferric chloride solution [56]. Gabe [57] also analyzed the mechanism of corrosion in sintered parts and the role of the porosity in determining the stability of the oxide film. He further suggested some protection methods to improve the corrosion resistance. Fedrizzi *et al.*, [58] studied the corrosion resistance of P/M austenitic stainless steel sintered in dissociated ammonia atmosphere. Copper was added to the samples and the corrosion resistance was compared. They reported that the alloys containing copper possessed better corrosion resistance.

Ahlberg *et al.* [59] provided insights on the electrochemical corrosion behavior of sintered stainless steels. Both austenitic and ferritic stainless steels were investigated in sulfuric acid. It was reported that the density of the sintered material had no conclusive influence on the corrosion behavior and the surface composition was of greater importance. The authors further reported that the type of corrosion in ferritic stainless steels was general uniform corrosion, despite the large number of pores in the material. Moyer *et al.* [60] investigated an alternate process of obtaining ferritic stainless steel P/M parts by using premixed powders. The authors concluded that the premixed powders provided components possessing better magnetic properties without significant sacrifice of corrosion resistance. A new approach for measuring the corrosion rate of P/M stainless steel by calorimetric method was suggested by Yuan *et al.*, [61]. The results obtained by this method were compared with the salt spray method.

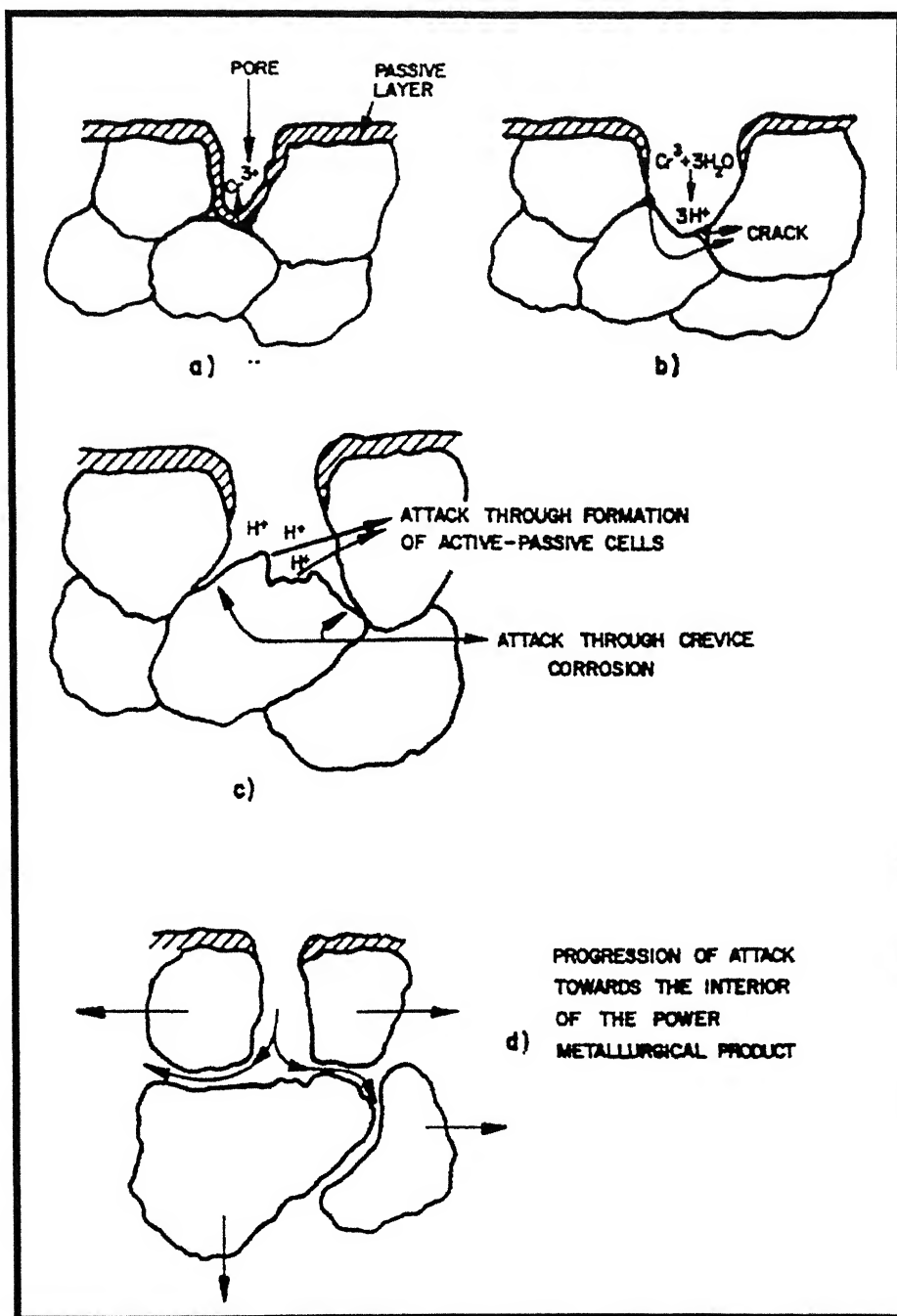


Figure 2.32. Possible corrosion mechanism in P/M stainless steels [55].

2.12. Stainless Steel Based Particulate Composites

Although work has been reported on the corrosion of P/M stainless steels, not much has been reported on P/M stainless steel particulate composites. The particulate particles are added to the straight stainless steel in order to improve the high temperature strength, corrosion and oxidation properties. The process can be defined as the process of strengthening a metal or alloy by incorporating a fine insoluble phase dispersed uniformly throughout the matrix of the parent metal. The particulate particles that are normally used are high temperature oxides such as Al_2O_3 , ZrO_2 , ThO_2 , TiO_2 and Y_2O_3 . These oxide dispersoids have good high temperature properties and impart better mechanical strength, oxidation and corrosion resistance.

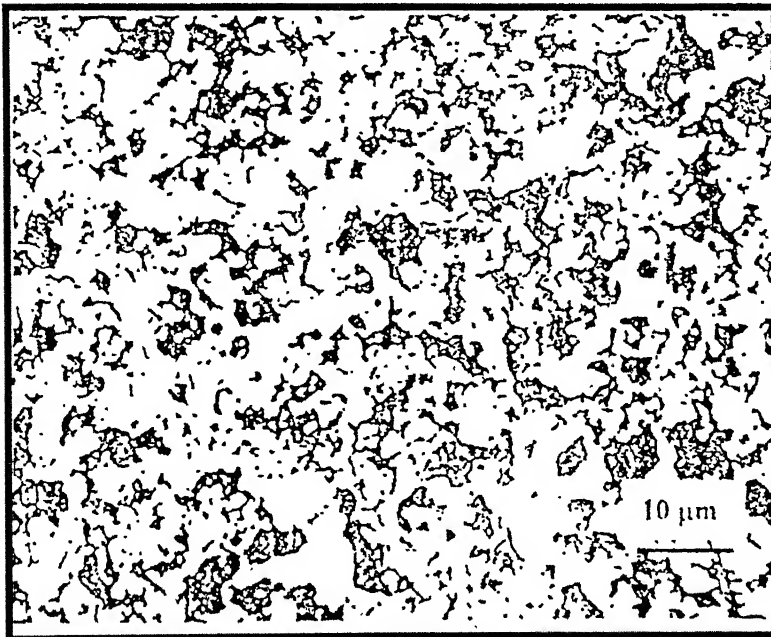
Extensive research was carried out on the effect of Y_2O_3 on the sintering behavior and corrosion resistance of 316L stainless steel by Lal and Upadhyaya [62-64]. Solid state sintering was carried out on 316L austenitic powders and the effect of Y_2O_3 was studied by varying the composition from 0 to 8%. It was observed that the sintered porosities were superior for the Y_2O_3 containing composites than for the straight 316L under identical sintering conditions. This was attributed to the interaction of Cr_2O_3 with the Y_2O_3 dispersoids. Maximum tensile strength was obtained for samples containing 4-volume % Y_2O_3 . The hardness of the samples increased with increasing percentage of Y_2O_3 but the oxidation resistance degraded at higher concentrations. The potentiodynamic polarization studies on the samples showed that the sample with 8-volume % Y_2O_3 was superior. This was attributed to the interaction of Cr_2O_3 with the Y_2O_3 dispersoids. Patankar and Tan [65] studied the role of reinforcement in sintering of 316L/SiC composites. The addition of SiC to the 316L powders resulted in better sintered density. This was attributed to the interaction of SiC with the 316L matrix resulting in the formation of a low melting Fe-SiC phase. The microstructures from Patankar and Tan samples are shown in the Figure 2.33.

The effect of Al_2O_3 oxide dispersoids on the sintering behavior and properties of 434L ferritic stainless steel was investigated in detail by Mukherjee and Upadhyaya [66-69]. Al_2O_3 was added from 0 to 8 volume % in 434L stainless steel samples and subjected to solid state sintering. It was reported that the composites possessing 4 to 6 volume % of Al_2O_3 had higher mechanical properties. The authors conducted

potentiodynamic polarization studies on the samples in 1N sulfuric acid and concluded that the sample containing 8- volume % of Al_2O_3 had better corrosion resistance. This was attributed to the interaction between Cr_2O_3 and Al_2O_3 in the formation of the protective oxide. Further, the authors added phosphorous to the composites and concluded that addition of phosphorous enhances the corrosion resistance of the composite.



(a)



(b)

Figure 2.33. Microstructure showing (a) 316L stainless steel and (b) 316L/SiC composite [65].

Chapter 3

SCOPE OF THE PRESENT WORK

As explained in the previous chapter there has been much work going on the area of P/M stainless steel. Stainless steel is used especially for its corrosion resistance. The main problem in almost all the P/M products is their corrosion resistance due to the inherent porosity present in the P/M products. This implies the importance of the study about the corrosion resistance of P/M stainless steel. The two main types of stainless steel that are used for their wide range of applications are the austenitic stainless steels and the ferritic stainless steels. Hence these two types of stainless steels were selected as the materials for the current work. Austenitic stainless steels are chosen mainly for their better corrosion resistance and mechanical properties among the stainless steel. The ferritic stainless steel is selected in areas where economy comes as the basic need of the product.

The particulate composites of stainless steel are believed to have better properties than the straight P/M stainless steel [62,66]. The particulate particles are very fine, hard second phase, dispersed in the metallic matrix, which tend to retain their strength at high temperatures. There are a wide variety of dispersed second phase particles that are available such as Al_2O_3 , TiO_2 , SiC , Y_2O_3 etc. In the present work, yttrium oxide (Y_2O_3) was selected as the dispersoid because of its high hardness and stability at high temperatures. The Y_2O_3 dispersoids act as pinning centers at the grain boundaries preventing grain boundary sliding and also prevents dislocation motion even at high temperatures. This improves the mechanical properties of the component. Moreover, the dispersoids have the same structure of Cr_2O_3 and hence act as initiation sites for the oxide formation [62].

The P/M route has been selected for the processing of these composites, as it is an attractive and flexible way for producing particulate composites. Mechanical mixing is the simplest and more flexible way for producing composites. Since only a small amount of sample was required, a mortar and pestle were used for mixing.

Solid state sintering was the method that was commonly reported as the sintering technique in all the previous research on P/M particulate stainless steel composites. In the

present work, a novel method for sintering prealloyed powders called supersolidus liquid phase sintering (SLPS) is been used. In this technique the prealloyed powders of stainless steel are sintered between the solidus and liquidus temperature, so that a liquid phase is formed within the particles thereby producing higher densification. Although work has been reported on SLPS of stainless powders [30], nothing has been reported on particulate composites by this sintering procedure. The strengthening effect of the particulate composites has been studied by various authors [62-69], but very less has been reported on the corrosion behavior of these composites.

In the current work, prealloyed powders of 316L and 434L were chosen and compacted at a pressure of 600Mpa. The green samples were sintered at two temperatures of 1250°C (solid state sintering) and 1400°C (supersolidus liquid phase sintering). Y_2O_3 was added to the stainless steel powders from 0 to 10 weight percent and is mixed mechanically to form a homogenous mixture. The powder mixture was compressed at 600MPa and then sintered at the two temperatures mentioned above. The initial characterization of the sample is done by density measurement and by measuring radial and axial shrinkage. The density measurements were carried out by measuring the initial and final dimensions of the sample. The radial and axial shrinkage gives the aspect ratio of the sample.

Unlike the wrought alloys the corrosion behavior of P/M stainless steels is not fully documented in literature. Hence the corrosion properties of the P/M stainless steels were carried out through polarization techniques. The potentiodynamic polarization and Tafel extrapolation were carried out in 0.1N sulfuric acid. The cyclic polarization was carried out in 3.56 weight percent NaCl solution. This reveals the pitting characteristics of the sample. The corrosion results of the particulate and the straight samples were compared. Further the comparison of the corrosion behavior of 316L and 434L samples under identical conditions was studied.

EXPERIMENTAL PROCEDURE

4.1 Raw Materials

4.1.1 Stainless Steel Powders

The stainless steel powders that were used in the present work were 316L austenitic grade and 434L ferritic grade. The gas atomized stainless steel powders were supplied by AMETEK Specialty Metal Products Division, Pennsylvania, USA. The chemical composition and the powder characteristics of the as received powders are provided below,

316L Powder

Chemical Composition, wt. %	C: 0.025	Ni: 12.97	Cr: 16.51
	Fe: BAL	Mo: 2.48	Si: 0.93
	Mn: 0.21	S: 0.008	P: <0.01
Apparent Density, g/cm ³	2.72		
Flow Rate, s/50g	29		
Sieve Analysis	ASTM Standard Mesh Size	percent	
	+100	3.1	
	+120	2.7	
	+140	5.0	
	+200	14.9	
	+270	23.9	
	+325	13.8	
	-325	36.6	

434L Powder

Chemical Composition, wt. %	C: 0.023	Ni: nil	Cr: 15.93
	Fe: BAL	Mo: 1.00	Si: 0.71
	Mn: 0.24	S: 0.013	P: 0.02
	O: 0.27		
Apparent Density, g/cm ³	2.60		

Sieve Analysis	ASTM Standard Mesh Size	percent
	+100	1.3
	+120	3.6
	+140	6.1
	+200	14.2
	+270	23.1
	+325	13.8
	-325	37.4

4.1.2 Yttria Powder

The yttria powders that were supplied by RE Acton, Rare Earth Products Ltd., Cheshire, UK. The powder was 99.9% pure and finer than the stainless steel powders.

4.2 Powder Characterization

The as received powders were characterized for their size distribution and morphology. For the characterization techniques only a small part of the sample was utilized and assumed as representative of the bulk sample.

4.2.1 Particle Size and Size Distribution

A Laser Scattering Analyzer (model: Economy, laser Klasse 1; supplier; Fritsch, Germany) was used for analyzing the particle size of the powders. Low angle Fraunhofer light scattering using monochromatic (laser) light and dispersed particles were used in this case. The particles were suspended in a suspension made using 1 to 3 g of powder dissolved in approximately 60 ml of distilled water with 10% sodium metaphosphate. The particles were passed through a laser beam in a circulating water stream. The light scattered after interactions with the particles were measured by detectors that are placed strategically. The size of the particle affects both the intensity and angular extent of scattering. With the coherent light the scattering angle varies inversely with the particle diameter. The scattering depends upon the refractive index of the particle in the suspending medium, the wavelength of light and particle size and shape. From the

particle size analysis the unimodal size distribution of yttria particles was obtained as shown in Figure 4.1. From the unimodal distribution graph shown in the Figure 4.1, it is clearly seen that the maximum particles are in a range of 20 μm size. The unimodal gaussian distribution graphs for 316L and 434L were obtained from the particle size analyzer. Figure 4.2 shows the particle size distribution for 316L which indicates that the maximum number of particles was in a size of 40 μm . Figure 4.3 shows the particle size distribution for 434L and it is seen that maximum particles were of the size 40 μm and this was considered as the mode value for the bulk sample.

4.2.2 Particle Shape

The particle size of the powders was obtained using a JEOL, JSM-840A, scanning electron microscope (SEM), in the secondary electron (SE) mode. The magnification of the SEM was far greater than the optical microscope. The figure 4.4 shows the SEM micrograph of yttria powder. From the figure it is seen that the size of the yttria powders is around 1 μm , but the particle size analysis gives about 20 μm . This can be explained as the yttria powder forms agglomerates when dispersed in the solution used in particle size analysis. In order to confirm this an yttria agglomerate was also captured using SEM and is shown in Figure 4.4. The SEM micrographs of 316L and 434L powders were shown in the Figure 4.5. In case of the stainless steel powders the agglomeration problem was not evident and the particle size coincided with the particle size analysis.

4.3 Premix Preparation

The composite was formed by mixing stainless steel powder with yttria in a mortar and pestle for 30 min. The powders were weighed first in a 0.001g accurate electronic balance (supplier: Mettler, AE 200, USA). The balance was calibrated using a series of weights. The required weight percent of yttria powder was weighed accurately with stainless steel powder and were then transferred into the mortar. The mixture was mixed in the mortar using the pestle for about 20 min in order to ensure proper mixing of the composite. To prevent segregation of the yttria particles care was taken not to shake the powders after mixing.

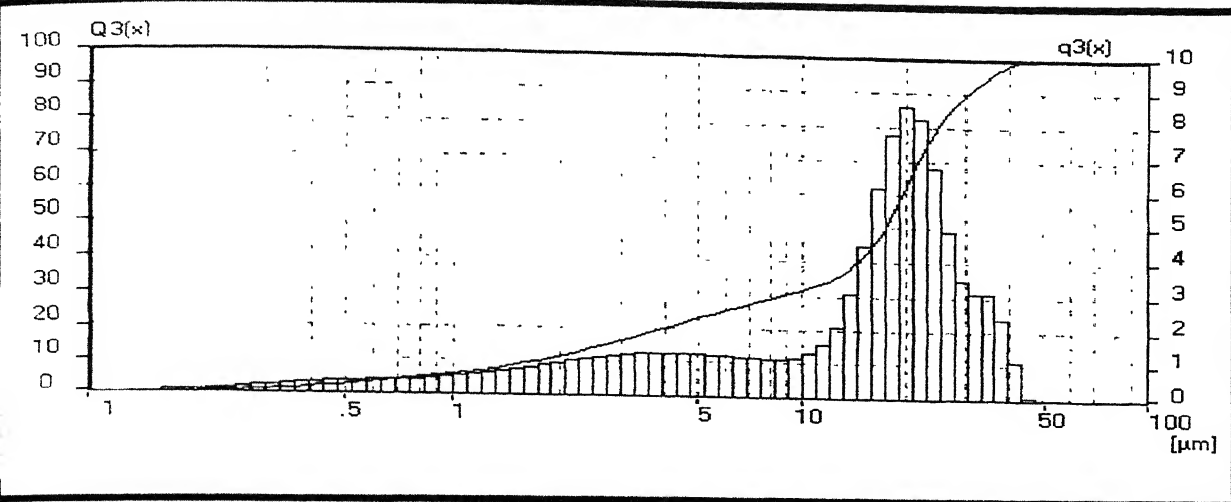


Figure 4.1. Particle size analysis of Y_2O_3 .

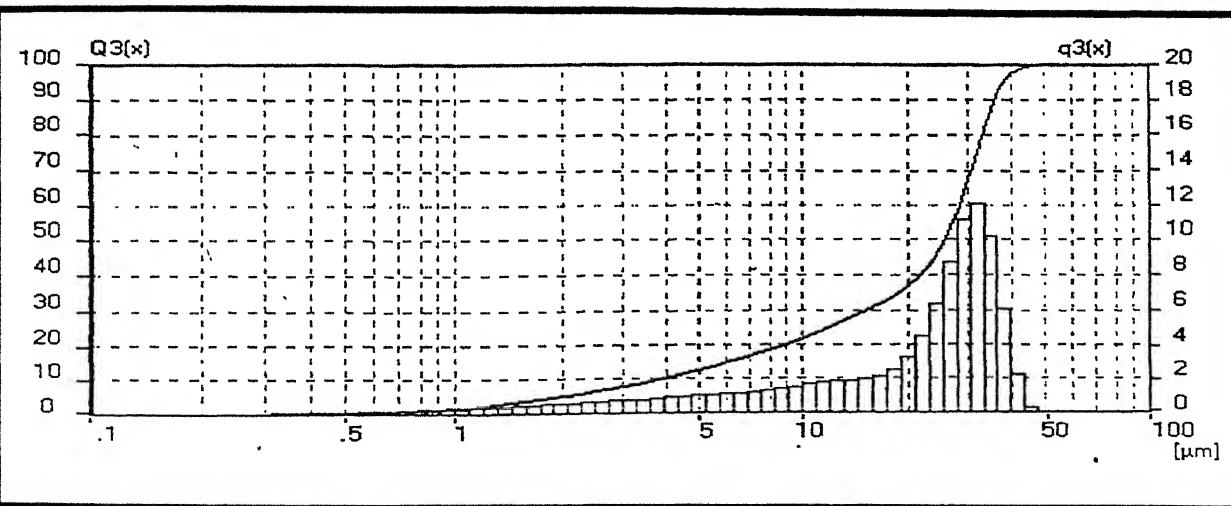


Figure 4.2. Particle size analysis of 316L.

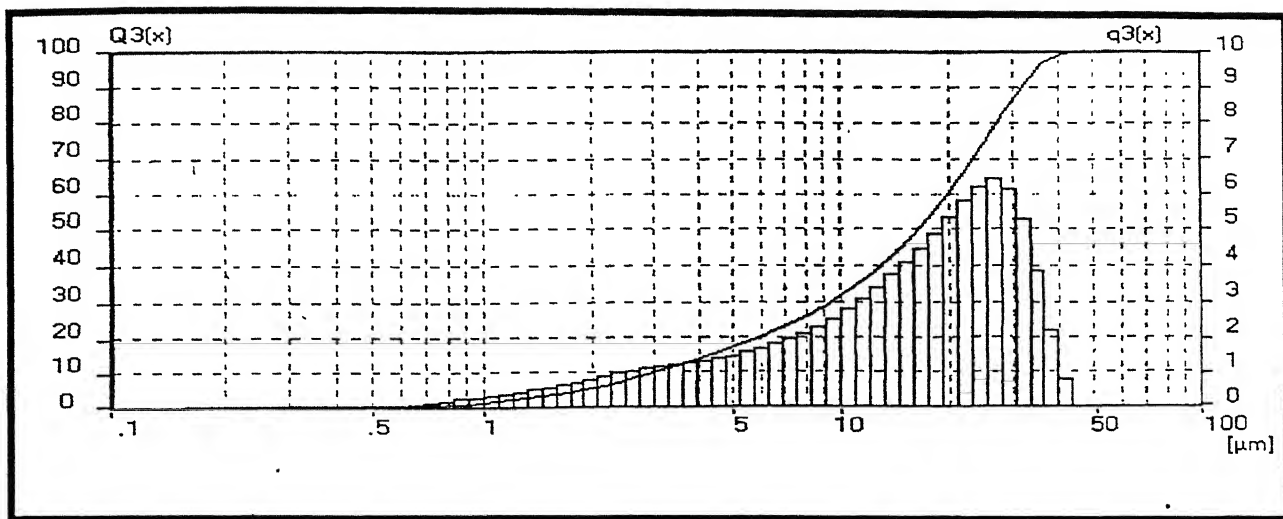
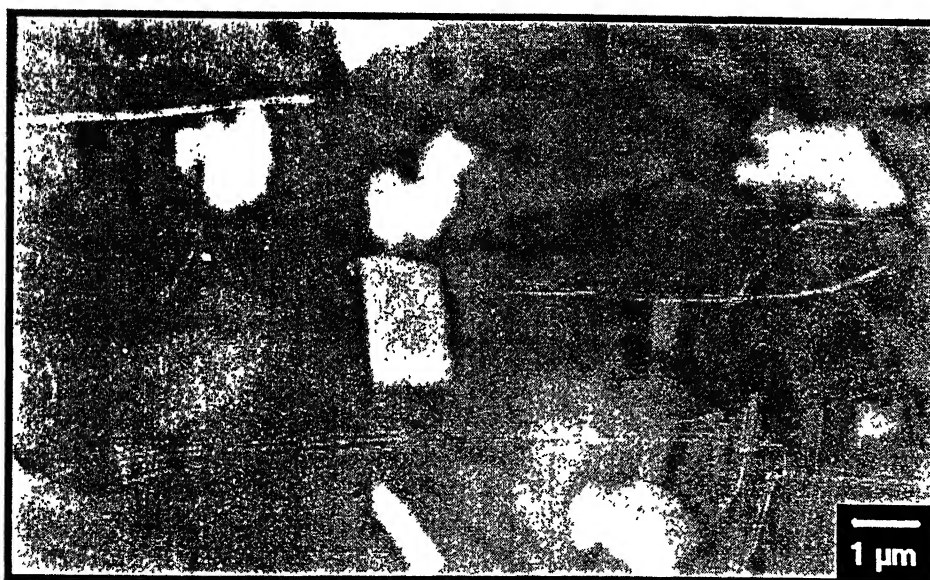


Figure 4.3. Particle size analysis of 434L.

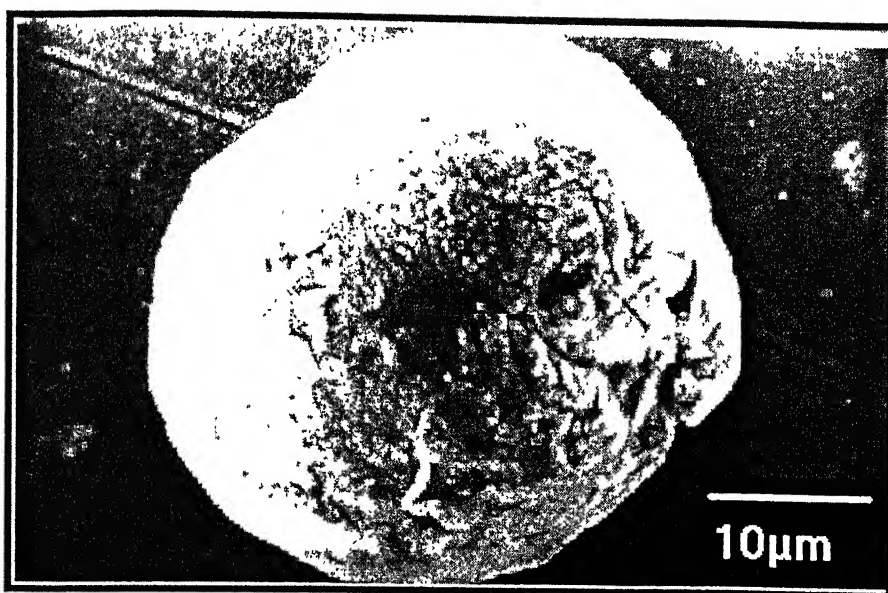


(a)

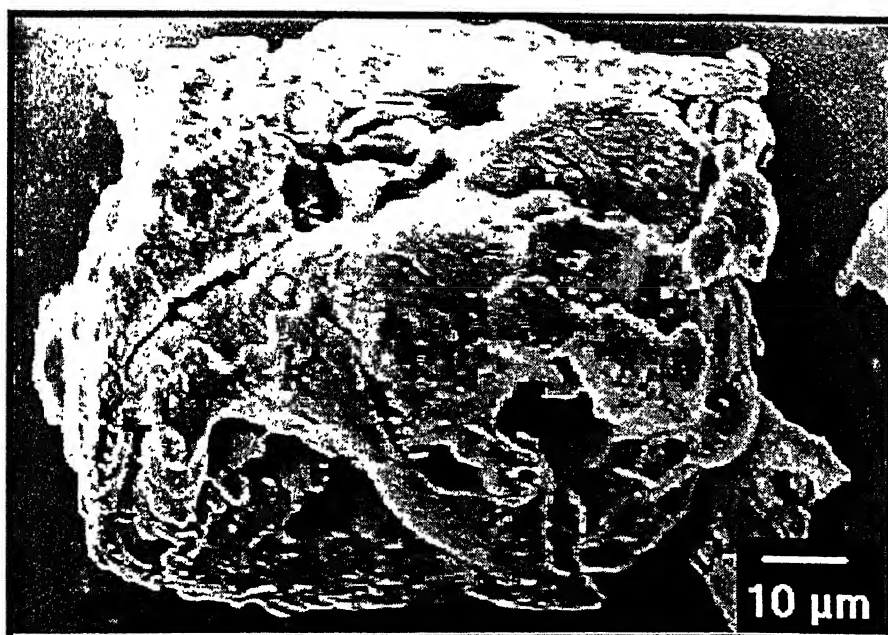


(b)

Figure 4.4. SEM Picture of (a) Y₂O₃ agglomerate (b) single particle.



(a)



(b)

Figure 4.5. SEM micrograph of (a) 316L powder and (b) 434L powder.

4.4 Compaction

A die of 12.7mm inner diameter was used to make the green compacts of approximately 3mm to 6mm in height. The pressure was applied uniaxially i.e. in one direction using a manually operated hydraulic press machine (Apex Construction Ltd., UK) of 20 T capacity. The pressure was applied from 150MPa to 600MPa for the pure 316L and 434L samples. The particulate composites were compacted only at 600MPa for five compositions of 0, 2.5, 5, 7.5 and 10 weight percent of yttria. The various pressures and the compositions at which the samples were compacted are provided in the Table 4.1. The dies were made up of high chromium high carbon steel and were cleaned with acetone during every compaction. Zinc-stearate was used as the lubricant during compaction, which facilitated compaction and subsequent removal of the compacted sample.

4.5 Sintering

Sintering of the green compacts was carried out in a laboratory type SiC-heated horizontal tubular furnace (rating 1.5 kVA). The schematic figure of the tubular furnace is shown in the Figure 4.6. The tube of the furnace was made up of doubly recrystallized alumina with an inner diameter of 38 mm and length of 980mm. The furnace possessed a heating zone of approximately 105 mm, with a capacity to attain 1500°C with an accuracy of $\pm 3^\circ\text{C}$. The atmosphere used for sintering was commercially pure hydrogen as it provides a reducing atmosphere for the samples and prevents the samples from oxidation. The dew point of the hydrogen gas is maintained by using a drier along the flow. The green samples were placed inside the furnace by means of an inconel boat. The inconel boat was used because it possesses a higher melting point and would therefore not contaminate the sample. It also prevents sticking of the sample after sintering. Both the ends of the furnace were sealed using a SILASTC (RTV 700) adhesive/sealant to prevent leakage of hydrogen during sintering. The heating rate was maintained at $5^\circ\text{C}/\text{min}$ for all the samples. The sintering temperatures used during the present work

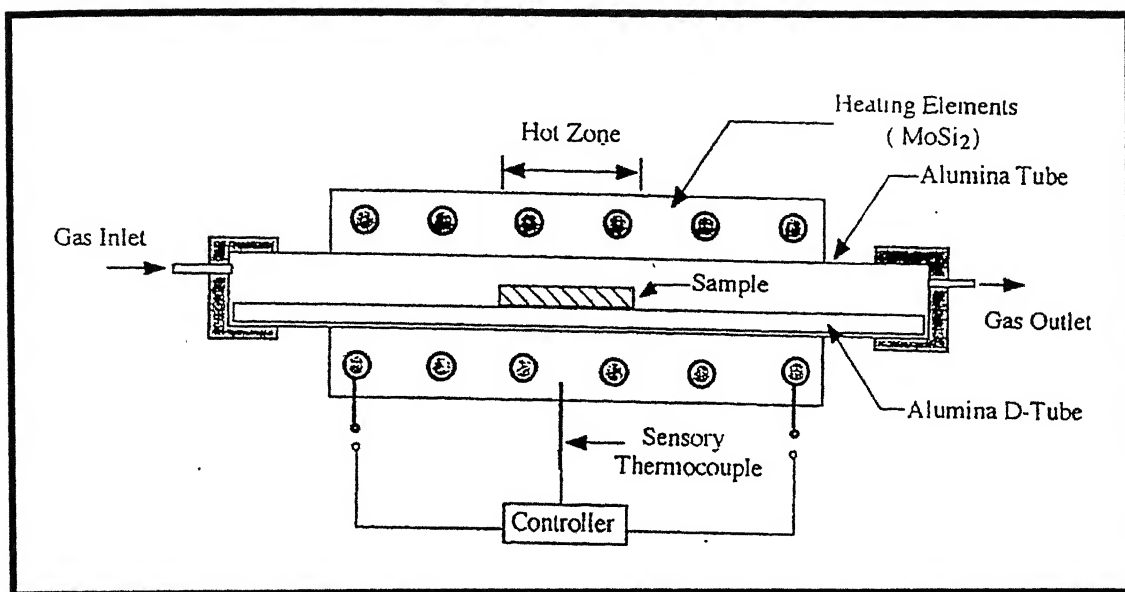


Figure 4.6. Schematic diagram of a horizontal tubular furnace.

Table 4.1. The experimental variants used during compaction.

Type of stainless steel	% Y ₂ O ₃	Compaction Pressure (MPa)
316L	0	200, 300, 400, 600
316L	2.5	600
316L	5	600
316L	7.5	600
316L	10	600
434L	0	200, 300, 400, 600
434L	2.5	600
434L	5	600
434L	7.5	600
434L	10	600

were 1250°C and 1400°C. The samples were heated to the required temperature after holding at 1000°C for one hour. This was to take care that the heating zone was uniform for all the samples used. An automatic temperature controller was used to monitor the temperature and the holding time was one hour for all the samples at the final sintering temperature. The samples were allowed to cool in the furnace itself and the hydrogen atmosphere was maintained upto 150°C during cooling. This is to ensure that there is no oxidation of the sample during cooling.

4.6 Densification Behavior

4.6.1 Density and Densification Parameter

The green densities and sintered densities were calculated from the mass and physical dimension measurements of the sample. The densification parameter was also utilized to determine the amount of densification that occurred after sintering. The densification parameter shows the normalized behavior of the sample density with respect to the parameters. The densification parameter (ψ) was expressed as follows,

$$\psi = (SD - GD)/(TD - GD) \quad (4.1)$$

where SD = Sintered Density, GD = Green Density and TD = Theoretical Density

4.6.2 Linear and Radial Shrinkage

The linear dimensions of the sample were measured using vernier callipers and screw gauge of accuracy ± 0.01 mm. The average of three measurements of each dimension is reported. The formulas used for calculations are as follows,

$$\text{Linear Shrinkage, } \delta h = \{1 - (h_s/h_g)\} \times 100\% \quad (4.2)$$

$$\text{Radial Shrinkage, } \delta r = \{1 - (r_s/r_g)\} \times 100\% \quad (4.3)$$

Where h_s , r_s = height and radius of sintered compact and h_g , r_g = height and radius of green compact.

4.7 Microstructural Studies

4.7.1 Optical Microscopy

As the sample dimensions were sufficient for manipulation during metallographic procedures, no mounting was performed. The compacts were polished on the Lunn Major Unit of Struers, Denmark make 220, 320, 500 and 1000 grit silicon carbide emery papers followed by wheel polishing with suspended 0.03 μ m size alumina in distilled water. The etchants that were used for etching are specified below,

Ferritic Etchant

1) CuCl ₂	-	5g
HCl	-	100 ml
Ethyl alcohol	-	100 ml
Distilled water	-	100 ml
2) HCl	-	10 ml
HNO ₃	-	3 ml
Ethyl alcohol	-	100 ml

Austenitic Etchant

3) CuSO ₄ .5H ₂ O	-	12 g
HCl (conc)	-	60 ml
Distilled Water	-	60 ml

Etching was carried on leather for 20-30 seconds to attain proper etching.

4.7.2 Scanning Electron Microscopy

The microstructures of selected samples were observed using a JOEL, JSM-840A, scanning electron microscope (SEM). The operating voltage was 10-15 kV and the probe current ranged from 1×10^{-10} to 5×10^{-8} in secondary electron imaging mode. Some of the samples were captured by back-scattered mode, which reveals the porosity more effectively. The samples were deeply etched to reveal the fine details of the sample.

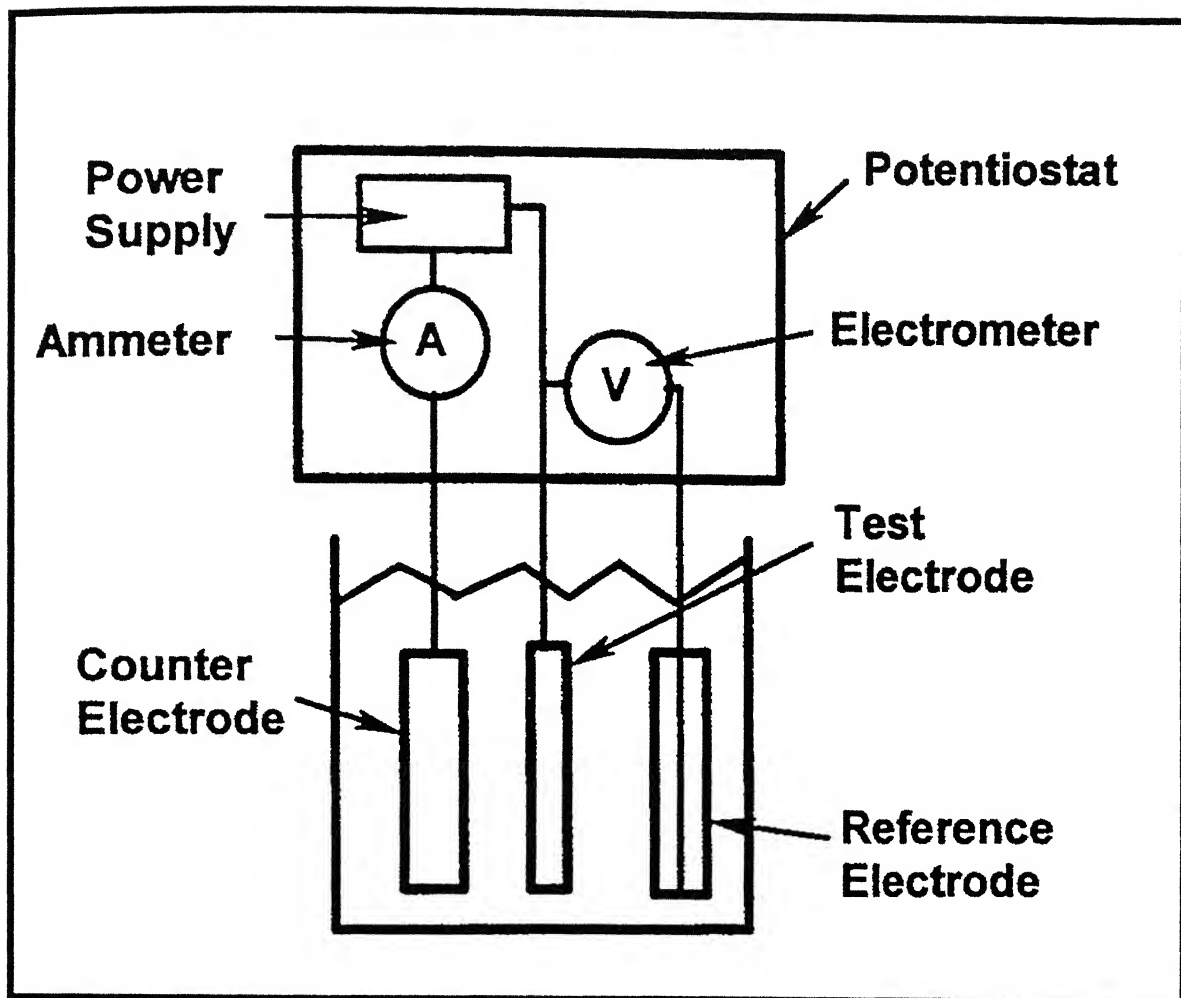


Figure 4.7. Schematic diagram showing the connections in the potentiostat.

4.8 Electrochemical Studies

The electrochemical studies on the sample were carried out in a potentiostat, Model 263A supplied by EG&G Instruments Inc., Princeton Applied Research, USA. It possessed a very high range of sensitivity from 100 μA to 1A. The electrolyte used for testing was 0.1N sulfuric acid, prepared in the laboratory from laboratory grade chemicals. The basic diagram of a potentiostat connected with the working cell is shown in Figure 4.7. The potentiostat is basically made up of an ammeter, an electrometer and a power supply. There were four probes from the potentiostat plugin, which are connected to the working electrode, Reference electrode and counter electrode. The fourth probe was grounded. The working cells for the potentiostat are of two types, the flat cell or the round cell. The flat cell can be used for quick readings and can only be used when the surface of the sample is flat. The round cell can be used for any type of sample and usually the samples are mounted before using in the round cell to avoid contact of the other portions. The schematic representations of the flat cell and the round cell are shown in Figure 4.8. The 430 standard sample, supplied by EG&G was used as the standard for ferritic samples. 316L wrought sample was used as the standard for the austenitic samples. In the flat cell, the reference electrode was Ag/AgCl in saturated KCl and the counter electrode was platinum. The potential of the reference electrode was 197mV with respect to standard hydrogen electrode (SHE). The working electrode was placed in the flange provided for so as to expose only 1cm^2 of the sample area. The round cell uses standard calomel electrode (SCE) as the reference electrode and graphite was used as the counter electrode. The potential of the reference SCE was 242mV with respect to standard hydrogen electrode (SHE). The samples that were used in this cell were usually mounted to expose only a specific surface area of the sample to the corrosive medium.

4.8.1. Polarization Experiments

The experiments were carried out in a solution of 0.1 N sulfuric acid prepared in distilled water. All the samples were tested in the flat cell except the 430 standard sample supplied by EG&G. The 430L sample was cylindrical with an area of 3.5cm^2 . The samples were tested with platinum as the counter electrode and Ag/AgCl as the reference electrode.

4.8.2. Tafel Extrapolation

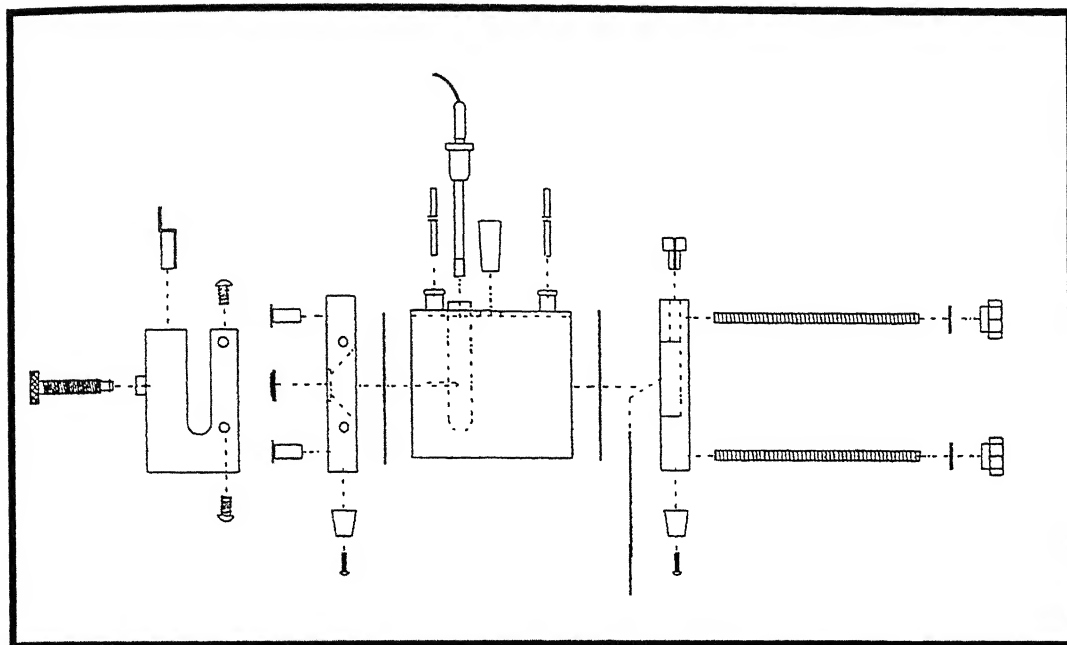
The Tafel extrapolation experiment was carried on from ± 250 mV from OCP. The scan rate used during the experiment was 0.166 mV/s as per ASTM standard []. The cathodic portion was extrapolated to meet the E_{corr} value and from the point of intersection the anodic slope was extrapolated. This method was used as the alloy was showing active-passive behavior and generally one-decade slope was not there in anodic curve. The slopes β_a and β_c were calculated from the curves obtained. The value of i_{corr} was calculated and the corrosion rate was determined.

4.8.3. Potentiodynamic Polarization

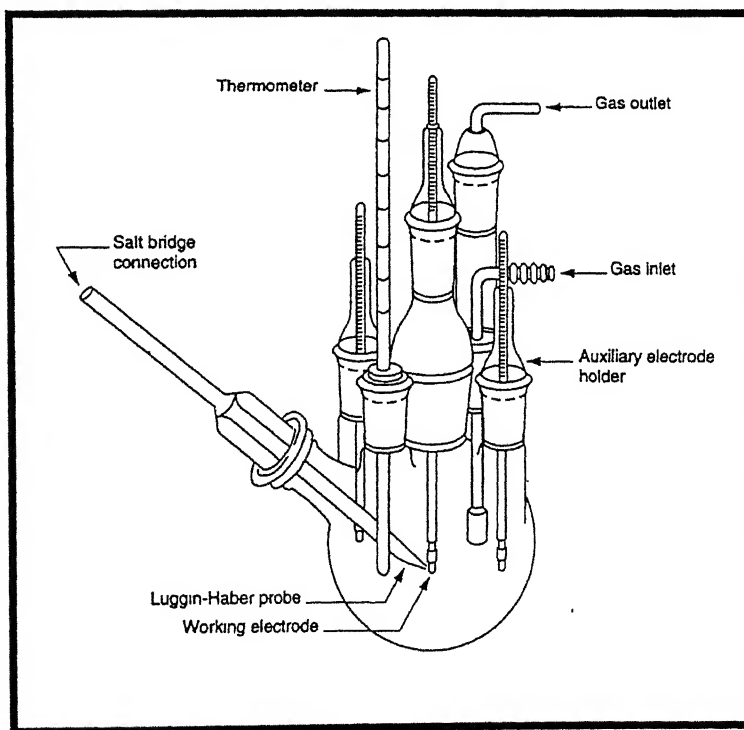
The potentiodynamic polarization was carried out in the potential range of -700 mV to $+1600$ mV for all the samples. The experiments were started immediately after immersion of the alloy in the electrolyte. This prevented the formation of a surface film before the experiment was started. The potentiodynamic polarization experiments were carried out at a scan rate of 1 mV/s.

4.8.4. Cyclic Polarization

The cyclic polarization tests were conducted in order to determine the localized corrosion behavior of the sample. The scan was reversed once the potential reached the pitting potential. The scan rate of 1 mV/s was used for all the tests. The value of repassivation potential was noted for further observation.



(a)



(b)

Figure 4.8. Schematic Representation of (a) Flat Cell and (b) Round Cell.

Chapter 5

RESULTS AND DISCUSSIONS

5.1. Sintering

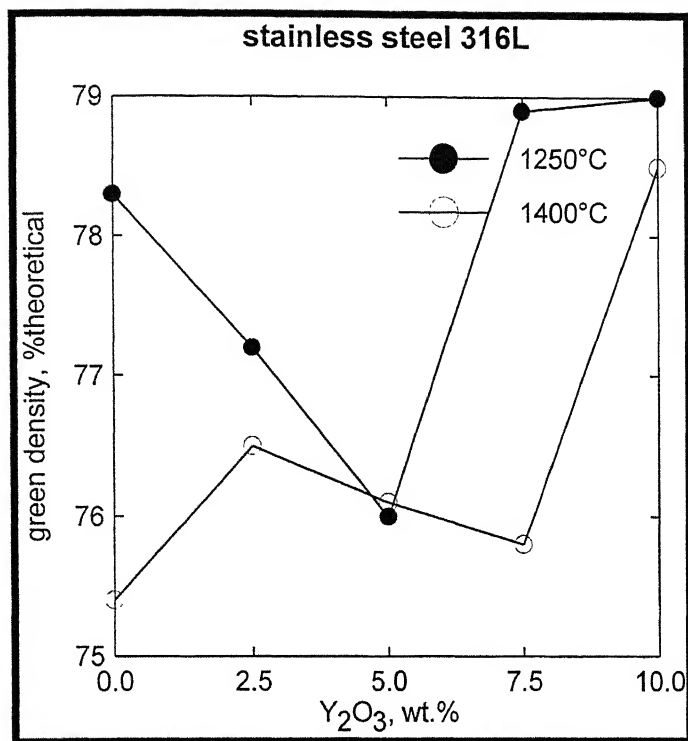
5.1.1. Results

5.1.1.1. Densification Behavior

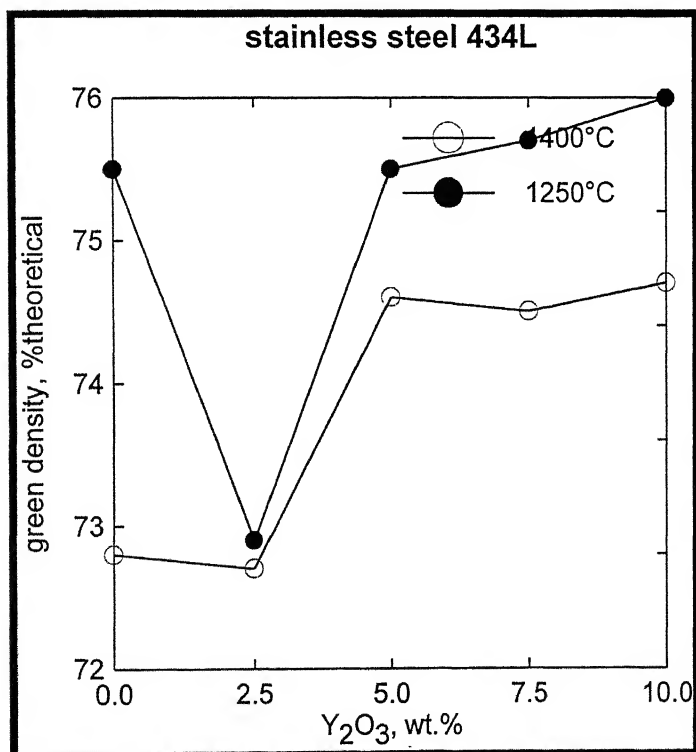
Density and Densification Behavior

The densification behaviors of the stainless steel P/M samples were described using the sintered density, densification parameter and change in shrinkage values. The experimental data before and after sintering for all the samples used in the present study are given in Appendix I and II. For both 316L and 434L samples, the green density increased with increasing pressure. The green densities increased from 65% to as high as 78% theoretical as the compaction pressure increased from 200 MPa to 600 MPa. The sintered densities of the samples follow the same trend. The sintered densities increased from 68% to as high as 80% with increase in pressure from 200 MPa to 600 MPa. The effects of temperature on the sintered densities of the samples are also given in Appendix I and II. The variation of green density with compaction pressure is shown in Figure 5.1. The variation of sintered density with compaction pressure for 434L and 316L sintered at 1250°C and 1400°C were plotted in Figure 5.2. The samples sintered at 1400°C were having higher sintered densities than the samples sintered at 1250°C for both 316L and 434L P/M stainless steel samples.

Densification parameter is also very important to understand the behavior of sample because it gives a relative measure of the densification of compacts with density being normalized with respect to green density [13]. The variation of densification parameter with compaction pressure and temperature are given in Appendix I and II. The variations were plotted in Figure 5.3. It was interesting to note that the densification parameter of the samples sintered at 1400°C were having better densification than samples sintered at 1250°C. Moreover, the samples compacted at 600MPa were having consistently higher densification parameter than other samples. This elucidates that the



(a)



(b)

Figure. 5.1. Variation of green density with compaction pressure.

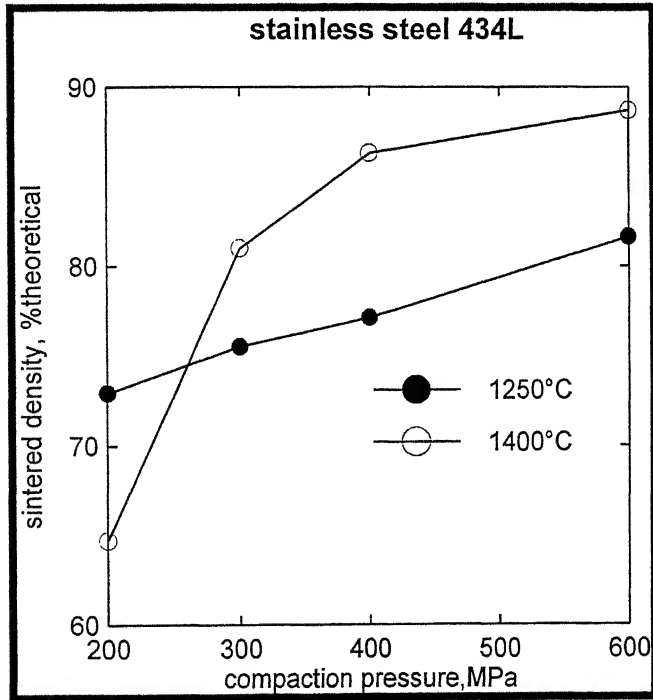
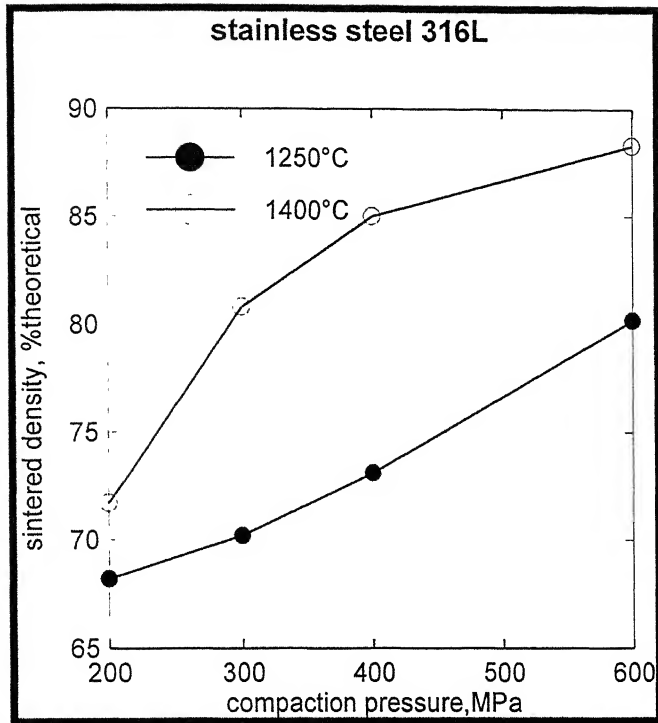


Figure 5.2. Variation of sintered density with compaction pressure and sintering temperature.

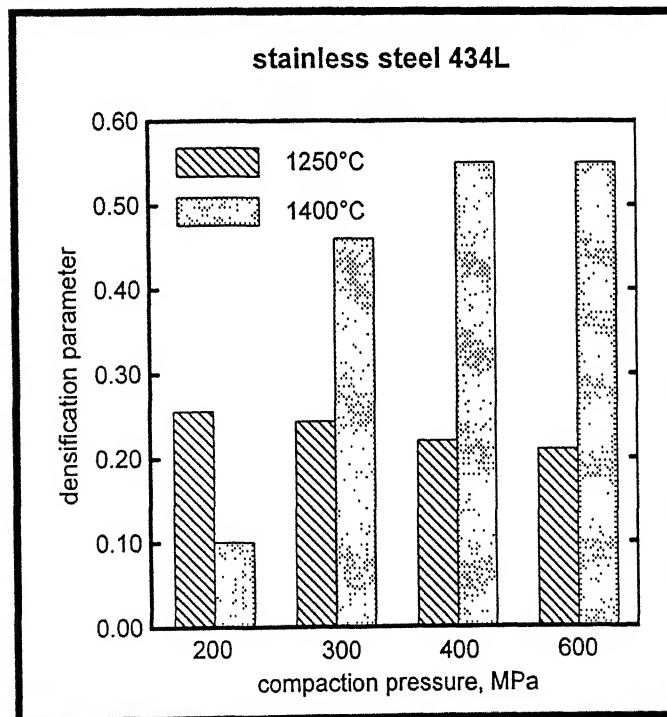
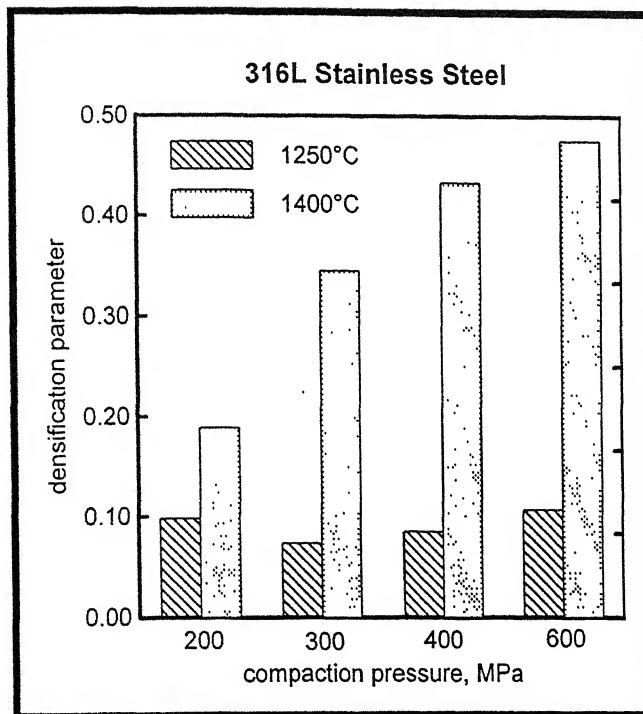


Figure 5.3. Variation of densification parameter with compaction pressure and sintering temperature.

sample compacted at 600MPa pressure and sintered at 1400°C was having better densification behavior than the other samples for both 316L and 434L.

Appendix III and IV give the experimental data before and after sintering for 316L and 434L particulate composites sintered at two temperatures 1250°C and 1400°C respectively. All the particulate samples were compacted at 600 MPa pressure. It was interesting to note that the green density of the samples decreased with addition of Y_2O_3 . The variation of sintered density with addition of Y_2O_3 and temperature is shown in Figure 5.4. The sintered density of 316L composites decreased with increasing weight percentage of Y_2O_3 at both the temperatures. The sintered density of 434L composites exhibited a similar behavior at 1400°C sintering. But when sintered at 1250°C, the 434L sample with 5-weight % Y_2O_3 , exhibited an anomalous behavior. The sintered density of the sample increased as high as 83% theoretical.

The variations of densification parameters for 316L and 434L samples were given in Figure 5.5. The densification parameter values are tabulated in Appendix III and IV. The densification parameter decreases with increase in Y_2O_3 composition for 316L particulate composites. The same behavior was observed in 434L composites sintered at 1400°C. But for the 434L composites sintered at 1250°C, the variation shows a typical behavior. For the sample containing 10-weight % Y_2O_3 , the densification parameter increases.

Axial and Radial Shrinkage

Appendix V presents the axial and radial shrinkage of the samples after sintering. Figure 5.6 represents the axial and radial shrinkage plots for the 316L stainless steel samples sintered at 1250°C and 1400°C. Both radial and axial shrinkages increase when the temperature is increased from 1250°C to 1400°C. There were no clear explanations for the variation of pressure on the radial and axial shrinkage. Figure 5.7 represents the axial and radial shrinkage for 434L stainless steel samples sintered at two temperatures. There was an increase in shrinkage with temperature, but the variation of pressure does not show a clear behavior. Figure 5.8 and 5.9 show the variation of radial and axial shrinkage with addition of Y_2O_3 in 316L and 434L composite samples sintered at 1250°C and 1400°C. In the samples sintered at 1250°C, the addition of Y_2O_3 increased the radial and axial shrinkage, while in the samples sintered at 1400°C, the addition of Y_2O_3

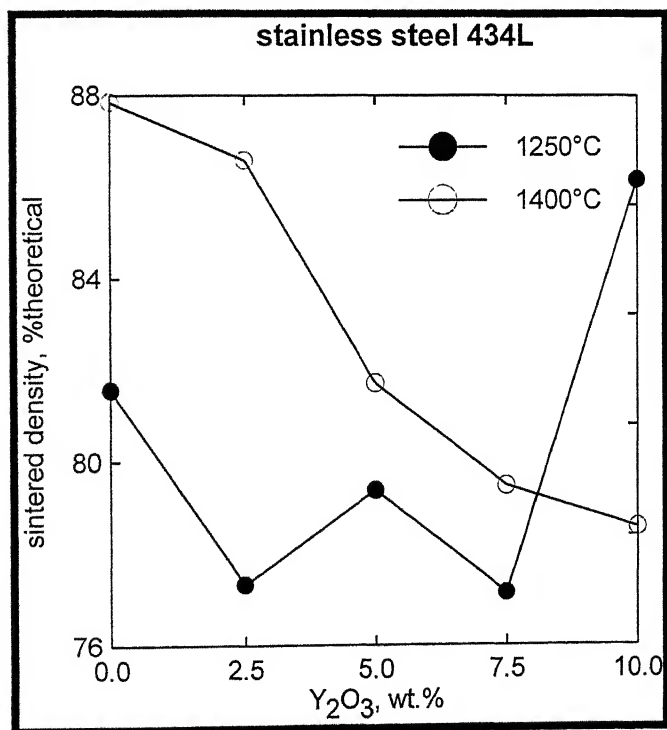
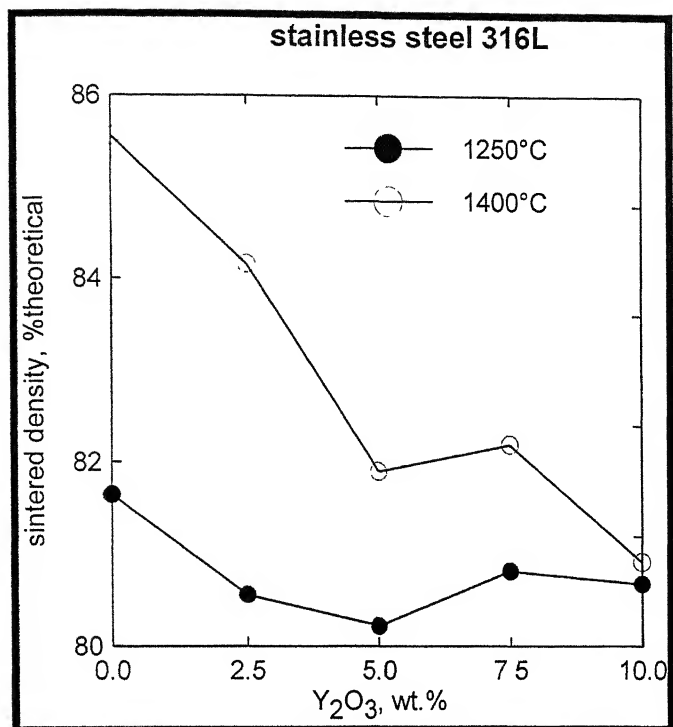


Figure 5.4. Variation of sintered density with addition of Y_2O_3 and temperature.

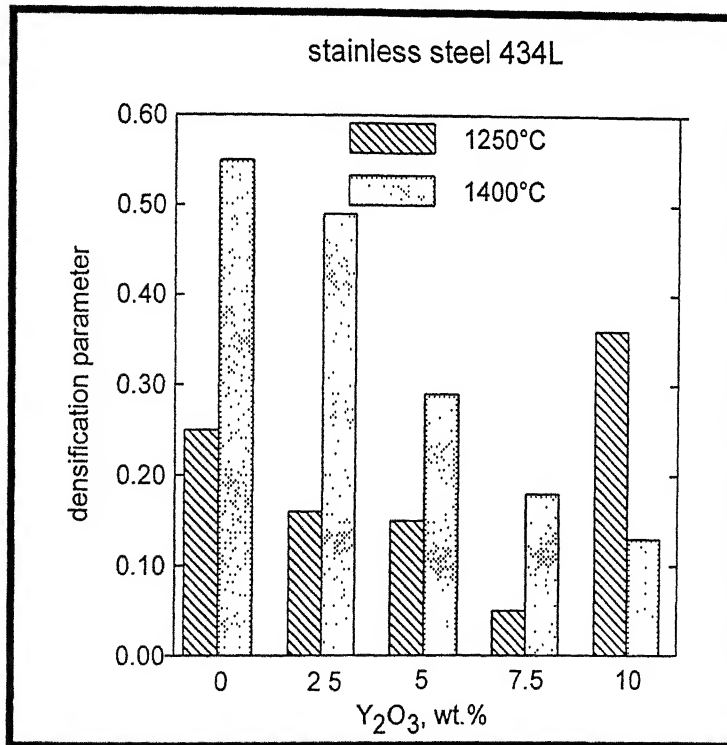
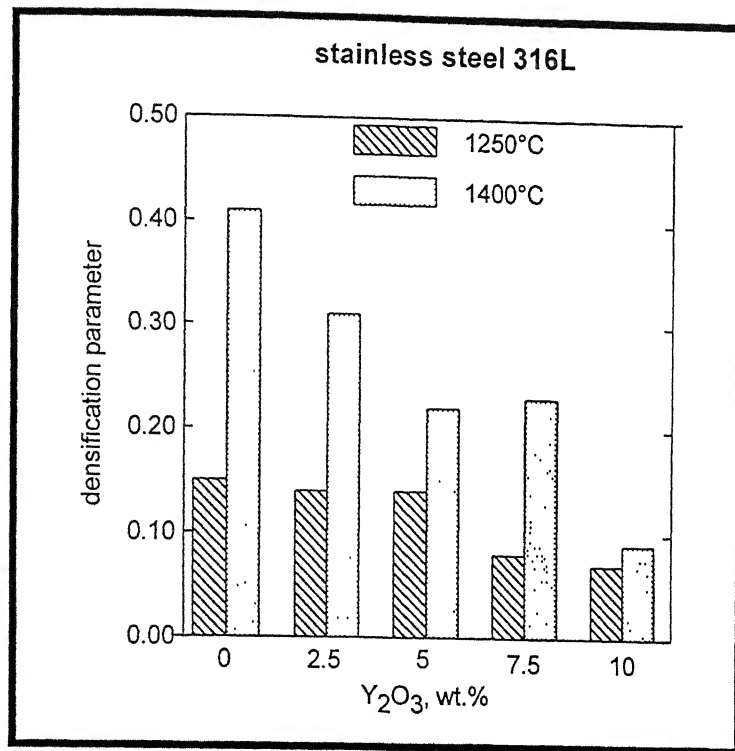


Figure 5.5. Variation of densification parameter with addition of Y_2O_3 and temperature.

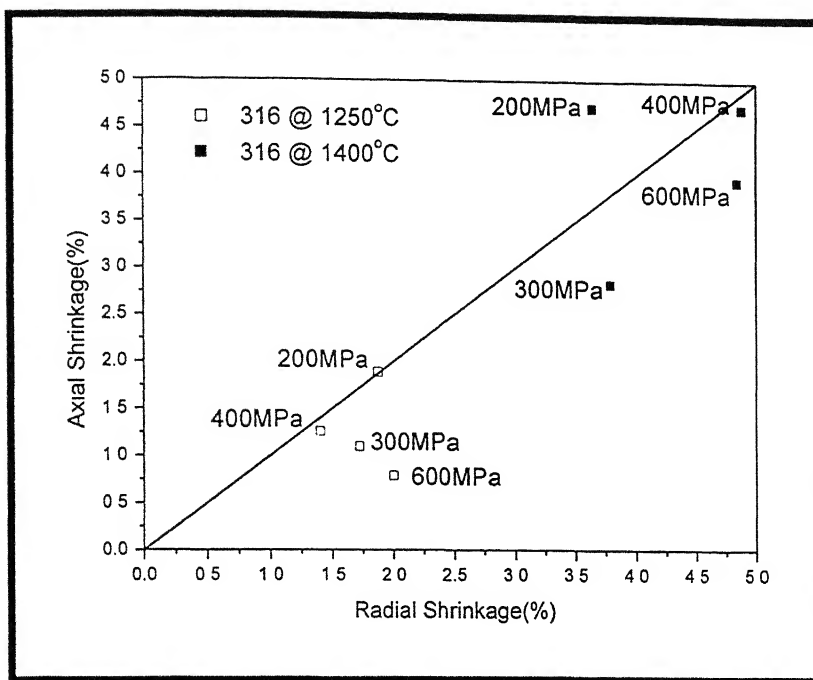


Figure 5.6. Radial vs axial shrinkage with variation in pressure and temperature for 316L stainless steel samples.

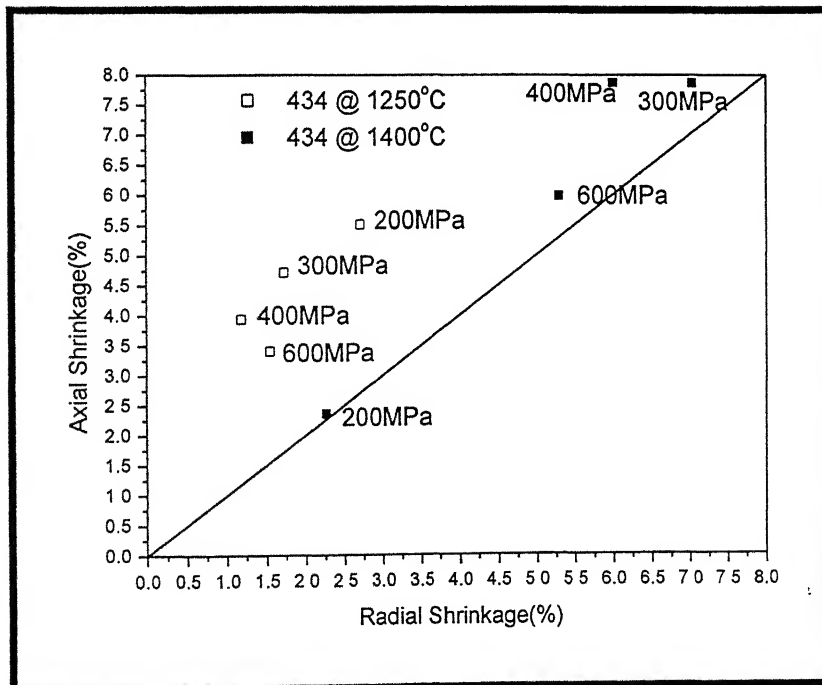


Figure 5.7. Radial vs axial shrinkage with variation in pressure and temperature for 434L samples.

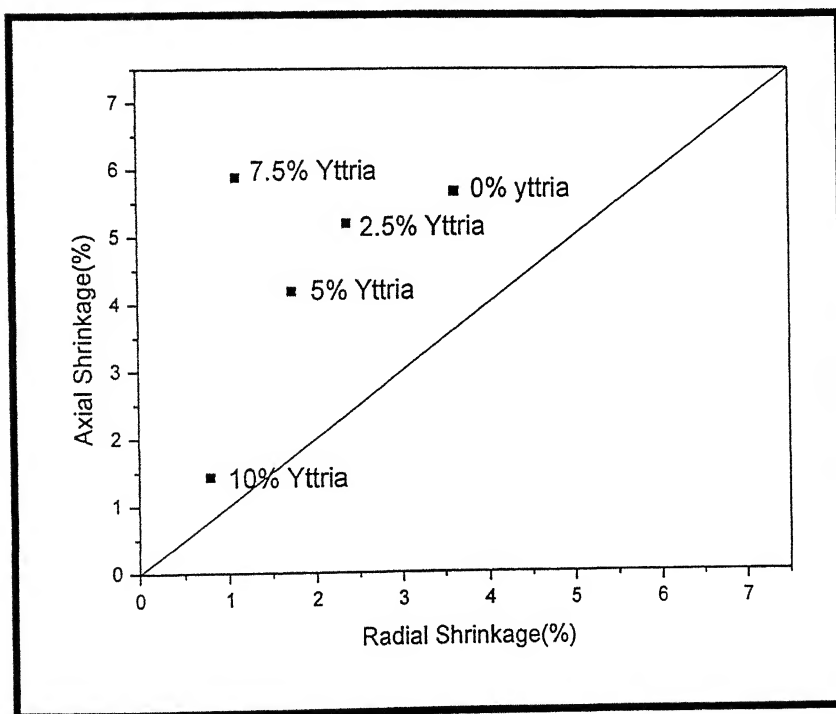
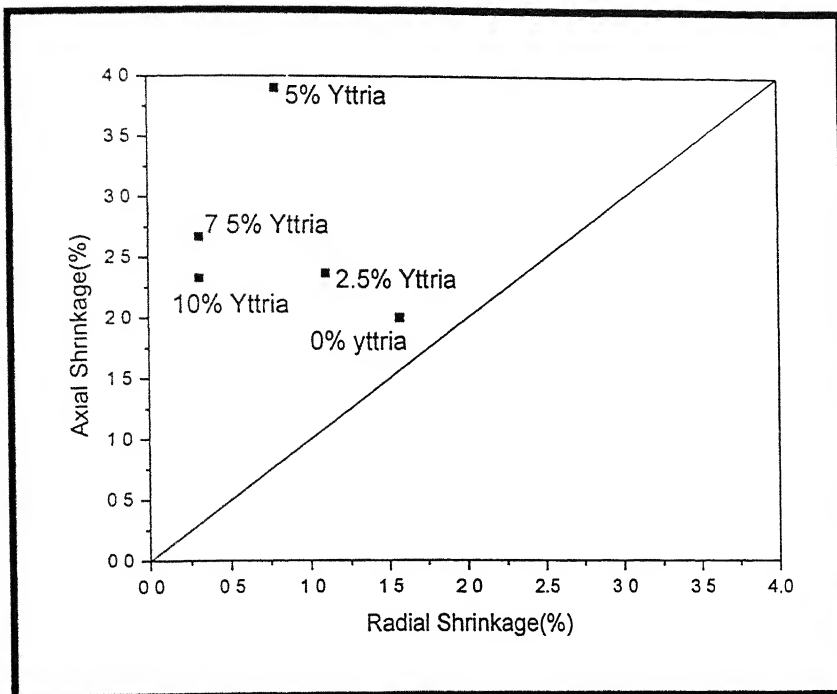


Figure 5.8. Radial vs axial shrinkage with variation in Y_2O_3 content and temperature of 316L composite samples.

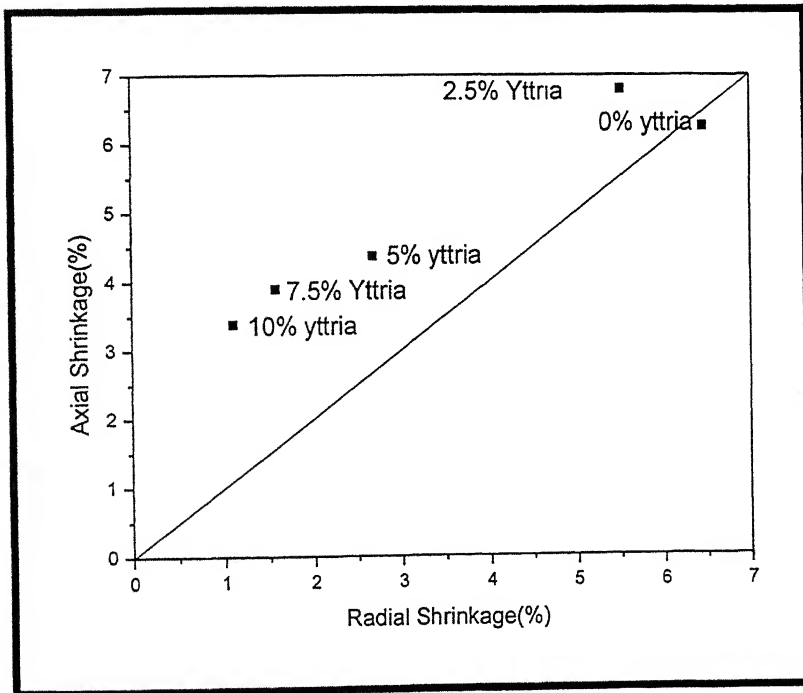
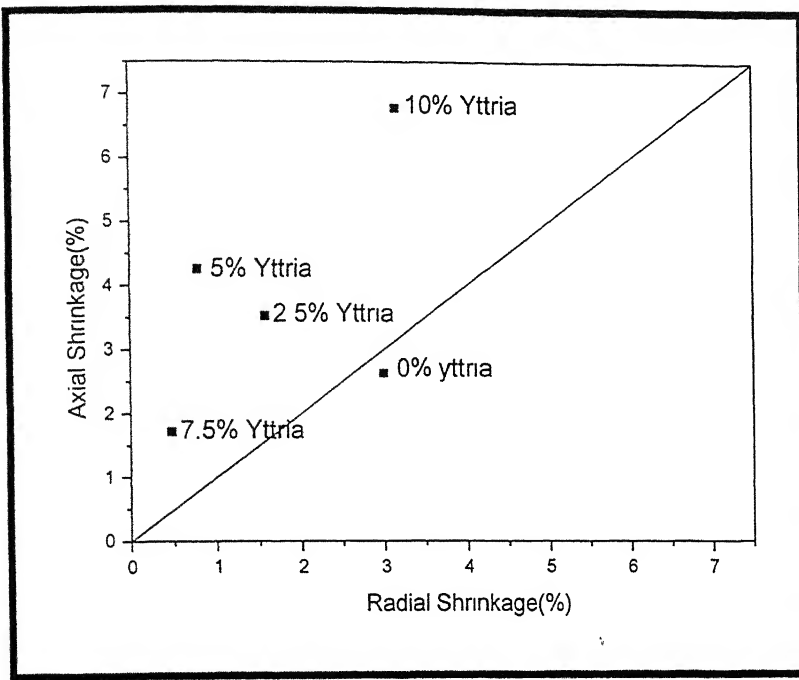


Figure 5.9. Radial vs axial shrinkage with variation in Y_2O_3 content and temperature for 434L composite samples.

decreased the axial and radial shrinkage. There were no marked differences on the variation of radial and axial shrinkage with change in Y_2O_3 content.

Weight Loss

The weight loss measurements of the 316L austenitic and 434L ferritic samples are shown in Appendix I and II. Figure 5.10 represent the weight loss data for the samples sintered at 1250°C and 1400°C. The weight loss for sintering at 1400°C was higher when compared to the 1250°C for 434L samples. In the case of 316L samples the weight loss data were reversed. Samples sintered 1250°C were showing higher weight loss than the samples sintered at 1400°C. As the compaction pressure increases the weight loss increased for 1250°C sintering. But for supersolidus liquid phase sintering no proper trend was noticed. In the case of the composites of both 316L and 434L, the variation of weight loss with respect to Y_2O_3 content was represented in figure 5.11. The weight loss was higher for the composites sintered at 1250°C than for the composites sintered at 1400°C. From the data it was noticed that increase in the addition of Y_2O_3 decreases the weight loss in the sample. The weight loss measurements for the composite are tabulated in Appendix III and IV.

5.1.1.2. Microstructural Results

Optical Micrographs

The optical micrographs of 316L stainless steels and composites sintered at 1250°C and 1400°C are shown from Figures 5.12 to 5.15. The micrographs capture the microstructural evolution trajectory of the samples as a function of sintering temperature and effect of Y_2O_3 . Figure 5.12 shows the microstructure of 316L samples sintered at 1250°C and 1400°C. The microstructures reveals that the sample sintered at 1250°C has lower grain growth as compared to the sample sintered at 1400°C. Moreover, the porosities are more rounded in case of supersolidus liquid phase sintering (1400°C). Figure 5.13 reveals the same features at a higher magnification. Figure 5.14 reveals the microstructure of 316L with 10-weight % Y_2O_3 samples sintered at 1250°C and 1400°C. From the microstructure it was noticed that the sample sintered at 1400°C has lower pores than the samples sintered at 1250°C. Moreover, the grain growth was much higher at

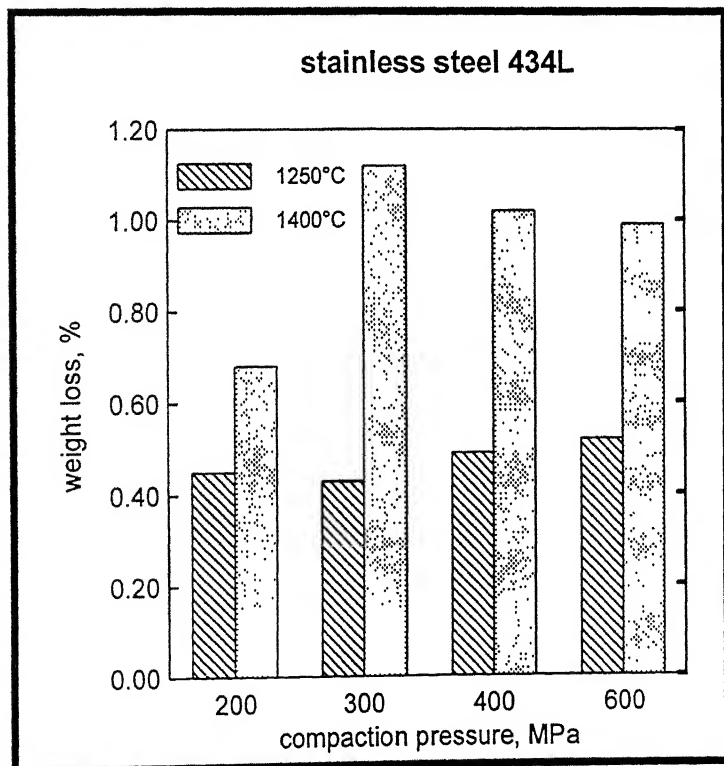
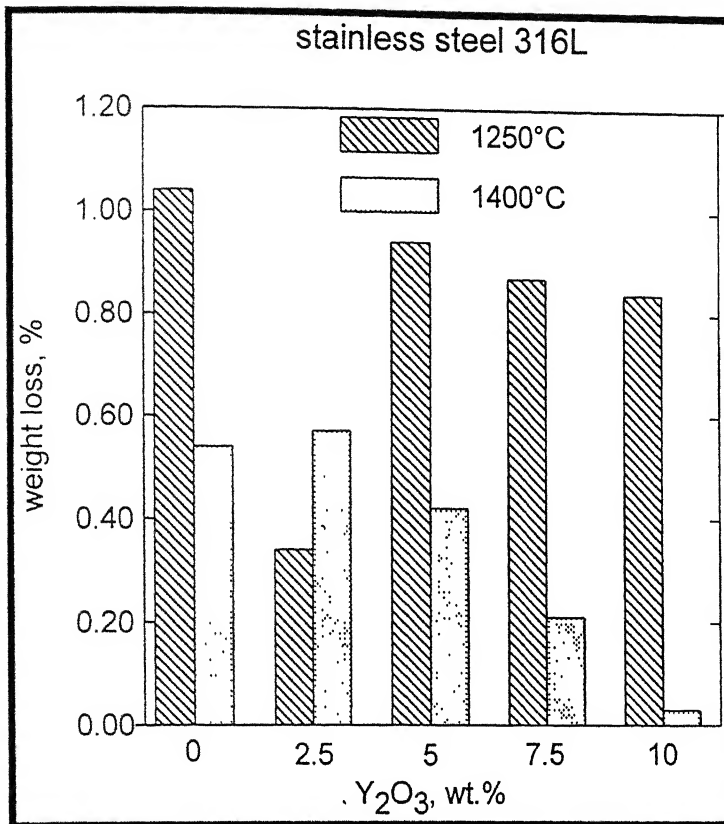


Figure 5.10. Variation Weight loss with compaction pressure and sintering temperature for 316L and 434L stainless steels.

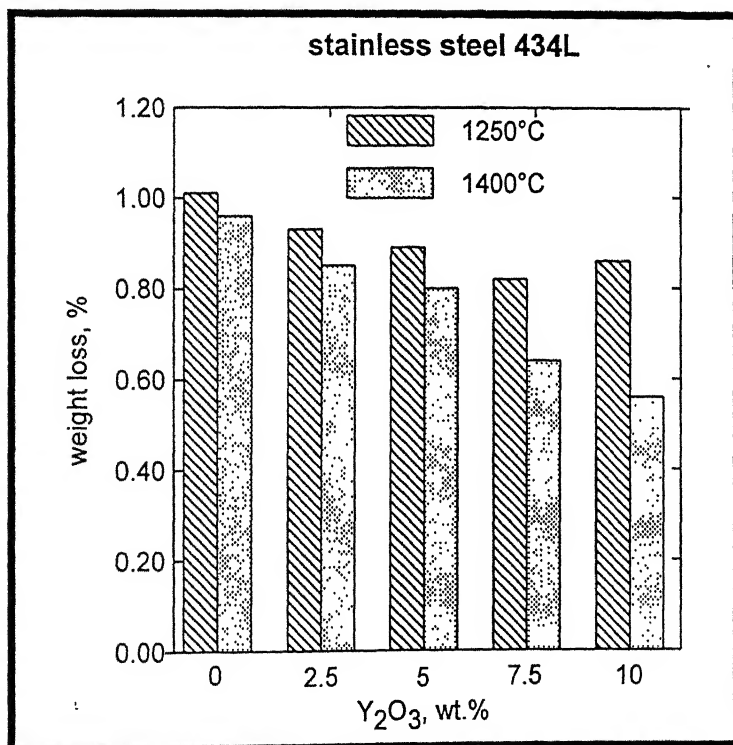
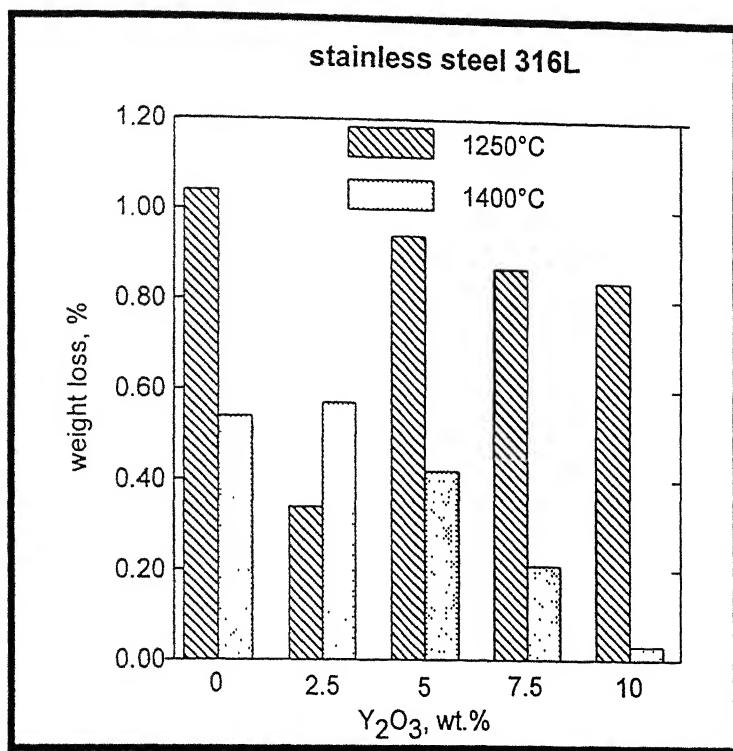
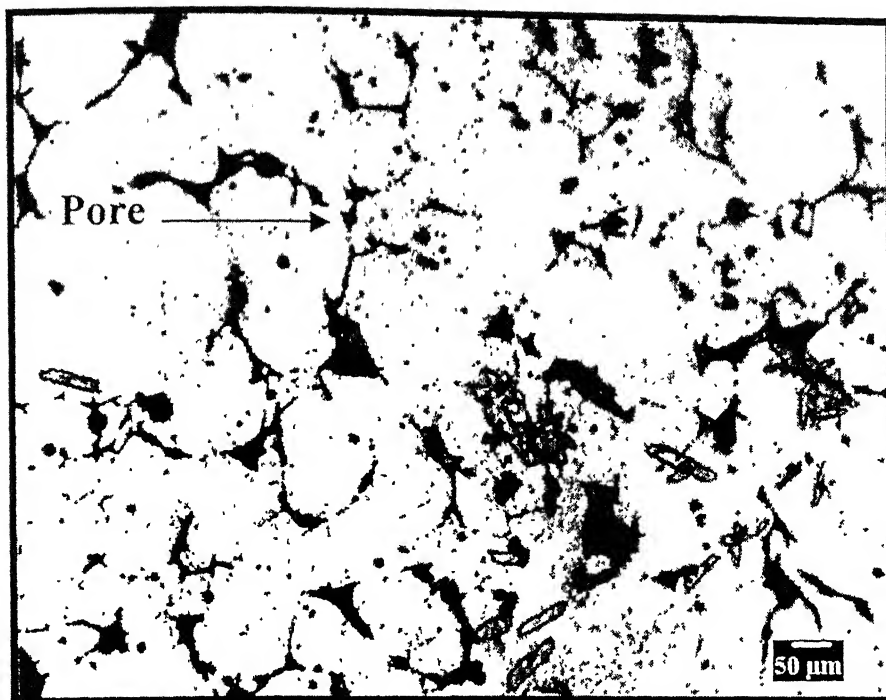
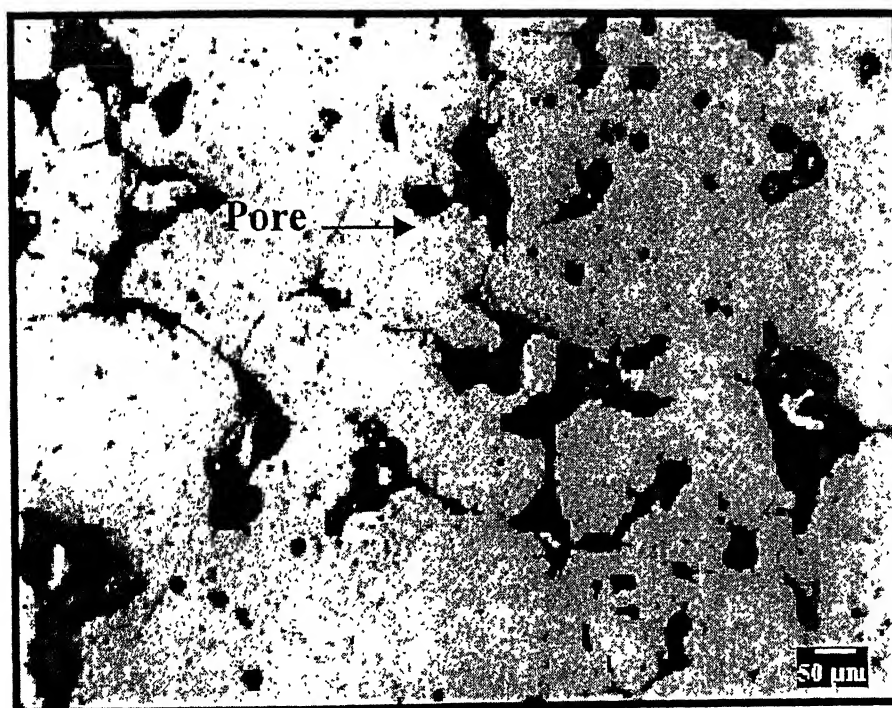


Figure 5.11. Variation of weight loss with temperature and Y_2O_3 content for 316L and 434L stainless steel composites.

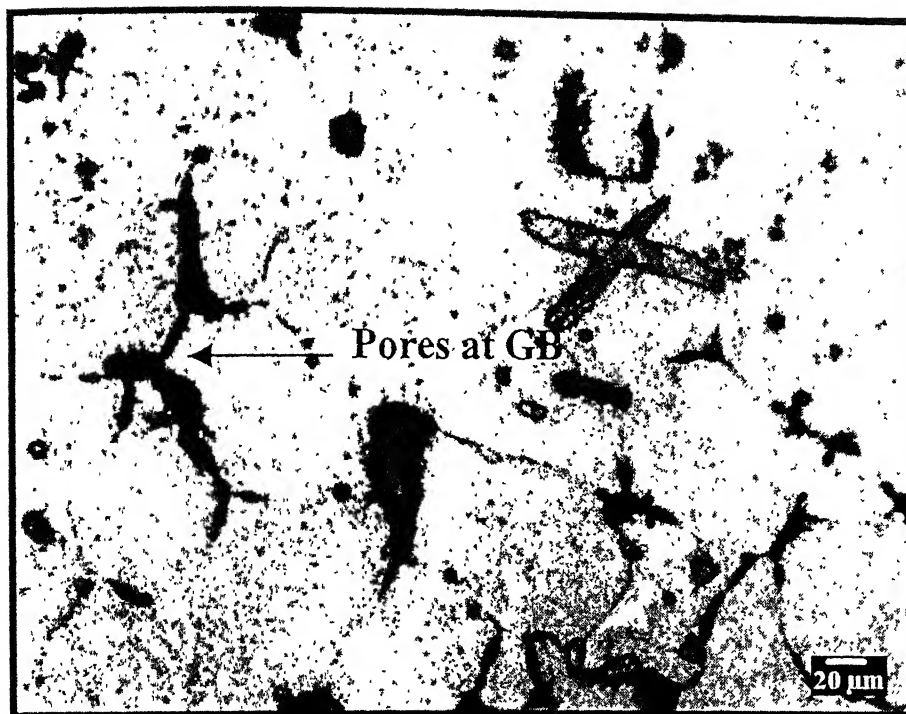


(a)

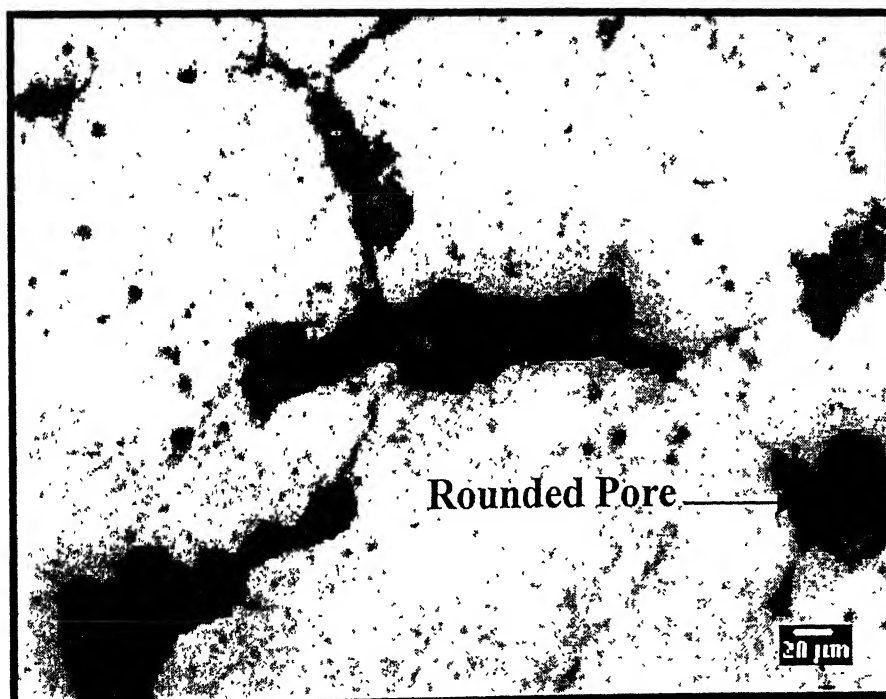


(b)

Figure 5.12. Optical micrograph of 316L P/M stainless steels sintered at (a) 1250°C and (b) 1400°C at 200X magnification. The samples were compacted at 600MPa.

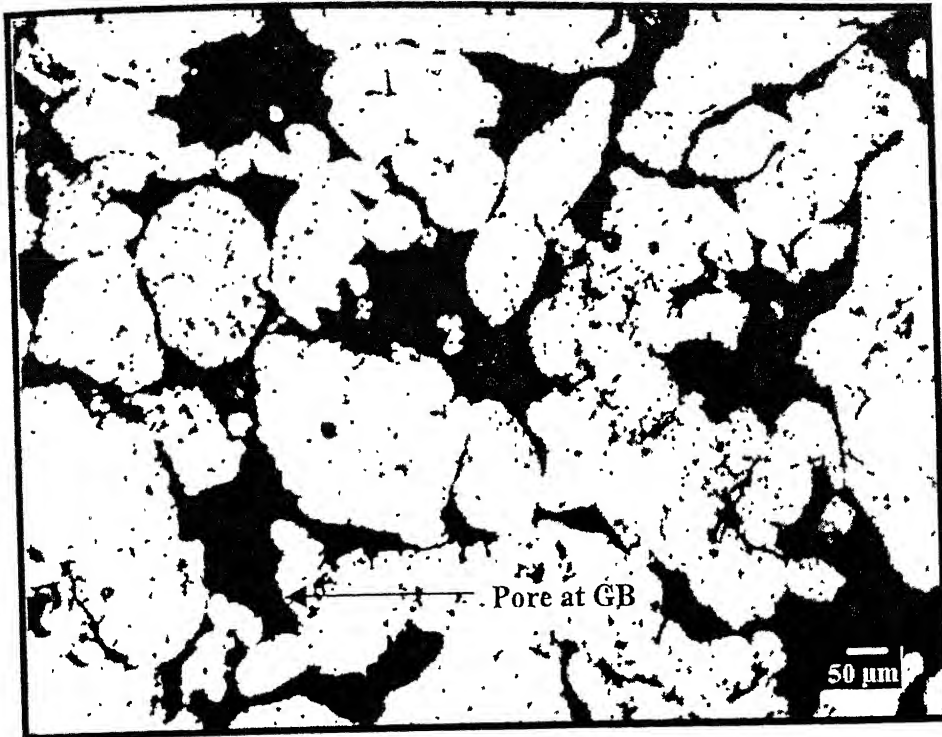


(a)

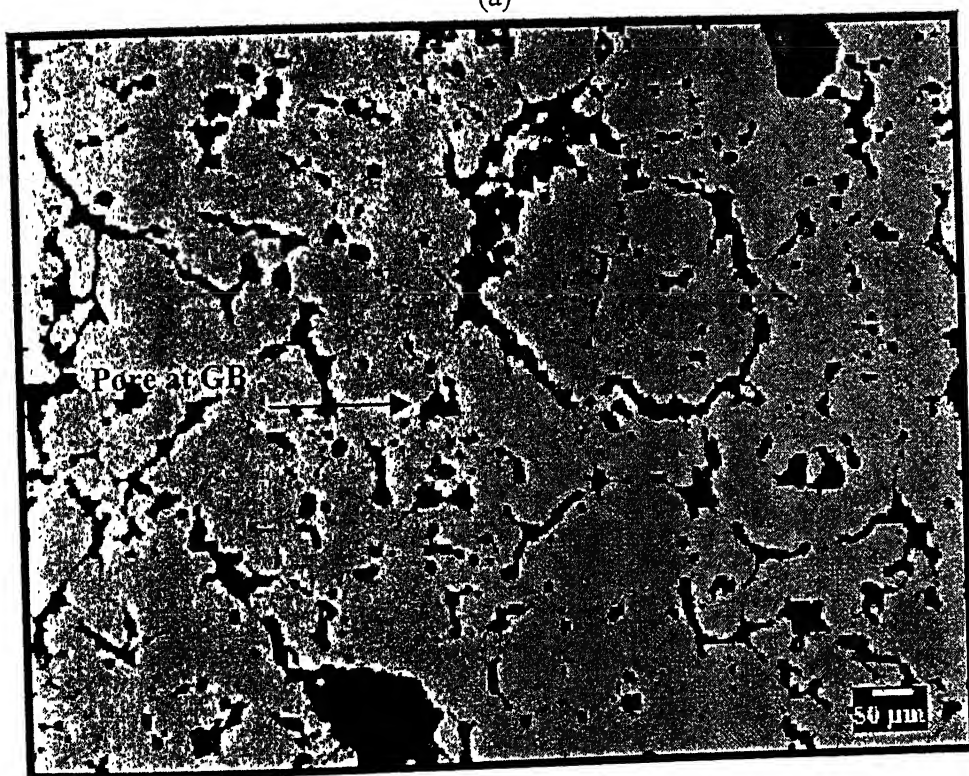


(b)

Figure 5.13. Optical micrograph of 316L P/M stainless steels sintered at (a) 1250°C and (b) 1400°C at 500X magnification. The samples were compacted at 600MPa.



(a)



(b)

Figure 5.14. Optical micrograph of 316L+10-weight % Y_2O_3 P/M composite sintered at (a) 1250°C and (b) 1400°C. The samples were compacted at 600MPa pressure.

1400°C and the pores were rounded when compared to the sample sintered at 1250°C. Figure 5.15 reveals the same features at an higher magnification.

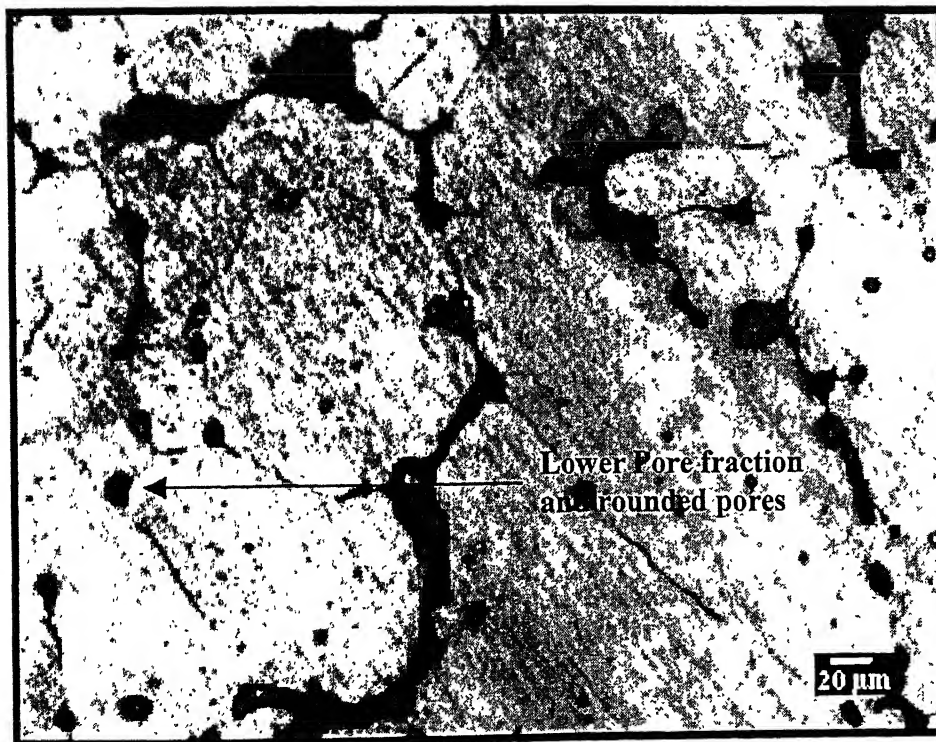
The microstructural evolution of 434L stainless steels sintered at 1250°C and 1400°C are shown in Figures 5.16 and 5.17. Figure 5.16 reveals the microstructure of 434L stainless steel samples sintered at 1250°C and 1400°C. From the micrographs it was noticed that the samples sintered at 1400°C had lower porosity and the pores were rounded. The samples sintered at 1250°C had higher porosity and the pores were irregular. The features also revealed inter-granular pores in the samples sintered at 1400°C. But in the 1250°C sample, the pores were concentrated at the grain boundaries. Figure 5.17 reveals the microstructure of 434L+10% Y_2O_3 stainless steel composites sintered at 1250°C and 1400°C. It was noticed that the porosity in 434L composite sintered at 1250°C was less when compared to the porosity in 434L composite sintered at 1400°C. Moreover, there were intergranular pores in the composite sintered at 1400°C. This was not observed in the case of the composite sintered at 1250°C.

SEM Micrographs

SEM micrographs of sintered samples are shown in Figures 5.18 to 5.23. The SEM micrographs were taken for specific samples. The stainless steel samples that were pure and the stainless steel composite with 10-weight % Y_2O_3 were concentrated. Main emphasis was given to change in the microstructure with sintering temperature and rare earth addition. Sintering temperature of 1250°C corresponds to solid state sintering and temperature of 1400°C corresponds to supersolidus liquid phase sintering. Figure 5.18 reveals the microstructure of 316L stainless steel + 10% Y_2O_3 composite sintered at 1250°C, with (a) corresponding to secondary electron mode (SE) and (b) corresponding to back scattered electron mode (BSE). BSE mode reveals the pores on the surface of the sample in an efficient manner. Figure 5.18 (a) shows the arrangement of pores at the grain boundaries. The Y_2O_3 particles and agglomerates were seen at the grain boundaries along with the pores. Figure 5.17 (b) shows the arrangement of pores at the grain boundaries. The pores were irregular and elongated at the grain boundaries. Figure 5.18 shows the microstructure of 316L + 10% Y_2O_3 sintered at 1400°C in SE and BSE modes.

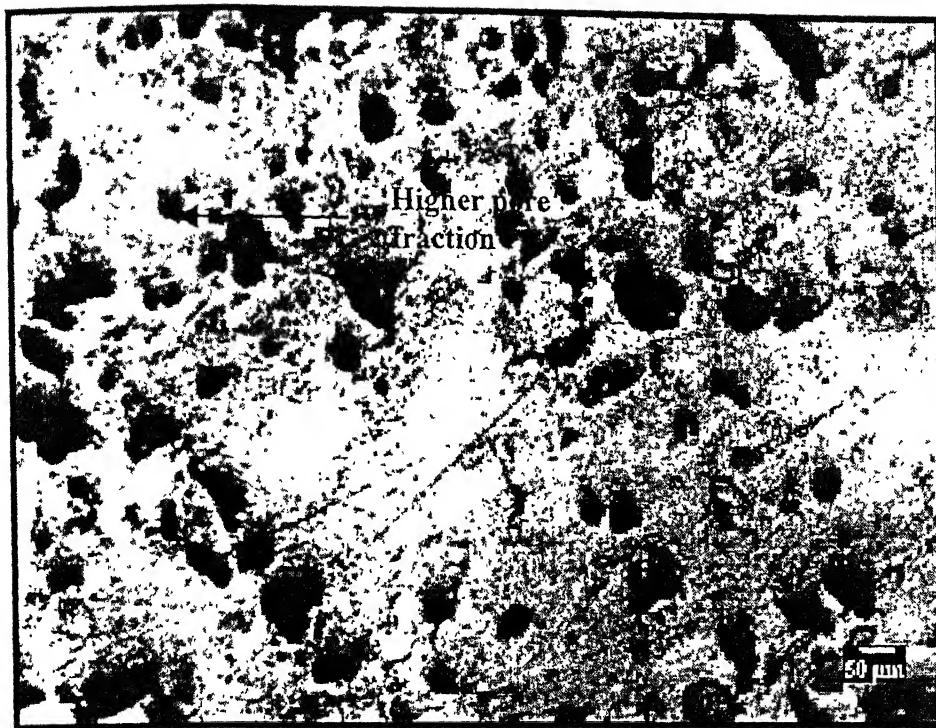


(a)

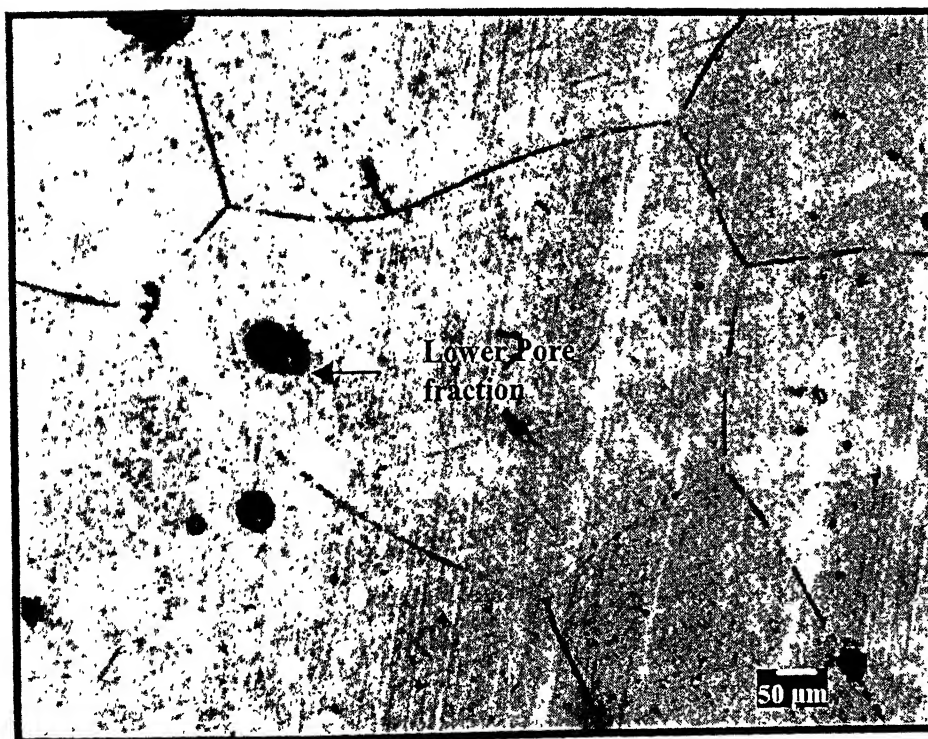


(b)

Figure 5.15. Optical micrograph of 316L+10-weight % Y_2O_3 P/M composite sintered at (a) 1250°C and (b) 1400°C. The samples were compacted at 600MPa pressure.



(a)

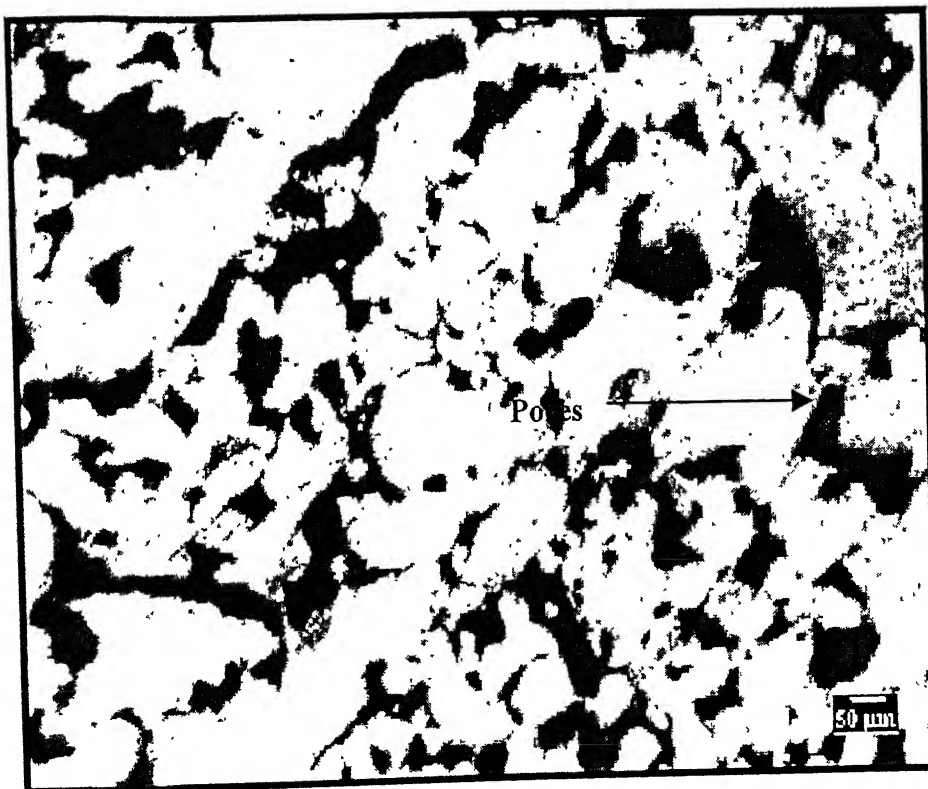


(b)

Figure 5.16. Optical micrographs of 434L stainless steels sintered at (a) 1250°C and (b) 1400°C. The samples were compacted at 600 MPa pressure.



(a)

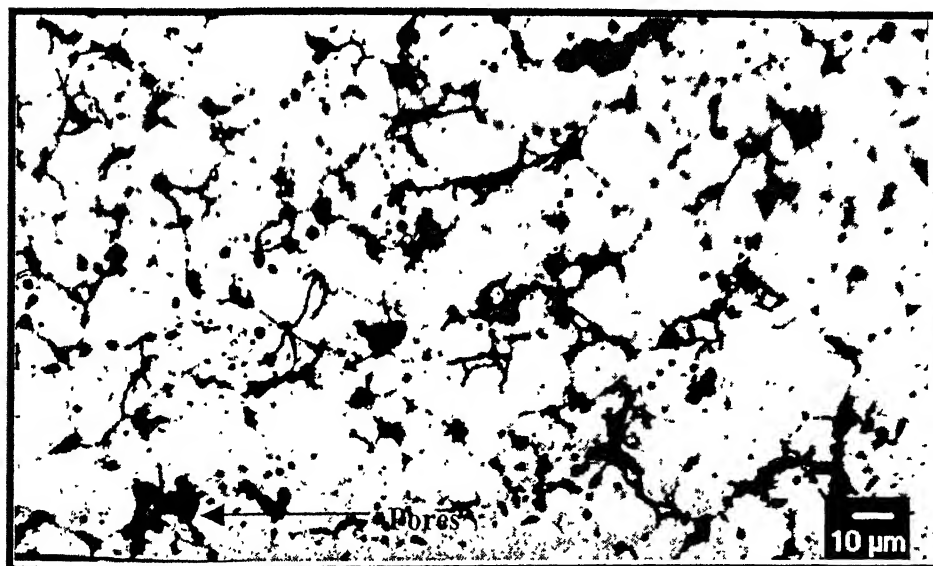


(b)

Figure 5.17. Optical micrograph of 316L+10% Y_2O_3 sintered at (a) 1250°C and (b) 1400°C.



(a)

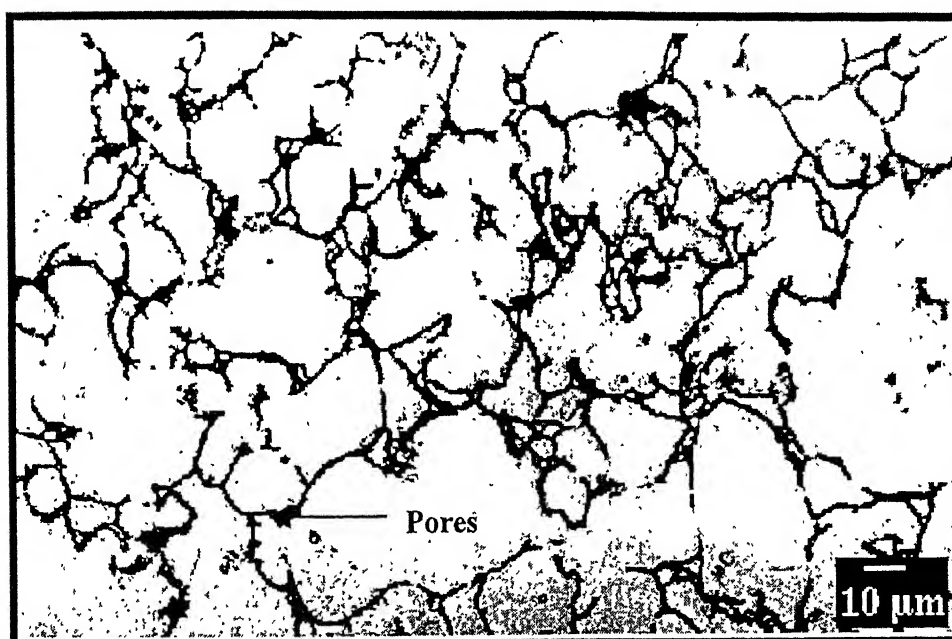


(b)

Figure 5.18. SEM micrograph of 316L+10% Y_2O_3 stainless steel composite sintered at 1250°C in (a) SE mode and (b) BSE mode showing the surface porosity.



(a)



(b)

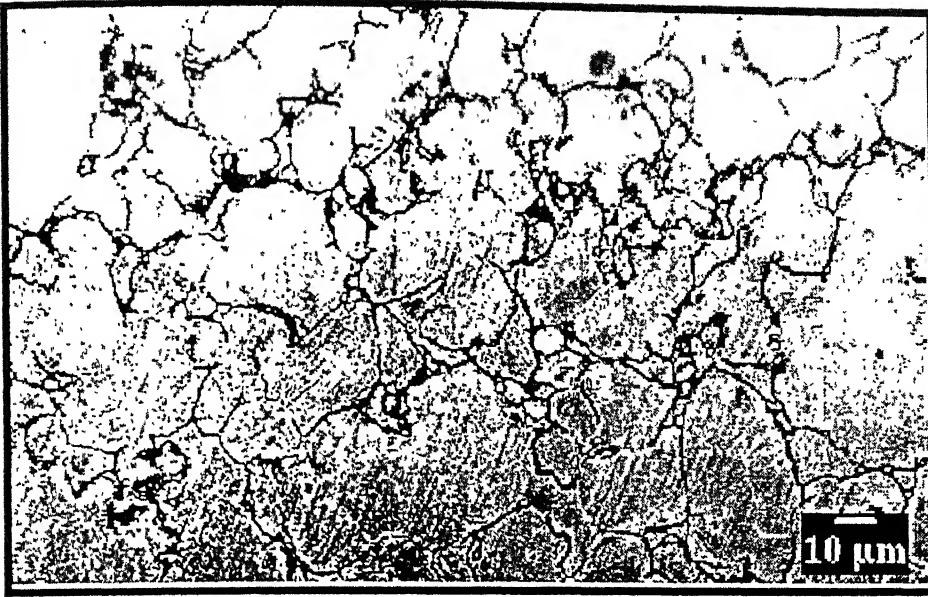
Figure 5.19. SEM micrograph of 316L+10% Y_2O_3 stainless steel composite sintered at 1400°C in (a) SE mode and (b) BSE mode showing the surface porosity.

The grain growth in the sample was higher than the sample sintered at 1250°C and the grains were brighter with no Y_2O_3 at the grain boundaries. Figure 5.20 reveals the microstructure of 316L + 10% Y_2O_3 composite sintered at 1250°C and 1400°C. The micrographs reveal that the sample sintered at 1400°C had higher grain growth than sample sintered at 1250°C. Moreover, Y_2O_3 was distributed throughout the surface of the sample when sintered at 1400°C. This accounts for the brightness on the sample surface. The Y_2O_3 dispersoids were concentrated in the grain boundaries in the sample sintered at 1250°C as shown in Figure 5.20 (a).

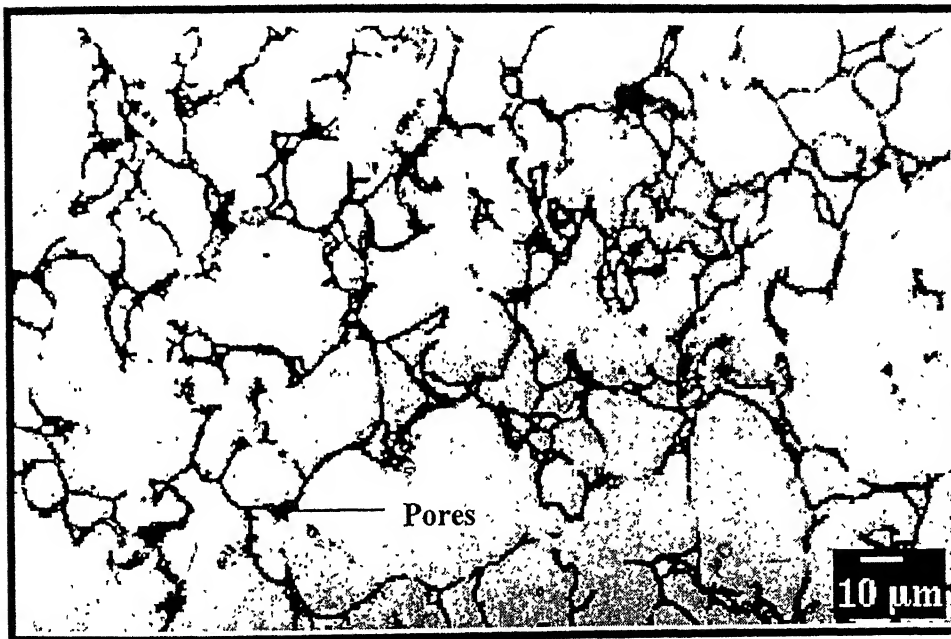
Figure 5.21 shows the microstructure of 434L + 10% Y_2O_3 sintered at 1250°C in SE and BSE modes. Micrograph 5.21 (a) reveals the sample with Y_2O_3 segregated at the grain boundaries and micrograph 5.21 (b) shows the microstructure in SE and BSE mode in the same picture. The BSE mode reveals the pores at the grain boundaries of the sample. Figure 5.22 shows the microstructure of 434L + 10% Y_2O_3 composite sintered at 1400°C. Micrograph (a) shows a single grain of the composite with Y_2O_3 dispersed uniformly on the sample surface. The grain growth was higher in the case of the sample sintered at 1400°C. Micrograph (b) shows the microstructure in both SE mode and BSE mode in the same picture. Figure 5.23 compares the 434L composite samples sintered at 1250°C and 1400°C. The micrographs reveal that the sample sintered at 1400°C has more rounded pores and the Y_2O_3 dispersoids are uniformly distributed in the grains. In the case of the sample sintered at 1250°C, the dispersoids are concentrated along the grain boundaries as shown in Figure 5.23 (b).

5.1.2. Discussions

The results obtained in the present work are discussed in this part. The first section of the discussion summarizes the densification behavior of the stainless steel samples sintered at the two temperatures and are compared with their wrought counterpart. This section also includes the weight losses involved in the samples along with the radial and axial shrinkage behavior. The second section discusses the metallography part which includes the discussions for optical and SEM micrographs.

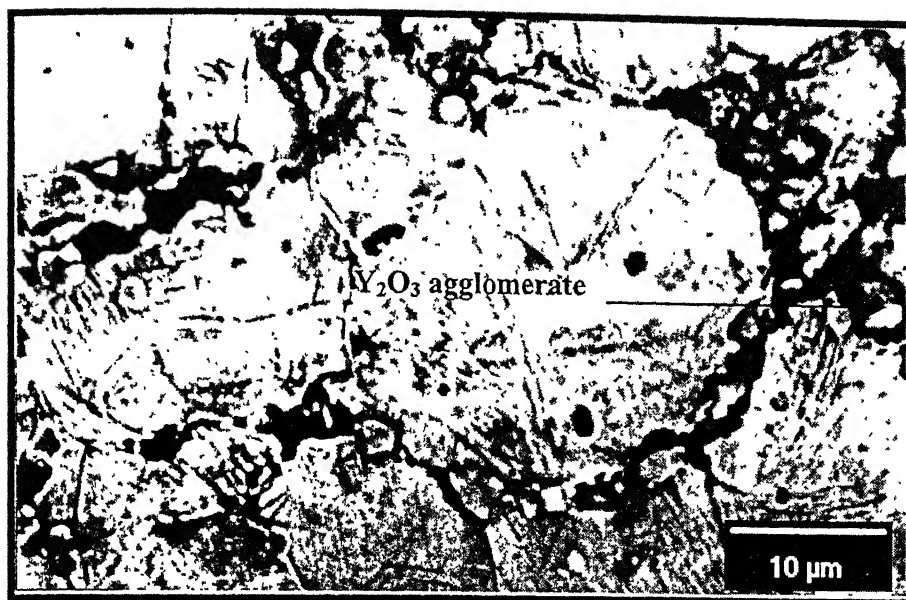


(a)

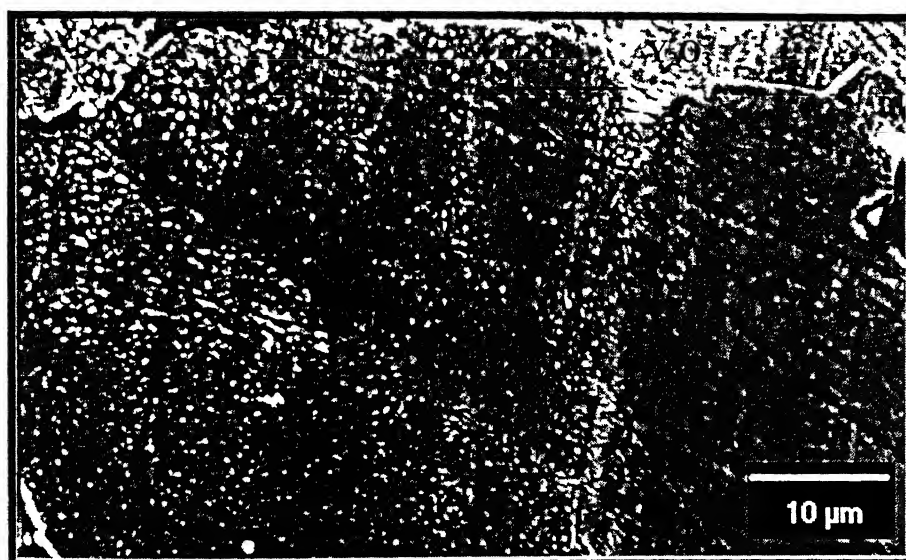


(b)

Figure 5.19. SEM micrograph of 316L+10% Y_2O_3 stainless steel composite sintered at 1400°C in (a) SE mode and (b) BSE mode showing the surface porosity.

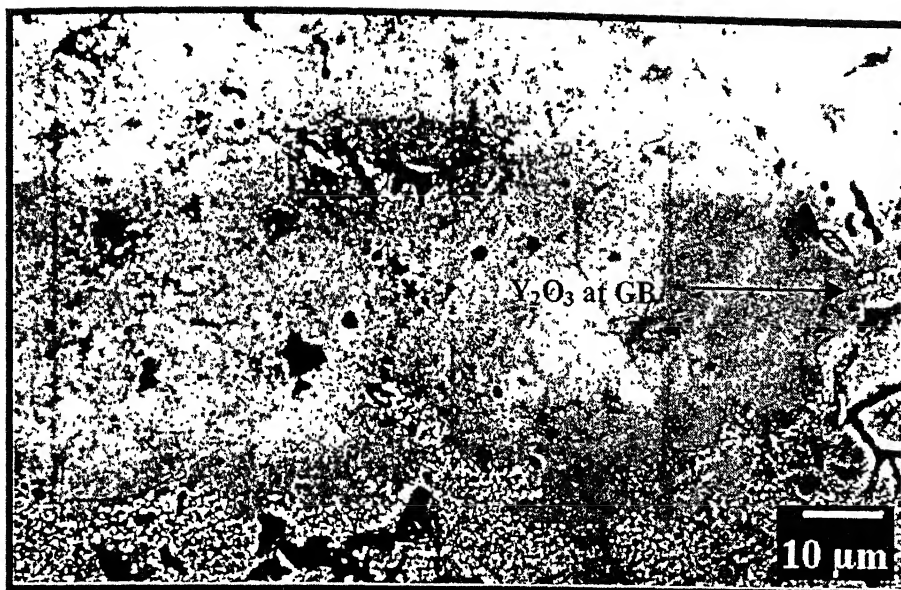


(a)

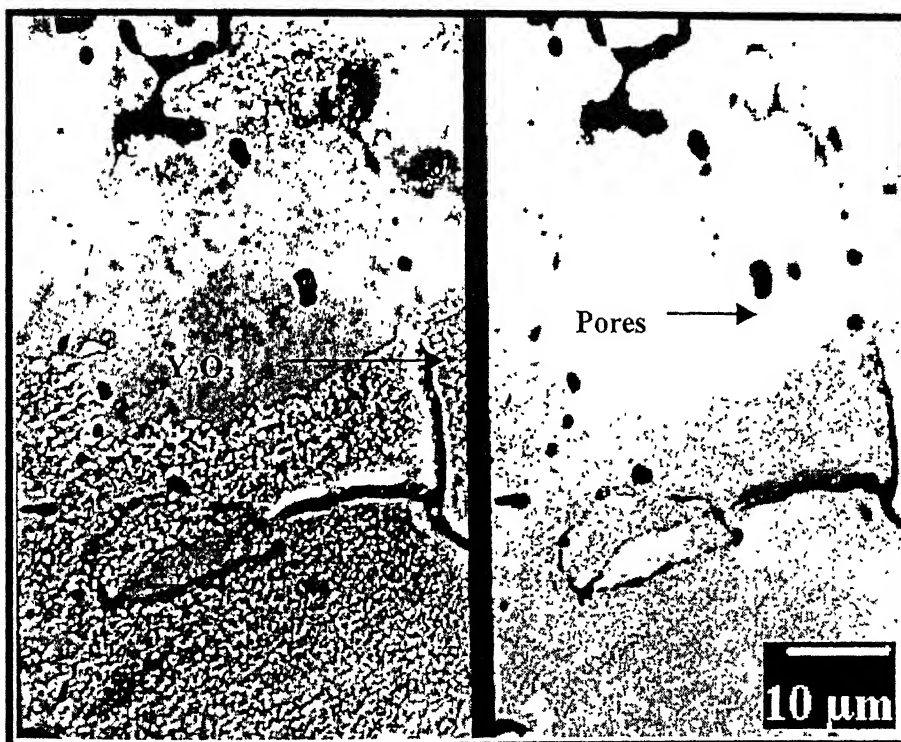


(b)

Figure 5.20. SEM micrograph of 316L+10% Y₂O₃ stainless steel composite sintered at (a) 1250°C and (b) 1400°C showing arrangement of Y₂O₃ at the surface.



(a)

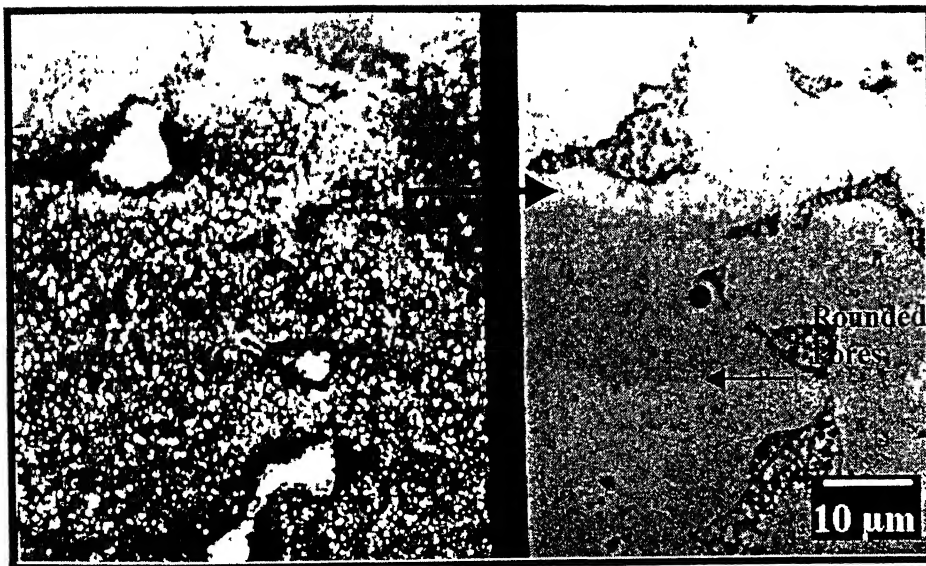


(b)

Figure 5.21. SEM micrograph of 434L+10% Y₂O₃ sintered at 1250°C showing Y₂O₃ dispersions in (a) SE mode and (b) SE and BSE modes.

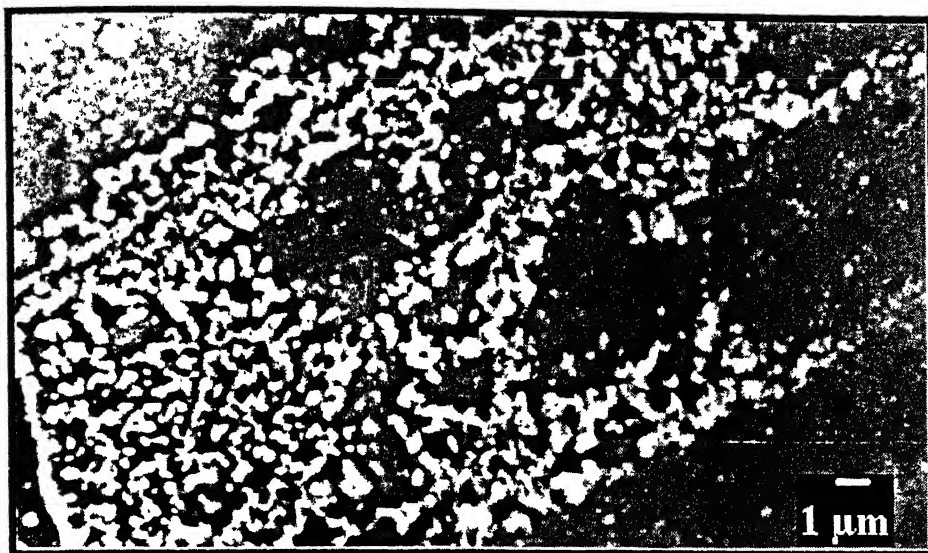


(a)

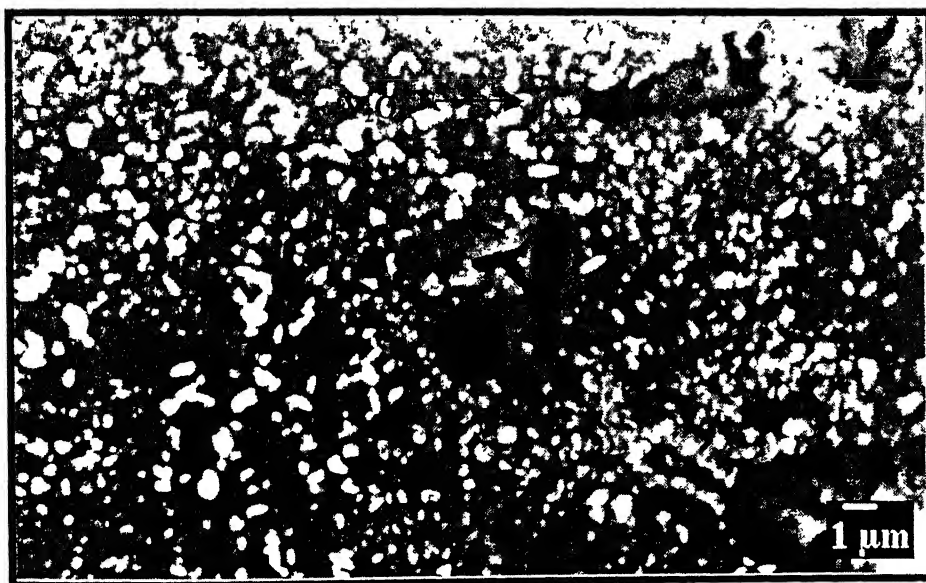


(b)

Figure 5.22. SEM micrograph of 434L+10% Y_2O_3 sintered at 1400°C showing Y_2O_3 dispersions in (a) SE mode and (b) BSE mode.



(a)



(b)

Figure 5.23. SEM micrograph of 434L+10% Y_2O_3 sintered at (a) 1250°C and (b) 1400°C showing the dispersion of Y_2O_3 on the surface.

5.1.2.1. Variation In Densification Behavior

As described earlier two sintering temperatures were selected for the present work. The effects of temperature on the sintered densities of the P/M stainless steels with and without oxide dispersions were studied. The solid state sintering of the samples were carried out at 1250°C for both ferritic and austenitic samples. Extensive research has been carried out on the solid state sintering of stainless steel samples and their particulate composites [62-69]. Supersolidus liquid phase sintering was carried out at 1400°C, which was between the solidus and liquidus temperature of stainless steel. Tandon [24] reported supersolidus liquid phase sintering of stainless steel with bronze additives at 1250°C and the bronze present in the sample resulted in lowering the sintering temperature. In the present work the effect of different sintering temperatures on both ferritic and austenitic stainless steel were compared. Effect of pressure on sintered densities was also considered and the results from the various experiments are summarized in the chapter.

The ferritic and austenitic stainless steel samples were compacted with applied pressures of 200, 300, 400 and 600 MPa. From Figure 5.2, it could be found that the samples compacted at 600 MPa exhibited higher sintered densities. This can be attributed to the higher green densities of the samples when compacted at higher pressure. The figure also compares the effect of temperature on the sintered densities of stainless steel samples. Samples sintered at 1400°C was having higher sintered densities than samples sintered at 1250°C, as the liquid formation occurs at 1400°C increases the sintered densities of the sample. Hence on summarizing Figure 5.2 it can be stated that the stainless steel samples compacted at a higher pressure and sintered at a higher sintering temperature yields higher sintered densities. The same was reported by Mukerjee [69] in his work on Al_2O_3 sintered ferritic stainless steels.

The effect of yttria addition on the sintered densities of the samples was given by Figure 5.4, show that the sintered densities decrease with increase in the yttria addition. The same was observed by Lal [62] and reported that this can be attributed to the lower green densities of the samples when yttria is added. The presence of second phase particles decrease the compressibility of the gas atomized powders leading to decrease in green density and subsequently the sintered density as shown in Appendix III and IV. But there was an exception in the case of 434L+10% yttria sample sintered at 1250°C, where

the sintered density increases comparable to the sintered density of the straight sample. The reason for this increase in sintered density was not so clearly understood. This can be attributed to the higher diffusion rate in the ferritic samples when compared with the austenitic sample.

Densification parameter gives the densification behavior of the compacts normalized with the green density. Appendix I and II shows the variation densification parameter for the stainless steel samples with compaction density. The trend was similar as that of the sintered density. The sample compacted with higher pressure and sintered at higher temperature resulted in higher densification parameter. Appendix III and IV compares the variation of densification parameter for the stainless steel composites with varying yttria content. The densification parameter decreases with increasing yttria content except for the 434L+10% yttria sample sintered at 1250°C. The trend was similar to that of the sintered density of the samples.

Figures 5.6 to Figure 5.9 compares the variation of radial and axial shrinkage in 434L and 316L samples sintered at 1250°C and 1400°C. Figure 5.6 and Figure 5.7 show the variation of radial and axial shrinkage in 316L and 434L with compaction pressure. The samples compacted at various pressures does not show a clear behavior in their radial and axial shrinkage. Figure 5.8 and Figure 5.9 compares the radial and axial shrinkage for stainless steel composites. The addition of yttria decreases the radial and axial shrinkage in 316L samples. 434L composites follow the same trend except the sample sintered at 1250°C with 10% yttria, which shows an increase in the shrinkage.

5.1.2.2. Microstructural Behavior

Microstructural evolutions of the stainless steel samples were observed by optical microscopy and SEM as a function of sintering temperature and yttria content. Optical micrographs capture the change in porosity in the samples as a function of temperature and yttria content. SEM micrographs capture the variation in the microstructure with yttria as a function of temperature.

The optical micrographs of 316L stainless steel samples and their composites are compared from Figure 5.12 to 5.15. The optical micrographs reveal the pore morphology of the samples. The pore concentrations in the samples sintered at 1400°C were lower when compared to the samples sintered at 1250°C. This can be attributed to supersolidus

liquid phase sintering that occurs at 1400°C. At 1400°C, liquid forms within each particle and as a consequence, each particle undergoes fragmentation and repacking, giving rise to a homogenous distribution of liquid. This results in increased sintering rate and higher sintered density of the sample. Moreover due to the liquid formation the pores tend to be more rounded than the normal solid state sintering where the pores are irregular. The optical micrographs of 434L stainless steel samples and their composites are compared in Figures 5.16 and 5.17. The straight 434L stainless steel samples follow the same trend as the austenitic samples. In the case of composites the behavior gets reversed. The sample sintered at 1250°C shows lower porosity than the sample sintered at 1400°C. The reason for this would be explained by the SEM micrographs of the samples.

The SEM micrographs of 316L+10% yttria are shown in Figures 5.18 and 5.19 sintered at 1250°C and 1400°C respectively. Each figure shows two micrographs one in scanning electron mode (SE) and other in the back-scattered electron mode (BSE). BSE mode does not reveal the yttria dispersoids and hence focuses only on the surface morphology of the samples. The micrographs reveal higher porosity in the sample sintered at 1250°C than the sample sintered at 1400°C. Moreover, yttria agglomerates were seen at the grain boundaries in the sample sintered at 1250°C. This feature is more clearly seen in Figure 5.20. The grain boundaries are the low energy sites. When the samples were sintered at solid state temperature the oxide dispersoids diffuse to the grain boundaries. This results in the yttria agglomerates at the grain boundaries. When the sample was sintered at 1400°C, liquid formation occurs and the oxide dispersoids get uniformly distributed all over the grain. Figure 5.20(b) elucidates this explanation. The SEM micrographs of 434L stainless steel composites were shown in Figures 4.21-4.23. The micrographs follow the same trend as that of the austenitic samples. But in this case the yttria particles concentrated at the grain boundaries cover up the pores present at the grain boundaries. This is the only possible explanation for the increase in the density of the sample sintered by solid state sintering. Moreover the diffusion in ferritic stainless steel is faster than austenitic stainless steel and hence this increase in density was found only in the case of ferritic stainless steel composites.

5.2. Corrosion

The P/M stainless steel samples were studied by several electrochemical tests to understand the corrosion behavior of the samples. Results for ferritic stainless steel samples will be presented first followed by those for the austenitic stainless steel samples. In each case the potentiodynamic polarization behavior, corrosion rate by Tafel extrapolation), cyclic polarization behavior and electrochemical impedance behavior (EIS) would be addressed. The effects of P/M processing, sintering temperature and Y_2O_3 addition on the electrochemical behavior of the samples will be discussed. The results for the ferritic 434L and austenitic 316L grades would be finally compared.

5.2.1. Potentiodynamic polarization

Ferritic stainless steel

The potentiodynamic studies were carried out in freely aerated 0.05 mol/l (pH=1) sulfuric acid. The polarization experiments were conducted at a scan rate of 1 mV/sec using Ag/AgCl in saturated KCl (SSC) as the reference electrode and platinum as the counter electrode. All the experiments were carried out after polishing the samples to a 4/0 finish. In the initial phase of studies, the free corrosion potential of the samples were allowed to stabilize in the electrolytic solution before conducting the polarization experiments. A typical stabilization of free corrosion potential (FCP) vs time for the wrought 316L sample is shown in Figure 5.24. The nature of these curves indicated progressive surface film formation on immersion. The FCP was initially established in the active potential region and after a certain period of time moved up rapidly towards nobler potentials and then stabilized (curves A and B in Figure 5.24). In some cases, the potentials moved to the noble direction at a relatively low rate of change (curve C in Figure 5.24). The potential finally stabilized at various potential values, even for the same sample on repeated experiments, indicating the possible differences in the nature and stability of the surface film. The potentials stabilized in a nobler positive potential indicating the formation of a passive film. Otero et al. [49] reported similar variation of free corrosion potential for P/M 316L stainless steel in solutions of 1 to 50% sulfuric acid

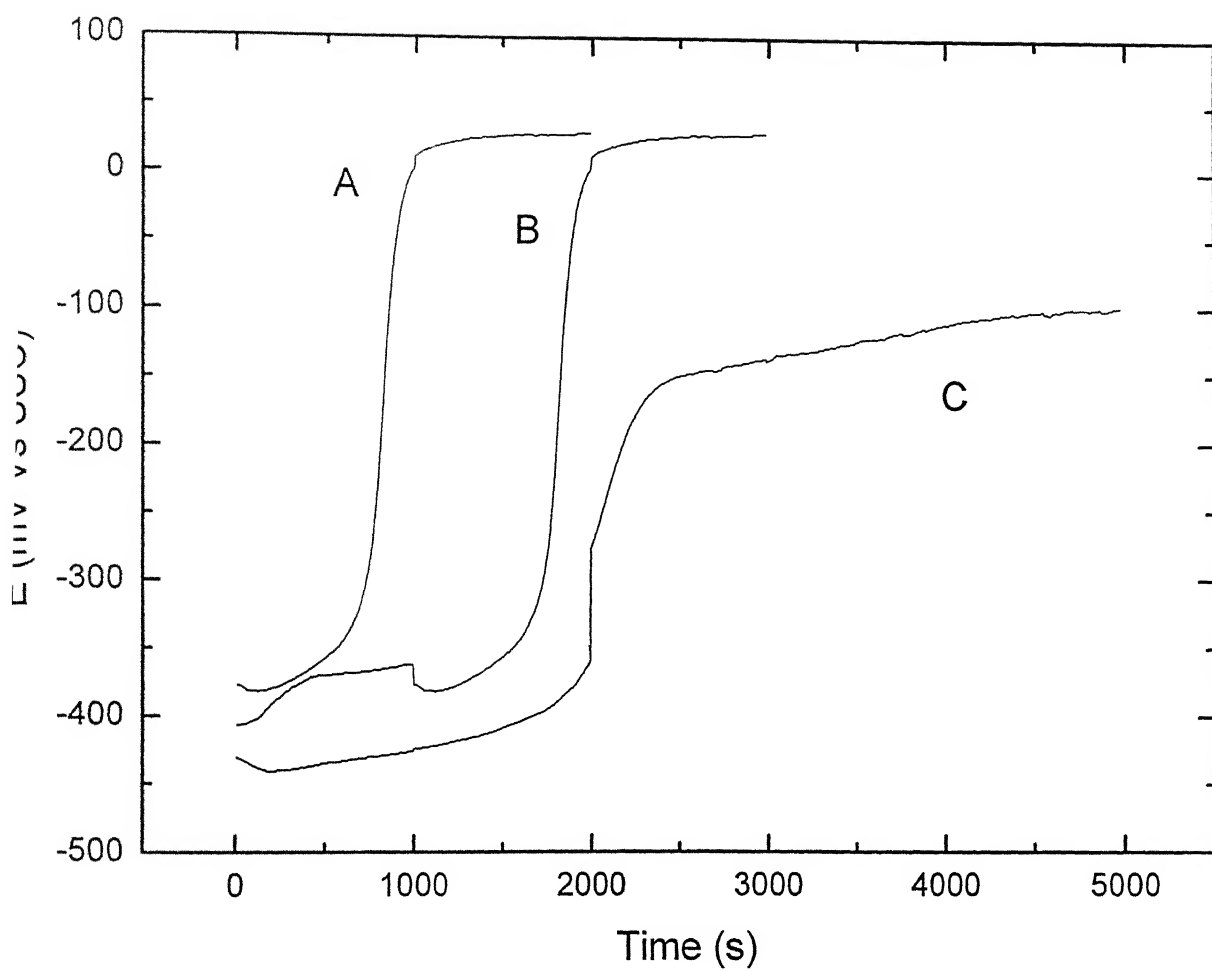


Figure 5.24. Three different experiments of variation of ZCP vs time in 0.05 mol/l H_2SO_4 solution for 316L standard.

and phosphoric acid. The final stabilization of FCP was not reproducible consistently. Therefore, the potentiodynamic polarization experiments were conducted immediately on immersion of the samples. This procedure resulted in potentiodynamic polarization behavior that was reproducible consistently.

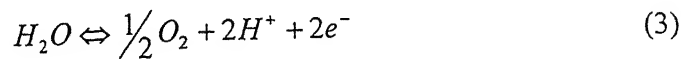
The potentiodynamic polarization curves for the P/M 434L ferritic stainless steels sintered at 1250°C, are compared with 430L standard in Figure 5.25. All the alloys exhibited active-passive behavior. The values of passive current density (i_{pass}), critical current density (i_{crit}), zero current potential (ZCP), primary passivation potential (E_{pp}), complete passivation potential (E_{cp}), pitting potential (E_p), breakdown potential (E_{bp}) and transpassive potential (E_{tp}) were obtained from the potentiodynamic polarization curves and these are summarized in Table 5.1. Data from two reproducible experiments are provided in the table and the results indicated that the experiments were reproducible, barring some minor variations.

In order to obtain some insights on the reduction reaction in the portion of the polarization diagram, the ZCP can be compared with the reversible potential for hydrogen evolution reaction. Table 1 indicates that the ZCP values of the alloys were in the order of -530 mV vs SSC. The reversible electrode potential E_{rev} for hydrogen evolution reaction (equation 1) is given by the Nernst equation as in equation (2).



$$E_{rev} = E_{H^+/H}^0 - 0.059 pH(SHE) \quad (2)$$

The pH of the sulfuric acid solution used was measured accurately by a pH meter and found to be as 1. The potential of the SSC electrode was 197 mV with respect to the SHE. The equilibrium potential for the hydrogen evolution reaction was calculated as -256 mV vs SSC. As the ZCP's were active compared to this value, hydrogen evolution can be considered to be the dominating cathodic reaction. The transpassive potential (E_{tp}), for the samples were well above the equilibrium potential of +1364 mV vs SSC for the oxygen evolution reaction. The equilibrium reaction for oxygen evolution and the corresponding E_{rev} for the reaction are given below.



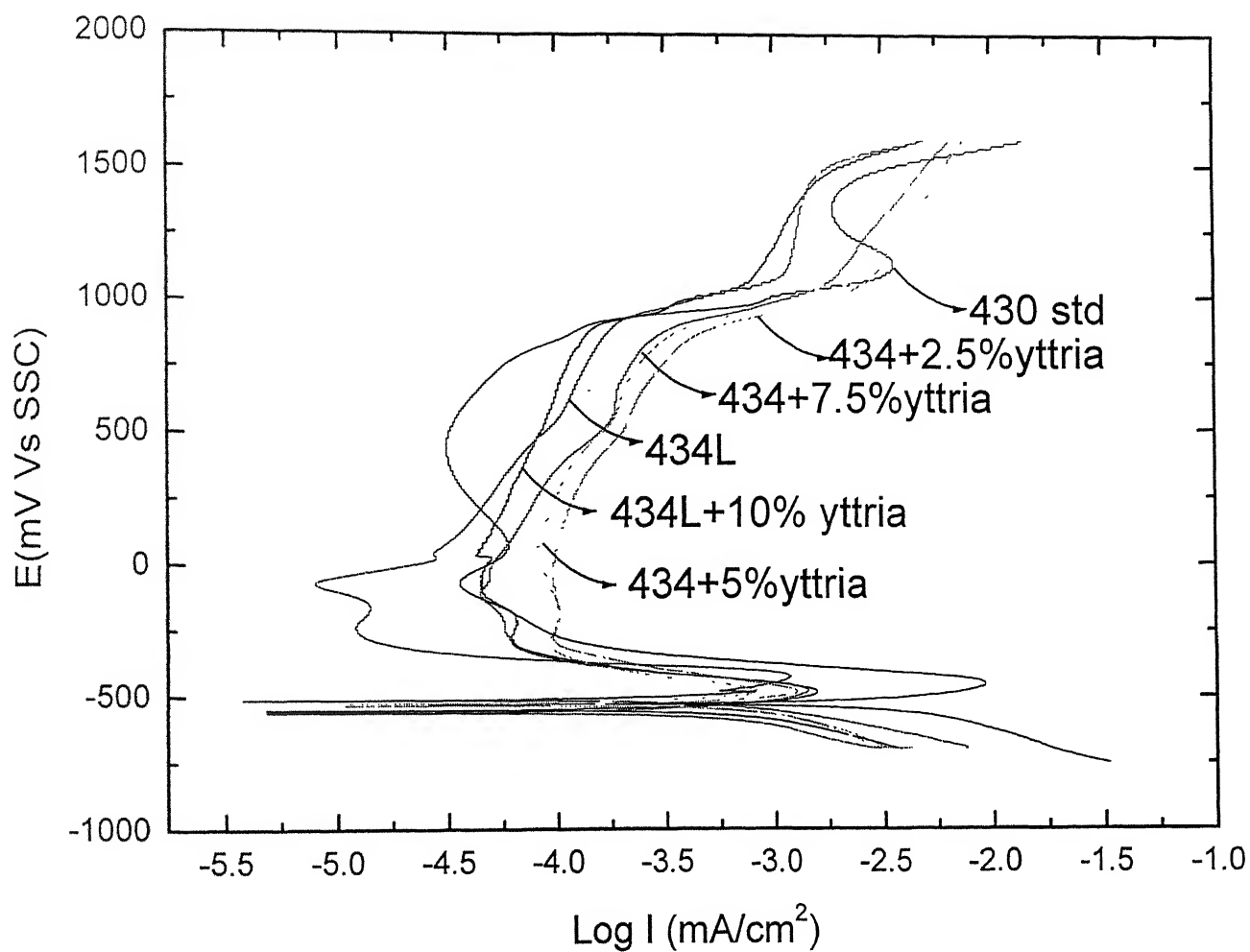


Figure 5.25. Potentiodynamic polarization curves for 430L standard, 434LP/M and 434L composites sintered at 1250°C .

Table 5.1. Passivity parameters obtained for potentiodynamic polarization curves for 434L samples sintered 1250°C.

Sample	i_{crit} (mA/cm ²)	ZCP (mV Vs SSC)	i_{pass} (mA/cm ²)	E_{cp} (mV Vs SSC)	E_p (mV Vs SSC)	E_{bp} (mV Vs SSC)	E_{ip} (mV Vs SSC)
430(std)	10.7100	-523	0.0295	-248	821	1060	1460
	9.3325	-523	0.0309	-248	827	1060	1460
434L	1.0230	-517	0.1690	-254	876	1100	1500
	1 2020	-517	0.1230	-248	853	1080	1470
434L+2.5%yttria	1.4125	-556	0.1862	-282	871	1060	
	1.4125	-550	0.1621	-285	871	1060	
434L+5%yttria	0.8317	-550	0.2291	-282	871	1060	
	1.3803	-531	0.5012	-282	871	1090	
434L+7.5%yttria	1.2302	-537	0.1445	-288	871	1060	
	1.2302	-537	0.1445	-288	871	1060	
434L+10% yttria	1.5135	-550	0.1202	-288	884	1070	1460
	1.5135	-550	0.1698	-288	890	1060	1460

$$E_{rev} = E_{O_2/OH^-}^{\circ} - 0.059 pH(SHE) \quad (4)$$

From the value of pH and E_{O_2/OH^-}° (1226 mV Vs SHE), the E_{rev} was calculated to be as 1364 mV. Therefore the gas evolved in the transpassive region on the sample was oxygen.

In the passive region, passive current densities are not constant but exhibit variation. For example, in Figure 5.25, the P/M 434L sample exhibits a wide passive region. In the potential around -70 mV and +500 mV vs SSC the current densities are very low, then exhibit an increasing trend with increasing potentials, until pitting of the surface. The variation of passive current densities reflects the differing nature of the passive film as a function of potential. Further insights into the passive film nature as a function of potential were obtained using EIS. Electrochemical impedance measurements were obtained at different applied potential conditions for 434L P/M sample sintered at 1250°C. The chosen potentials for study were: (a) freely corroding condition, (b) -70 mV vs SSC, (c) +500 mV vs SSC and (d) +1250 mV vs SSC. The results of the impedance study is presented in the Bode frequency plot in Fig 5.26, from which it can be concluded that the surface film formed at +500 mV vs SSC exhibits better capacitance and hence the best among the potentials studied at four potentials. The passive film at a potential of +500 mV vs SSC is less porous compared to the film formed at -70 mV vs SSC. Therefore, i_{pass} values were noted at +500 mV vs SSC for all the samples and have been reported henceforth.

Figure 5.25 indicates that the potentiodynamic polarization behavior of the P/M 434L stainless steel was similar to that of the wrought 430L sample. The critical current density for passivation of the P/M sample was, however, much lower than the wrought sample. The passive current densities of the P/M samples were an order of magnitude higher than that of the wrought sample. This difference may arise due to the inherent porosity present in the P/M sample.

The potentiodynamic curves of P/M stainless steel composites containing various percentages of Y_2O_3 are also compared in Figure 5.25. Compared to the 430 standard sample, the i_{crit} was lower in all the composite samples and i_{pass} was higher. As regard, the variation with Y_2O_3 addition, i_{pass} apparently appears to increase marginally, reaching a

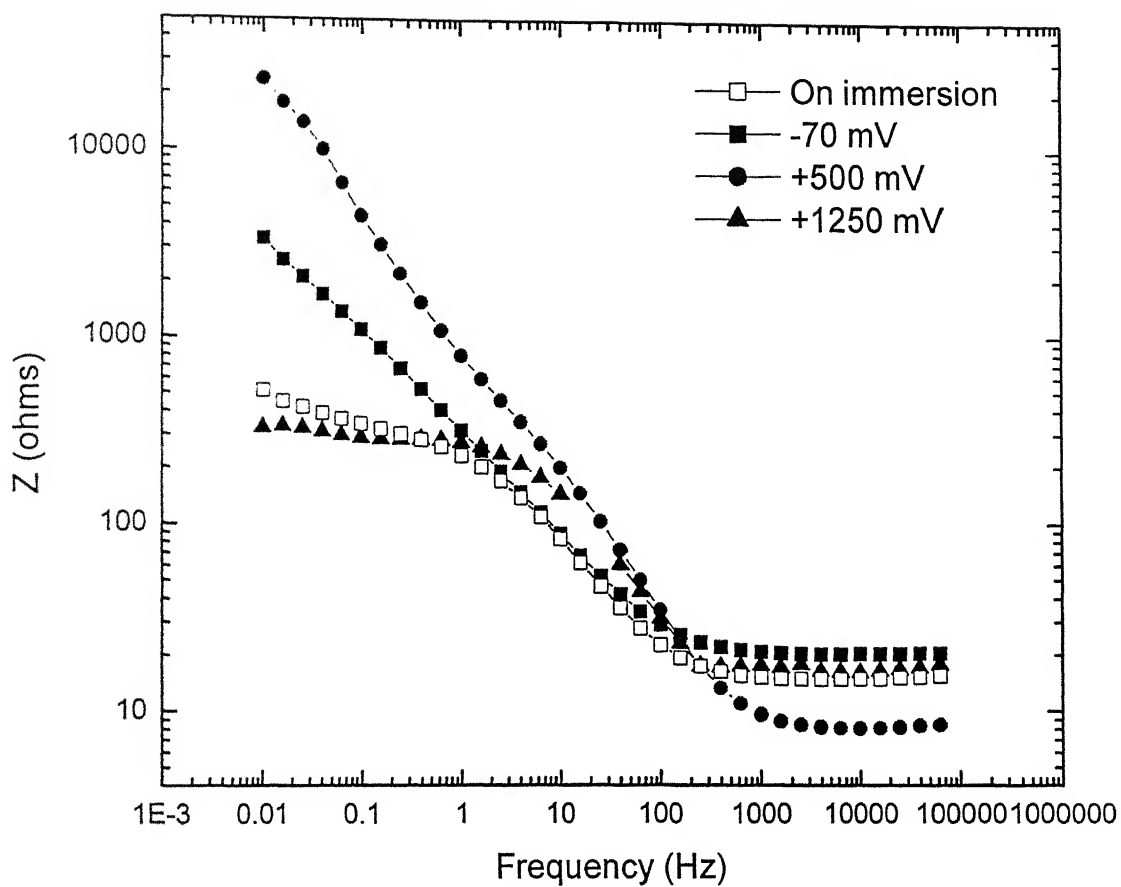


Figure 5.26. Bode frequency plot at various potentials for 434L P/M stainless steel sintered at 1250°C.

maximum for 5% Y_2O_3 and then decreases for 10% Y_2O_3 to reach the value similar to that of the straight P/M 434L sample. However the difference in i_{pass} are not so significant for the composites it can be concluded similar to that of the P/M 434L sample. The addition of Y_2O_3 does not have a marked alteration in the i_{crit} , ZCP, E_{cp} , E_p , E_{bp} and E_{tp} values of the P/M samples. It is important to note that the passive current densities are not affected significantly by Y_2O_3 addition. The secondary passivity region, which was noticed in the wrought and 434L straight samples, was not observed for the P/M composite samples except for the sample with 10% Y_2O_3 .

The potentiodynamic polarization curves for the P/M 434L stainless steel samples, sintered at 1400°C, were compared with 430L standard sample in Figure 5.27. The passivation parameters like ZCP, E_{cp} , E_p , E_{bp} , E_{tp} , i_{crit} and i_{pass} from these curves are tabulated in Table 5.2. All the alloys exhibited active-passive behavior. The ZCP of the alloys were around -530 mV vs SSC, which was less than that of equilibrium potential for hydrogen evolution (-253 mV vs SSC). Therefore, hydrogen evolution was considered as the dominant cathodic reaction. As noted for the 1250°C sintered samples, the P/M samples exhibited lower i_{crit} than the 430L wrought sample. However, the passive current density of the 434L straight P/M sample was comparable to that of the wrought sample. This can be attributed to the higher sintered density of the P/M sample due to higher sintering temperature utilized (1400°C). The critical current densities for passivation of the composites were an order magnitude higher when compared with the wrought sample but similar to the P/M 434L sample. On comparing the P/M samples, the i_{pass} value was similar for 430L, 434L P/M sample and 434L + 2.5% P/M composites. The addition of Y_2O_3 dispersoids increased the passive current density in the 5%, 7.5% and 10% Y_2O_3 composites. This behavior was unlike the samples sintered at 1250°C. All the alloys except the composite with 7.5% Y_2O_3 indicated the transpassive behavior. The transpassive potential (E_{tp}) was higher than +1364 mV vs SSC for all the alloys and hence was attributed to oxygen gas evolution. There was no marked difference in the other parameters like ZCP, E_{cp} , E_p , E_{bp} , E_{tp} and i_{crit} for the samples sintered at 1400°C.

On comparing the potentiodynamic polarization behavior of the ferritic stainless steel samples sintered at 1250°C and 1400°C, the following can be concluded. The ZCP, E_{cp} , E_p , E_{bp} , E_{tp} parameters were similar for the samples. The main parameters that

exhibited differences were the critical current density and passive current density. Critical current density provides insights about passive film nucleation and growth while passive current density provides information about the nature of the passive film. The values of i_{crit} were similar for all the composites sintered at both 1400°C and 1250°C. The i_{crit} was lower than that of the 430 standard wrought sample. This may be attributed to the presence of Mo in the 434L samples. Ahlberg *et al.* [53] indicated the same type of behavior during potentiodynamic polarization of 304L and 316L P/M stainless steels in 0.5 mol/l sulfuric acid. In case of the straight samples, the sample sintered at 1400°C had a lower i_{pass} than the sample sintered at 1250°C, which can be attributed to the lower porosity in the 1400°C sintered sample.

Considering the effect of Y_2O_3 addition, i_{pass} of the composite samples sintered at 1250°C did not show significant change with Y_2O_3 addition. An interesting effect due to the presence of Y_2O_3 on the sintering nature must be realized. Segregation of Y_2O_3 occurs at the grain boundaries during sintering at 1250°C and this decreases the passive current densities of the sample. In the case of 1400°C sintered samples, the liquid phase disperses the Y_2O_3 particles in the matrix of the metal and do not decrease the porosity. Therefore, the higher passive current density obtained with Y_2O_3 addition (greater than 5%) could be related to this effect.

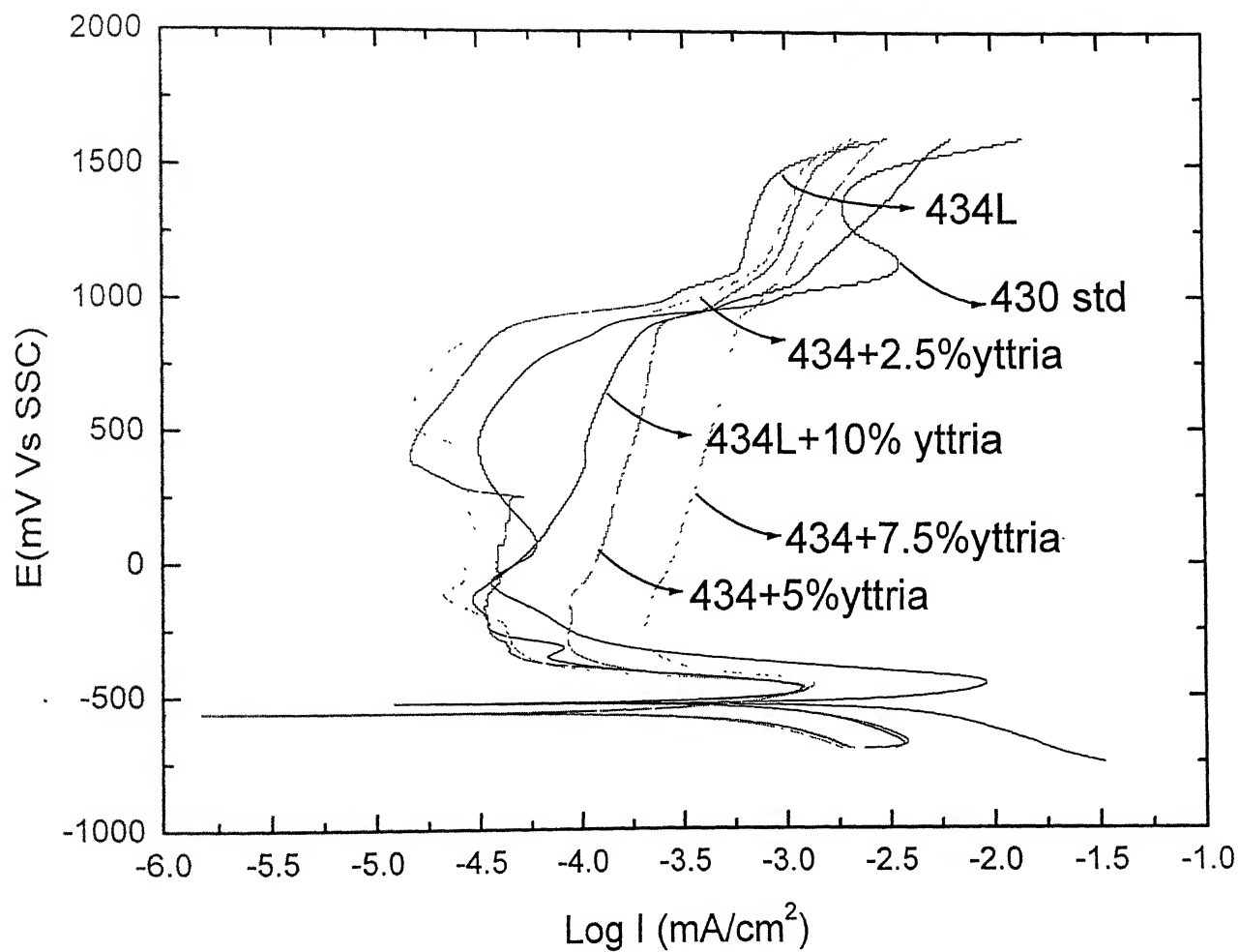


Figure 5.27. Potentiodynamic polarization curves for 430L, 434L and 434L composites sintered at 1400°C.

Table 5.2. Passivation parameters obtained for potentiodynamic polarization curves for 434L samples sintered at 1400°C.

Sample	i_{crit} (mA/cm ²)	ZCP (mV Vs SSC)	i_{pass} (mA/cm ²)	E_{cp} (mV Vs SSC)	E_p (mV Vs SSC)	E_{bp} (mV Vs SSC)	E_{tp} (mV Vs SSC)
430(std)	10.7100	-523	0.0295	-248	821	1060	1460
	9.3325	-523	0.0309	-248	827	1060	1460
434L	0.9120	-530	0.0151	-267	869	1120	1470
	1.2589	-530	0.0144	-248	853	1100	1480
434L+2.5%yttria	1.0715	-568	0.0169	-245	847	1100	1460
	1.2589	-568	0.0144	-228	847	1090	1480
434L+5%yttria	1.3182	-556	0.4677	-345	885	1150	1530
	1.1748	-556	0.2450	-337	884	1110	1510
434L+7.5%yttria	1.2882	-562	0.9120	-374			
	1.3489	-562	0.5888	-270	914	1070	
434L+10%yttria	1.3489	-531	0.1122	-276	884	1100	1510
	1.2302	-537	0.1023	-239	871	1050	1520

The potentiodynamic polarization curves of 316L wrought standard, 316L P/M sample and 316L composites sintered at 1250°C are compared in Figure 5.28. The passivity data from the polarization diagram have been tabulated in Table 5.3. All the samples exhibited active-passive behavior except the 316L P/M sample. The potentiodynamic polarization behavior of the 316L P/M sample indicated a different behavior (stable passive), which occurred in repeated experiments. The reason for the difference of this particular sample compared to others is not well understood. The ZCP values of the samples, except the 316L P/M sample were well above the equilibrium potential for hydrogen evolution (-253 mV vs SSC) reaction $2H^+ + 2e^- \rightleftharpoons H_2$. Therefore, hydrogen evolution was considered to be the dominating cathodic reaction. A secondary passive region was clearly seen (from +1200 mV to +1400 mV vs SSC) for the wrought 316L sample. This behavior was not observed in all the P/M alloys. The transpassivity potential (E_{tp}) was well above than the equilibrium potential (+1364 mV vs SSC) for the reaction $H_2O \rightleftharpoons \frac{1}{2}O_2 + 2H^+ + 2e^-$. Therefore, the gas evolved during transpassivity can be oxygen. The 316L wrought sample possessed lower i_{pass} value than all P/M samples, which may be attributed to the inherent porosity in the P/M samples. It was also noticed that the P/M sample possessed higher i_{crit} than the wrought sample. The comparison of the P/M stainless steel composites with the wrought sample indicated that the addition of Y_2O_3 to the 316L did not significantly affect i_{pass} and i_{crit} . Therefore, addition of Y_2O_3 did not significantly degrade the passive film nature. There were no marked differences in the values of ZCP, E_{cp} , E_p and E_{bp} values of the P/M stainless steel composites sintered at 1250°C.

The potentiodynamic polarization curves of 316L wrought sample, 316L P/M and 316L P/M composites sintered at 1400°C are compared in Figure 5.29. The passivation parameters have been recorded in Table 5.4. All the alloys indicated active-passive behavior. From the polarization data, it was evident that the i_{pass} value was the least for the wrought sample. In contrast to the P/M 316L samples sintered at 1250°C, the P/M stainless steel sample showed similar characteristics like the wrought sample, especially similar i_{pass} and i_{crit} value. The lower i_{crit} and i_{pass} for the P/M sample sintered at 1400°C

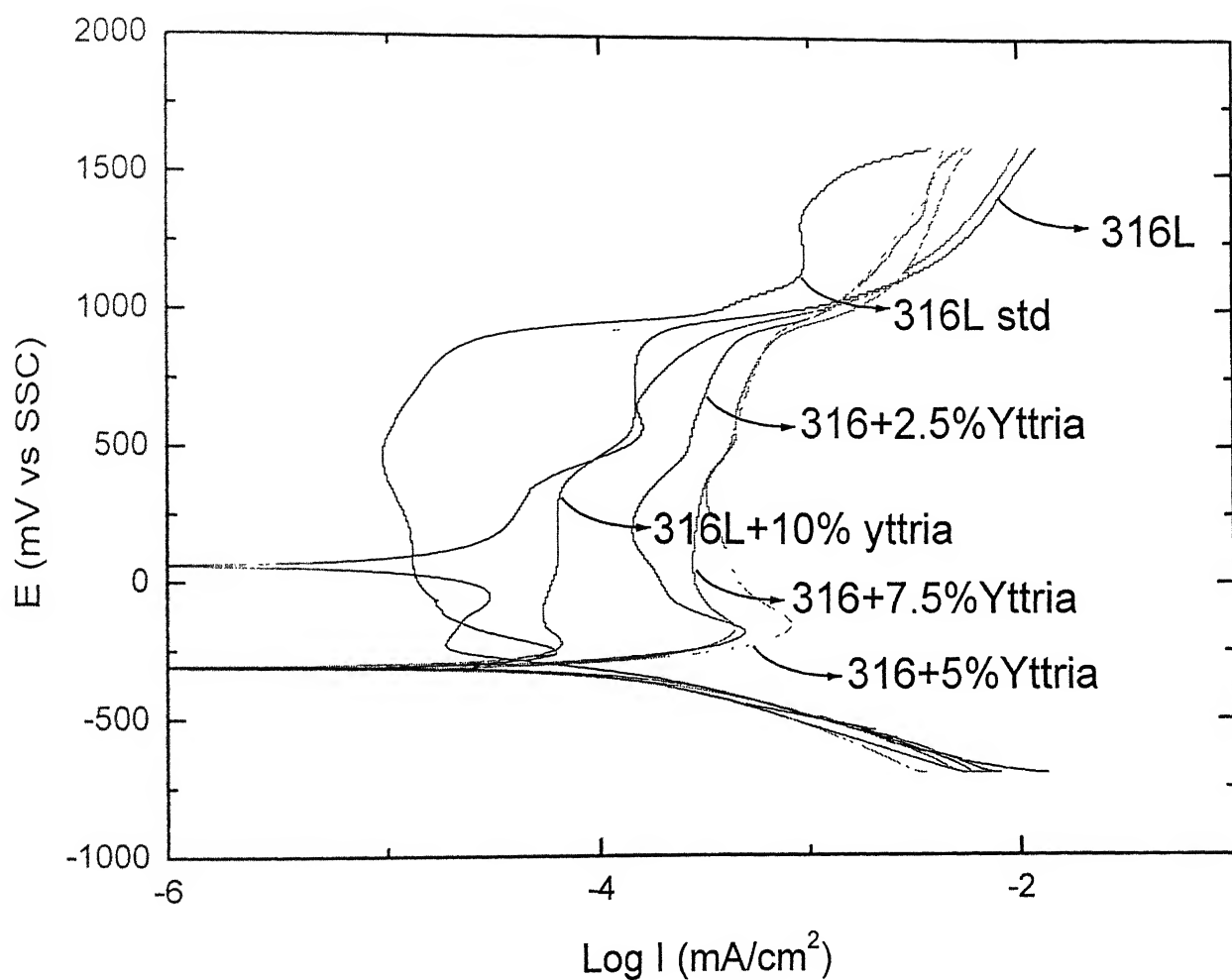


Figure 5.28. Potentiodynamic polarization plots for 316L wrought, 316L P/M and 316L P/M composites sintered at 1250°C.

Table 5.3. Passivation parameters obtained for potentiodynamic polarization curves for 316L wrought, 316L P/M and 316L P/M composites sintered at 1250°C.

Sample	i_{corr} (mA/cm ²)	ZCP (mV vs SSC)	i_{pass} (mA/cm ²)	E_{cp} (mV vs SSC)	E_p (mV vs SSC)	E_{bp} (mV vs SSC)	E_{tp} (mV vs SSC)
316(std)	0.0707	-319	0.0067	-79	908	1190	1400
	0.0631	-319	0.0131	-79	914	1140	1400
316L	0.1513	53	0.1445	-	911	1170	-
	0.1949	79	0.2398	-	911	1190	-
316L+2.5%yttria	0.5012	-288	0.138	-79	920	1150	-
	0.0977	-307	0.0912	-97	920	1120	-
316L+5%yttria	0.8317	-300	0.3162	-79	914	1130	-
	0.3467	-300	0.2089	-85	908	1120	-
316L+7.5%yttria	0.2238	-325	0.1862	-116	908	1100	-
	0.4688	-331	0.2754	-91	914	1130	-
316L+10%yttria	0.1445	-313	0.0691	-138	902	1170	-
	0.0676	-313	0.0537	-144	902	1150	-

Table 5.4. Potentiodynamic polarization data for 316L wrought, 316L P/M and 316L P/M composites sintered at 1400°C.

Sample	i_{corr} (mA/cm ²)	ZCP (mV Vs SSC)	i_{pass} (mA/cm ²)	E_{cp} (mV Vs SSC)	E_p (mV Vs SSC)	E_b (mV Vs SSC)	E_{tp} (mV Vs SSC)
316(std)	0.0707	-319	0.0067	-79	908	1190	1400
	0.0631	-319	0.0131	-79	914	1140	1400
316L	0.0107	-306	0.0079	-67	911	1110	1490
	0.0154	-306	0.0083	-60	905	1140	1510
316L+2.5%yttria	0.3467	-350	0.1479	-60	902	1170	1450
	0.1148	-350	0.0813	-60	902	1100	1450
316L+5%yttria	0.1122	-331	0.0741	-73	902	1140	-
	0.1819	-331	0.1202	-73	902	1130	-
316L+7.5%yttria	0.3019	-331	0.1096	-73	902	1090	-
	0.1548	-325	0.1174	-79	896	1100	-
316L+10%yttria	0.0933	-306	0.1348	-34	927	1130	-
	0.0912	-306	0.1995	-27	940	1140	-

when compared to the P/M sample sintered at 1250°C must be related to the higher sintered density that was obtained on sintering at high temperature. This can be attributed to the inherent pores in the P/M sample, which increases the passive current density. On comparing the P/M composites with the straight P/M sample, it was evident that addition of second phase particles increased the i_{crit} and i_{pass} . Therefore, there was an effect due to Y_2O_3 addition on the passivation nature. However, the variation with Y_2O_3 addition was not significance. The P/M samples did not exhibit transpassivity. There were no marked changes in the values of ZCP, E_{cp} , E_p and E_{bp} for the ferritic stainless steel samples sintered at 1400°C.

Comparing the polarization data of 316L P/M stainless steel samples sintered at 1250°C and 1400°C, there was no marked difference in the values of ZCP, E_{cp} , E_p , E_{bp} and E_{tp} . Therefore, the only variation was in the i_{pass} values. The straight P/M stainless steel sample sintered at 1400°C possesses lower i_{pass} and i_{crit} than the sample sintered at 1250°C. This can be attributed to the better densification and properties of the sample when sintered by supersolidus liquid phase sintering. A different effect was observed for the composites. The 10% Y_2O_3 composite will be addressed. This can be attributed to the rare earth effect of Y_2O_3 . At 1250°C, the Y_2O_3 dispersoids were preferentially segregated at the grain boundaries, which resulted in pore closure. Therefore, the samples exhibited lower i_{pass} . In the sample sintered at 1400°C, due to the liquid phase formation inside the particles, the preferential segregation did not occur. This results in a uniform distribution of Y_2O_3 in the metal matrix. Therefore, the i_{pass} value was higher in the sample sintered at 1400°C.

5.2.2. Tafel Extrapolation

The Tafel extrapolation experiments were carried out in 0.05 mol/l sulfuric acid with Ag/AgCl (SSC) as the reference electrode and platinum as counter electrode. A scan rate of 0.166 mV/s was applied as specified in the ASTM standard [12]. The parameters ZCP, β_a , β_c (anodic and cathodic Tafel Slopes) and i_{corr} were estimated and these have been tabulated in Tables 5.5 to 5.8. All the original experimental Tafel data have been provided in the Appendix. The corrosion rate was calculated using the formula [5],

$$\text{Corrosion rate (mpy)} = (i_{corr})(\Lambda)(1/\rho)(\epsilon)(1/A) \quad (1)$$

where Λ is the conversion factor of 1.2866×10^5 , ρ is the density of the sample in g/cm^2 , ϵ is the equivalent weight of the sample in g and A is the area of the sample exposed in cm^2 . The values of β_a and β_c were calculated by measuring the slope of at least one decade in the anodic and cathodic curves, respectively. One decade of linearity was not generally obtainable in the anodic region. However, the cathodic Tafel curve did possess a linearity of one-decade. The cathodic Tafel line was extrapolated and the point of intersection of this line with the horizontal drawn at ZCP was noted. By drawing a tangent from the intersection point to the anodic curve, β_a value was determined. Figure 5.30 details the method used for calculating the Tafel slopes. β_a values will be positive, as the anodic overpotentials are positive and similarly β_c value will be negative as the cathodic overpotentials are negative.

The results of Tafel method for the 430L wrought sample and P/M samples sintered at 1250°C and 1400°C are tabulated in Table 5.5 and 5.6, respectively. The i_{corr} values for the P/M samples were lower by an order of magnitude than that of the 430L wrought sample. This can be attributed to the compositional difference between 430L and 434L ferritic stainless steels. The presence of Mo in 434L P/M stainless steel samples can be the reason for the reduction in corrosion rate. The same behavior was noticed for 304L and 316L P/M samples by Ahlberg et al. [53] in 0.05 mol/l solution of sulfuric acid. The i_{corr} values and the corrosion rates of the P/M samples were comparable. The results indicate that addition of Y_2O_3 did not severely degrade the corrosion behavior of the P/M 434L ferritic samples. Moreover the i_{corr} for the P/M samples sintered at 1400°C were similar to that of the samples sintered at 1250°C .

The results of Tafel experiment for 316L wrought and 316L P/M samples have been tabulated in Table 5.7 (sintered at 1250°C) and 5.8 (sintered at 1400°C). The corrosion rates of the P/M samples were comparable with that of the wrought sample. Further, there was no significant effect of Y_2O_3 addition or sintering temperature on the corrosion rates. It must be noticed that the β_a and β_c slopes (Table 5.7 and 5.8) were lower in the case of the austenitic P/M samples when compared with the ferritic grade (Table 5.5 and 5.6). Moreover, the corrosion rates for the austenitic grade were lower than that of the ferritic grade. This can be attributed to the presence of nickel in the austenitic grade, which results in better corrosion resistance [2].

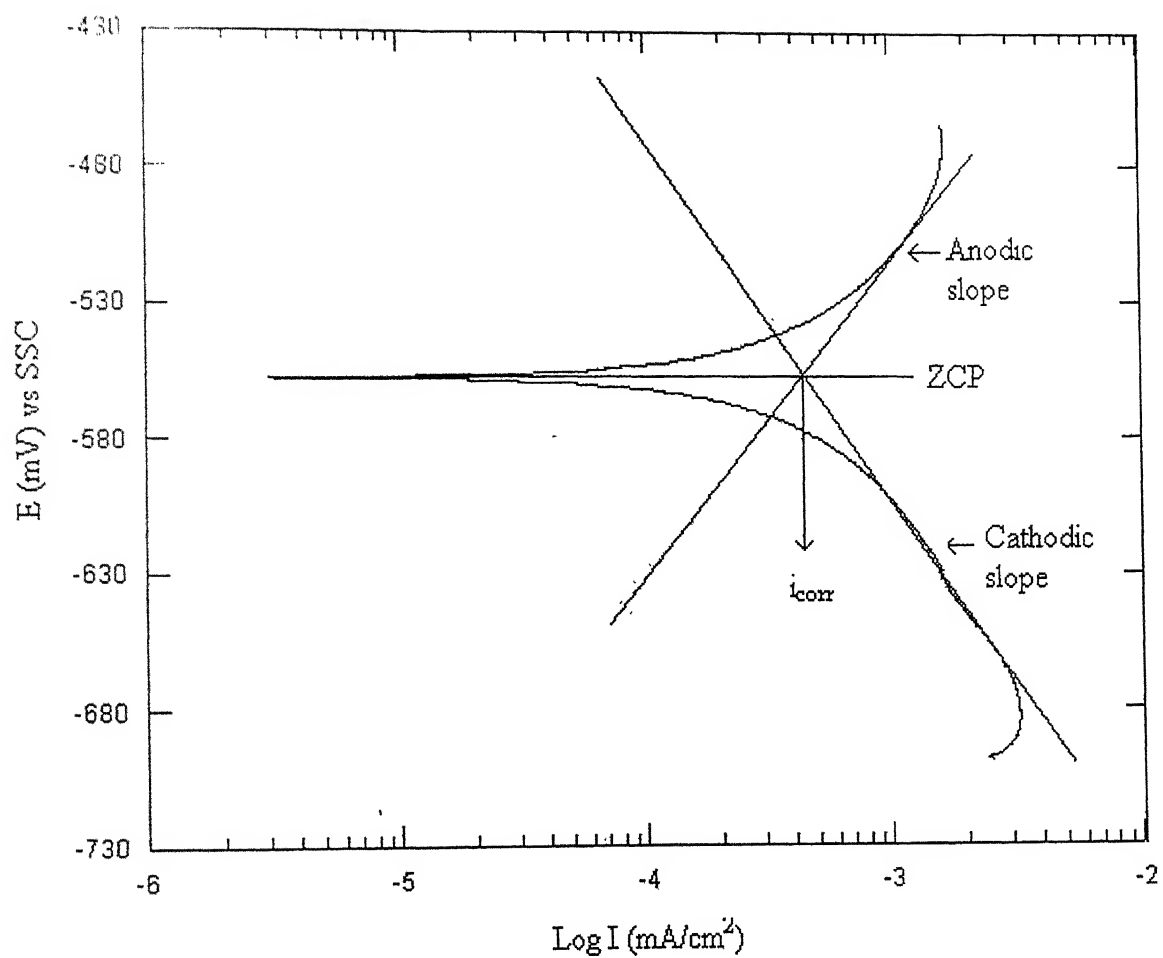


Figure 5.30. Estimation of Tafel slopes and corrosion rate, i_{corr} from the experimental data of the Tafel experiment.

Table 5.5. Tafel extrapolation data for 430L wrought, 434L P/M and 434L P/M composites sintered at 1250°C.

Sample	ZCP (mV vs SSC)	i_{corr} (A/m ²)	β_a (mV/dec)	β_c (mV/dec)	Corrosion rate (mpy)
430(std)	-555	2691	124	-124	1074.77
434L	-531	269	102	-122	135.31
434L+2.5%yttria	-558	389	119	-120	188.09
434L+5%yttria	-555	295	107	-118	152.82
434L+7.5%yttria	-555	360	107	-117	188.94
434L+10%yttria	-559	100	44	-42	48.00

Table 5.6. Tafel extrapolation data for 430L wrought, 434L P/M and 434L P/M composites sintered at 1400°C.

Sample	ZCP (mV vs SSC)	i_{corr} (A/m ²)	β_a (mV/dec)	β_c (mV/dec)	Corrosion rate (mpy)
430(std)	-555	2691	124	-124	1074.77
434L	-568	323	179	-128	140.99
434L+2.5%yttria	-568	251	125	-110	115.10
434L+5%yttria	-564	295	131	-132	142.64
434L+7.5%yttria	-563	350	135	-124	176.72
434L+10%yttria	-553	524	187	-124	251.54

Table 5.7. Tafel extrapolation data for 316L wrought, 316L P/M and 316L P/M composites sintered at 1250°C.

Sample	ZCP (mV vs SSC)	i_{corr} (A/m ²)	β_a (mV/dec)	β_c (mV/dec)	Corrosion rate (mpy)
316L std	-317	6.00	181	-129	2.39
316L	86	7.00	98	-101	3.42
316L+2.5%Y ₂ O ₃	-274	10.00	177	-82	5.00
316L+5%Y ₂ O ₃	-315	15.00	105	-66	7.61
316L+7.5%Y ₂ O ₃	-335	15.00	108	-56	7.63
316L+10%Y ₂ O ₃	-305	8.00	33	-30	4.12

Table 5.8. Tafel extrapolation data for 316L wrought, 316L P/M and 316L P/M composites sintered at 1400°C.

Sample	ZCP (mV vs SSC)	i_{corr} (A/m ²)	β_a (mV/dec)	β_c (mV/dec)	Corrosion rate (mpy)
316L std	-317	6.00	181	-129	2.40
316L	-262	7.00	124	-59	3.27
316L+2.5%Y ₂ O ₃	-333	8.00	81	-46	3.84
316L+5%Y ₂ O ₃	-309	7.00		-52	3.48
316L+7.5%Y ₂ O ₃	-303	8.00	99	-56	4.00
316L+10%Y ₂ O ₃	-270	9.00	88	-33	4.61

Chapter 6

CONCLUSIONS

The microstructural evolution and electrochemical behavior of yttria-dispersed P M austenitic (316L) and ferritic (434L) stainless steels have been studied. Austenitic and ferritic stainless steel samples were compressed in pressures of 200, 300, 400 and 600 MPa. The samples compacted at 600 MPa exhibited higher green density. The compacted samples were sintered by two sintering techniques, namely, normal solid state sintering at 1250°C and supersolidus liquid phase sintering at 1400°C. Based on the sintered densities, it was concluded that the samples compacted at 600 MPa pressure and sintered at 1400°C exhibited better densities than the other samples. At 1400°C, liquid formed within each particle and as a consequence, each particle underwent fragmentation and repacking, giving rise to a homogenous distribution of liquid. This resulted in increased sintering rate and higher sintered density of the sample. Microstructural studies on the samples sintered at two different temperatures indicated better interparticle bonding and emergence of grain boundaries when sintered at 1400°C, which was confirmed by densification results. The sintered densities of ferritic stainless steel samples were higher than the austenitic stainless steel samples. This was attributed to the higher rate of diffusion in 434L when compared to 316L. The effect of yttria content on the sintered density was studied by varying the yttria weight percentage (0, 2.5%, 5%, 7.5% and 10%). Stainless steel-Y₂O₃ composites presented a striking case where similar and dissimilar surfaces are in contact and the migration of atoms and defects are greatly modified due to the contact. The constriction of diffusion across the section for lattice and grain boundary diffusion of atoms has been attributed to the contact. This resulted in the reduction of sintered density of the composites. When the yttria content reached 10-weight % in 434L ferritic stainless steel composite, the sintered density increased drastically. The composites sintered at 1400°C possessed higher sintered density than the samples sintered at 1250°C, which can be attributed to the higher sintering temperature. Microstructural evolution of the samples revealed that, when sintered at 1250°C, yttria segregated at the grain boundaries of the matrix. When sintered at 1400°C, the yttria

dispersoids were dispersed uniformly in the metal matrix. This has been attributed to liquid formation during sintering at 1400°C, which leads to uniform dispersion of yttria.

The electrochemical behavior of the samples in freely-aerated 0.05 mol/l H_2SO_4 at ambient temperature was studied by potentiodynamic polarization, Tafel extrapolation and impedance spectroscopy. The potentiodynamic polarization curves revealed that all the P/M samples exhibited active-passive behavior. From the zero current potentials of the samples, it was concluded that the dominating cathodic reaction was hydrogen evolution. The transpassive region was attributed to oxygen evolution. The range of passivity was not affected by yttria additions. Electrochemical impedance spectroscopy (EIS) was used to study the surface film properties. EIS for 434L P/M ferritic stainless steel sample revealed that the surface film formed on the surface is stable at around the potential of +500 mV vs SSC and hence the i_{pass} values were measured at +500 mV vs SSC. There were no significant changes in the values of ZCP, E_{cp} , E_{p} , E_{bp} , E_{tp} , i_{crit} values for the composites and stainless steel samples. On comparing the austenitic and ferritic P/M stainless steel specimens, the austenitic stainless steel specimens exhibited lower i_{pass} , ZCP and i_{crit} than ferritic samples, which is due to the presence of Ni in the austenitic stainless steel. In the case of stainless steel composites, the corrosion rates for the ferritic stainless steel composites were higher compared to the austenitic stainless steel composites, which has been attributed to the presence of Ni in the austenitic varieties. The addition of yttria dispersoids did not drastically alter the corrosion rates of the composites. The wrought 430L sample exhibited a higher corrosion rate compared to 434L P/M samples because of lower alloying additions of Mo. 316L wrought specimen and the P/M samples possessed similar corrosion rates, thereby indicating that the addition of yttria did not degrade the corrosion resistance. On comparing the effect of sintering temperature on the electrochemical behavior, the samples sintered at 1400°C exhibited lower i_{pass} than the samples sintered at 1250°C. This can be attributed to the lower porosity in the samples sintered at 1400°C.

Reference

- 1) D.A. Jones, Principles and Prevention of Corrosion, Maxwell Macmillan International Editions, NY, 1992.
- 2) I. B. Massalski et al., Binary Alloy Phase Diagrams, 2nd edition, ASM International, Materials Park, OH, 1990.
- 3) W.F. Smith, "Stainless Steel," Structure and Properties of Engineering Alloys, McGraw-Hill Inc., New York, USA, pp. 289-334.
- 4) "Introduction to Stainless Steels," ASM Specialty Handbook: Stainless Steel, J. R. Davis, Davis & Associates (eds.), pp. 4-38.
- 5) "Stainless Steels," *Advanced Materials and Process*, 1998, v.154, n.4, pp. 63-66.
- 6) S.J. Suess, "Corrosion in Stainless Steel," *Advanced Materials Processes*, 1997, v.151, n.4, pp. 27-30.
- 7) "Forms of Corrosion," *Industrial Heating*, 1998, v.12, pp. 140-146.
- 8) K. R. Trethwey and J. Chamberlin, Corrosion For Students of Science and Engineering, John Wiley & Sons, Inc., New York, 1988.
- 9) M.G. Fontana and N.D. Greene, Corrosion Engineering, McGraw-Hill International Book Company, Japan, 2nd edition, 1983.
- 10) H.H. Uhlig and R. Winston Revie, Corrosion and Corrosion Control, A Wiley-Interscience Publications, Canada, 1991.
- 11) W.S. Tait, "An Introduction to Electrochemical Corrosion Testing For Practicing Engineers and Scientists," Pair O Does Publications, Racine, WI, USA, 1994.
- 12) Metals Test Methods and Analytical Procedures, Annual Book of ASTM Standards, v. 3.02, section 3, Philadelphia, PA, USA, 1987.
- 13) R. Baboian and G.S. Haynes, "Cyclic Polarization Measurements-Experimental Procedure and Evolution of Test Data," Electrochemical Corrosion Testing, Eds. F. Mansfeld and U. Bertocci, American Society For Testing and Materials, STP 727, 1981, pp. 274-283.
- 14) E. Klar, P.K. Samal, "Powder Metallurgy Stainless Steels," ASM Handbook, v 7, pp. 174-785.
- 15) F. Thumler and R. Oberacker, An Introduction to Powder Metallurgy, The Institute of Materials, 1993.
- 16) G.S. Upadhyaya, Powder Metallurgy Technology, Pergamon Press, NY, USA, 1965.
- 17) R. M. German, Powder Metallurgy Science, Metal Powder Industrial Federation, Princeton, NJ, USA, 1994.
- 18) From Web <http://www.mpif.org/>
- 19) S. Ghosh, "Processing of Premixed and Prealloyed Bronze Through Transient and Supersolidus Liquid Phase Sintering," M.Tech Thesis, IIT Kanpur, 2001.
- 20) J. S. Hirschhorn, Introduction to Powder Metallurgy, American Powder Metallurgy Institute, Princeton, NJ, USA.
- 21) R. M. German, Sintering Theory and Practice, John Wiley and Sons, Inc., New York, 1996.
- 22) R. M. German, Liquid Phase Sintering, Plenum Press, NY, 1985.

- 23) J.W. Huppmann, H. Riegger, W.A. Kaysser, V. Smolej and S. Pejovnik, "Elementary Mechanisms of Liquid Phase Sintering," *Sonderdruck aus Zeitschrift für Metallkunde*, 1979, Band 70, H. 11, pp. 707-713.
- 24) R. Tandon, "Densification Mechanisms and Microstructural Evolution Leading to High Density Processing of Prealloyed Powders in Supersolidus Liquid Phase Sintering," PhD Thesis, The Pennsylvania State University, USA, 1995.
- 25) R.M. German, "Supersolidus Liquid Phase Sintering; Part I: Process Review," *International Journal of Powder Metallurgy*, 1990, vol. 26, pp. 23-33.
- 26) R.M. German, "Quantitative Theory for Supersolidus Liquid Phase Sintering," *Powder Metallurgy*, 1991, vol. 34, pp. 101-107.
- 27) J.A. Lund and S.R. Bala, "Supersolidus Sintering," *Modern Developments in Powder Metallurgy*, H.H. Hausner and W.E. Smith (eds.), Metal Powder Industries Federation, Princeton, NJ, 1974, vol. 6, pp. 409-421.
- 28) A. Lal, "Mechanisms and Mechanics of Shape Loss During Supersolidus Liquid Phase Sintering," PhD Thesis, The Pennsylvania State University, USA, 1999.
- 29) E.J. Westerman, "Sintering of Ni-based Superalloys," *Metallurgical Society of AMIE*, 1962, vol. 224, pp.159-164.
- 30) R. Tandon and R.M. German, "Supersolidus-Transient Liquid Phase Sintering Using Superalloy Powders," *International Journal of Powder Metallurgy*, 1994, vol. 30, pp.435-443.
- 31) A. Lal, "Homogenization, Densification, and Brazing Using Supersolidus Liquids Formed in Nickel-base Alloy Powder Mixtures," MS Thesis, The Pennsylvania State University, US, 1996.
- 32) A. Lal, R. Iacocca and R.M. German, "Densification During Supersolidus Liquid Phase Sintering of Nickel-base Prealloyed Powder Mixtures," *Materials and Metallurgical Transactions A: Physical Metallurgy and Material Science*, 1999, vol. 30, n. 8, pp. 2201-2208.
- 33) R.M. German, "Advances in High Alloy Sintering Using Supersolidus Liquids," *Advances in Powder Metallurgy and Particulate Materials*, 1997, vol. 2, pp. 14-3-14-8.
- 34) Y. Liu, R. Tandon and R.M. German, "Modeling of Supersolidus Liquid Phase Sintering: I. Capillary Force," *Metallurgical and Materials Transactions A: Physical Metallurgy and Materials Science*, 1995, vol. 26, n. 9, pp. 2415-2422.
- 35) Y. Liu, R. Tandon and R.M. German, "Modeling of Supersolidus Liquid Phase Sintering: II. Densification," *Metallurgical and Materials Transactions A: Physical Metallurgy and Materials Science*, 1995, vol. 26, n. 9, pp. 2423-2430.
- 36) From Web <http://www.mpif.org/industry/2001-10.html>.
- 37) E. Klar, Powder Metallurgy – Applications, Advantages and Limitations, American Society For Metals, Metals Park, OH, USA, 1983.
- 38) "Metallography of Powder Metallurgical Materials," ASM Handbook, v 7, pp.728.
- 39) B. Shaw, "Corrosion Resistant Powder Metallurgy Alloys," ASM Handbook, v. 7, pp. 978-1005.
- 40) D. Itzhak and E. Aghion, "Corrosion Behavior of Hot-Pressed Austenitic Stainless Steel in H₂SO₄ Solutions at Room Temperatures," *Corrosion Science*, 1983, vol. 23, N. 10, pp. 185-1094.

- 41) J. Maahn and T. Mathiesen, "Corrosion Properties of Sintered Stainless Steel," *UK Corrosion Proceedings*, Institute of Corrosion, 1991, vol. 2, pp. 1-15.
- 42) A. Tiziani, A. Molinari, L. Fedrizzi, A. Tomasi, and P.L. Bonora, "Liquid Phase Sintering of AISI 316L Stainless Steel," *Powder Metallurgy*, 1989, vol.32, n.2, pp.118-122.
- 43) W.J. Wang and Y.L. Su, "Liquid Phase Sintering of Austenitic Stainless Steel Powders with Silicon Additives," *Powder Metallurgy*, 1986, vol.29, n.4, pp.269-275.
- 44) R.M. German, "The Production of Stainless Steels by Injection Moulding Water Atomised Prealloy Powders," *Journal Injection Moulding Technique*, 1997, vol.1, n.3, pp. 171-179.
- 45) A. Sharon, N. Melman, and D. Itzhak, "Corrosion Resistance of Sintered Stainless Steel Containing Nickel Based Additives," *Powder Metallurgy*, 1994, v.37, n.4, pp.67-71.
- 46) G. Lei, R.M. German, and H.S. Nayar, "Corrosion Control in Sintered Austenitic Stainless Steel," pp.391-405.
- 47) H.S. Nayar, R.M. German, and W.R. Johnson, "The effect of Sintering on Corrosion Resistance of 316 Stainless Steel," pp.255-265.
- 48) D.H. Ro and E. Klar, "Corrosion Behavior of P/M Austenitic Stainless Steel," pp.1-38.
- 49) R. Tandon, J. W. Simmons, B. S. Covino, and J. H. Russel, "Mechanical And Corrosion Properties of Nitrogen- Alloyed Stainless Steel Consolidated by MIM," *International Journal Powder Metallurgy*, 1998, vol.34, n.8, pp. 47-54.
- 50) R.H. Shay, T.L. Ellison, K.R. Berger, "Control of Nitrogen Absorption and Surface Oxidation of Austenitic Stainless Steels in H₂-N₂ Atmospheres," pp.411-430.
- 51) T. Tunberg and L. Nyborg, "Surface Reactions During Water Atomization and Sintering of Austenitic Stainless Steel Powder," *Powder Metallurgy*, 1995, vol.38, n.2, pp. 121-130.
- 52) D.C. Smith, "The Material Property Response to Variation in the Sintering Atmosphere of Stainless Steel," MS Thesis, The Pennsylvania State University, USA, 1998.
- 53) G.H. Lei and R.M. German, "Corrosion of Sintered Stainless Steels in Sodium Chloride Solutions," Modern Developments in Powder Metallurgy, v.16, E.N. Aqua and C.I. Whitman (eds.), Metal Powder Industries Federation, Princeton, NJ, USA, 1984, pp. 261-266.
- 54) E. Otero, A. Pardo, E. Saenz, M.V. Utrilla, and F.J. Perez, "Corrosion Resistance of Sintered Austenitic Stainless Steels in Boiling Nitric Acid," *Canadian Metallurgical Quarterly*, 1997, v.36, n.1, pp.65-72.
- 55) E. Otero, A. Pardo, E. Saenz, M.V. Utrilla, and F.J. Perez, "Corrosion Behavior of AISI 304L and 316L Stainless Steels Prepared by Powder Metallurgy in the Presence of Sulfuric and Phosphoric Acid," *Corrosion Science*, 1998, vol.40, n.8, pp.1421-1434.
- 56) E. Otero, A. Pardo, E. Saenz, M.V. Utrilla, and F.J. Perez, "Influence of Microstructure on the Corrosion Resistance of AISI Type 304L and 316L

- Sintered Stainless Steels Exposed to Ferric Chloride Solution," *Materials Characterization*, 1995, vol.35, pp.145-151.
- 57) D.R. Gabe, "Corrosion and Protection of Sintered Metal Parts," *Powder Metallurgy*, 1977, n.4, pp.227-231.
 - 58) I. Fedrizzi, A. Molinari, F. Deflorian, A. Tiziani and P.L. Bonora, "Corrosion Resistance of Sintered Austenitic Stainless Steel,"
 - 59) F. Ahlberg, P. Engdahl and R. Johansson, "An Electrochemical Investigation on the Corrosion Behavior of Sintered Stainless Steels," International Conference of Powder Metallurgy, Wembley Conference Centre, London, UK, vol. 1, July 1990, pp. 419-433.
 - 60) K.H. Moyer, F.W. Winter, H. Dahlgren, and W. Ziegler, "An Alternative Solution to Obtaining Ferritic Stainless Steel P/M Parts With Exceptional Magnetic Properties and Corrosion Resistance," International Conference of Powder Metallurgy, Wembley Conference Centre, London, UK, vol. 1, July 1990, pp. .
 - 61) D. Yuan, J.R. Spirko, and H.I. Sanderow, "Calorimetric Corrosion Testing of P/M Stainless Steel," *International Journal Powder Metallurgy*, 1997, v.33, n.2, pp. 41-49.
 - 62) S. Lal, "Sintering of 316L Austenitic Stainless Steel-Y₂O₃ Particulate Composites," PhD Thesis, Indian Institute of Technology, Kanpur, 1988.
 - 63) S. Lal and G.S. Upadhyaya, "Sintering of Stainless Steel and Their Based Composites," *Review on Powder Metallurgy and Physical Ceramics*, 1986, vol. 3, No. 2, pp. 165-203.
 - 64) S. Lal and G.S. Upadhyaya, "Effect of Y₂O₃ Addition and Sintering Period on the Properties of P/M 316L Austenitic Stainless Steel," *Journal of Materials Science Letters*, 1987, vol. 6, pp. 761-764.
 - 65) S.N. Patankar and M.J. Tan, "Role of Reinforcement in Sintering of SiC/316L Stainless Steel Composite," *Powder Metallurgy*, 2000, vol. 43, no. 4, pp. 350-352.
 - 66) S.K. Mukherjee, "Sintering of 434L Ferritic Stainless Steel-Al₂O₃ Particulate Composites," PhD Thesis, Indian Institute of Technology, Kanpur, 1984.
 - 67) S.K. Mukherjee and G.S. Upadhyaya, "Sintering of 434L Ferritic Stainless Steel Containing Al₂O₃ Particles," *International Journal of Powder Metallurgy and Powder Technology*, 1983, vol. 19, pp.289.
 - 68) S.K. Mukherjee and G.S. Upadhyaya, "Sintering of Ferritic Stainless Steel-Al₂O₃ Particulate Composites," *Journal of Powder and Bulk Solid technology*, 1983, vol. 7, pp. 27.
 - 69) S.K. Mukherjee and G.S. Upadhyaya, "Sintered 434L Ferritic Stainless Steel-Al₂O₃ Particulate Composites Containing Phosphorous," *High Temperature Technology*, 1983, vol. 1, pp. 223.

Appendix I

316L sintered at 1250°C

Compact Pressure (MPa)	Type	Weight (g)	Height (mm)	Diameter (mm)	Density (g/cm ³)	Weight loss (%)	Densification Parameter
200	Green	4.8932	7.50	12.70	5.15 (64.7)	0.54	0.10
	Sintered	4.8668	7.36	12.36	5.42 (68.2)		
300	Green	3.9678	5.80	12.70	5.40 (68.2)	0.53	0.07
	Sintered	3.9467	5.70	12.56	5.40 (67.8)		
400	Green	3.0641	4.30	12.70	5.62 (70.6)	0.54	0.09
	Sintered	3.0475	4.24	12.54	5.82 (73.1)		
600	Green	6.3818	8.00	12.70	6.19 (77.8)	0.69	0.11
	Sintered	6.2790	7.84	12.60	6.38 (80.1)		

316L sintered at 1400°C

Compact Pressure (MPa)	Type	Weight (g)	Height (mm)	Diameter (mm)	Density (g/cm ³)	Weight loss (%)	Densification Parameter
200	Green	4.1679	6.34	12.70	5.19 (65.2)	0.22	0.18
	Sintered	4.1589	6.10	12.34	5.70 (71.7)		
300	Green	3.9196	5.5	12.70	5.63 (70.7)	0.04	0.34
	Sintered	3.9180	5.3	12.10	6.43 (80.8)		
400	Green	4.2533	5.74	12.70	5.85 (73.5)	0.19	0.43
	Sintered	4.2453	5.46	12.10	6.77 (85.0)		
600	Green	4.5273	5.78	12.70	6.19 (77.7)	0.23	0.48
	Sintered	4.5170	5.5	12.20	7.03 (88.3)		

Appendix II

434L sintered at 1250°C

Compact Pressure (MPa)	Type	Weight (g)	Height (mm)	Diameter (mm)	Density (g/cm ³)	Weight loss (%)	Densification Parameter
200	Green	5.5705	8.90	12.70	5.07 (63.6)	0.45	0.26
	Sintered	5.6847	8.66	12.00	5.81 (72.9)		
300	Green	3.9566	5.80	12.70	5.39 (67.7)	0.43	0.24
	Sintered	3.9697	5.70	12.10	6.01 (75.5)		
400	Green	6.0552	8.50	12.70	5.63 (70.7)	0.49	0.22
	Sintered	6.0258	8.40	12.20	6.14 (77.1)		
600	Green	6.7334	8.70	12.70	6.11 (76.7)	0.52	0.21
	Sintered	6.6981	8.68	12.30	6.50 (81.6)		

434L sintered at 1400°C

Compact Pressure (MPa)	Type	Weight (g)	Height (mm)	Diameter (mm)	Density (g/cm ³)	Weight loss (%)	Densification Parameter
200	Green	3.2538	5.32	12.70	4.83 (60.7)	0.68	0.10
	Sintered	3.2318	5.20	12.40	5.15 (64.7)		
300	Green	2.4091	3.70	12.70	5.14 (64.6)	1.12	0.46
	Sintered	2.3822	3.44	11.70	6.44 (81.0)		
400	Green	3.5064	5.00	12.70	5.54 (69.6)	1.02	0.55
	Sintered	3.4706	4.70	11.70	6.87 (86.3)		
600	Green	3.4312	4.54	12.70	5.97 (75.0)	0.99	0.55
	Sintered	3.3972	4.30	11.94	7.06 (88.7)		

Appendix III

316L + Y₂O₃ sintered at 1250°C

Y ₂ O ₃ composition	Type	Weight (g)	Height (mm)	Diameter (mm)	Density (g/cm ³)	Weight loss (%)	Densification Parameter
0%	Green	3.9472	5.00	12.70	6.24 (78.3)	1.04	0.15
	Sintered	3.9062	4.90	12.50	6.50 (81.6)		
2.5%	Green	3.2500	4.22	12.70	6.08 (77.2)	0.34	0.14
	Sintered	3.2389	4.12	12.56	6.35 (80.6)		
5%	Green	3.1055	4.10	12.70	5.98 (76.6)	0.94	0.14
	Sintered	3.0762	3.94	12.60	6.26 (80.2)		
7.5%	Green	4.0440	5.24	12.70	6.10 (78.9)	0.87	0.08
	Sintered	4.0088	5.10	12.66	6.25 (80.8)		
10%	Green	3.9520	5.16	12.70	6.05 (79.0)	0.84	0.07
	Sintered	3.9188	5.04	12.66	6.18 (80.7)		

316L + Y₂O₃ sintered at 1400°C

Y ₂ O ₃ composition	Type	Weight (g)	Height (mm)	Diameter (mm)	Density (g/cm ³)	Weight loss (%)	Densification Parameter
0%	Green	3.2214	4.24	12.70	6.00 (75.4)	0.54	0.41
	Sintered	3.2040	4.00	12.24	6.81 (85.6)		
2.5%	Green	3.2365	4.24	12.70	6.03 (76.5)	0.57	0.31
	Sintered	3.2180	4.02	12.40	6.63 (84.2)		
5%	Green	3.2358	4.30	12.70	5.94 (76.1)	0.42	0.22
	Sintered	3.2221	4.12	12.48	6.40 (81.9)		
7.5%	Green	2.5230	3.40	12.70	5.86 (75.8)	0.21	0.23
	Sintered	2.5178	3.20	12.56	6.35 (82.2)		
10%	Green	3.1989	4.20	12.70	6.02 (78.5)	0.03	0.09
	Sintered	3.1981	4.14	12.60	6.20 (80.9)		

Appendix IV

434L + Y₂O₃ sintered at 1250°C

Y ₂ O ₃ composition	Type	Weight (g)	Height (mm)	Diameter (mm)	Density (g/cm ³)	Weight loss (%)	Densification Parameter
0%	Green	3.1881	4.19	12.70	6.01 (75.6)	1.01	0.25
	Sintered	3.1560	4.08	12.32	6.49 (81.6)		
2.5%	Green	2.4742	3.40	12.70	5.75 (72.9)	0.93	0.16
	Sintered	2.4512	3.28	12.50	6.09 (77.3)		
5%	Green	3.5078	4.70	12.70	5.89 (75.5)	0.89	0.15
	Sintered	3.4767	4.50	12.60	6.20 (79.4)		
7.5%	Green	4.2978	5.80	12.70	5.85 (75.7)	0.82	0.05
	Sintered	4.2626	5.70	12.64	5.96 (77.1)		
10%	Green	4.3481	5.90	12.70	5.82 (76.0)	0.86	0.36
	Sintered	4.3108	5.50	12.30	6.60 (86.2)		

434L+Y₂O₃ sintered at 1400°C

Y ₂ O ₃ composition	Type	Weight (g)	Height (mm)	Diameter (mm)	Density (g/cm ³)	Weight loss (%)	Densification Parameter
0%	Green	3.5200	4.80	12.70	5.79 (72.8)	0.96	0.55
	Sintered	4.4863	4.50	11.88	6.99 (87.8)		
2.5%	Green	3.2048	4.42	12.70	5.73 (72.7)	0.85	0.49
	Sintered	3.1775	4.12	12.00	6.82 (86.6)		
5%	Green	3.3790	4.58	12.70	5.83 (74.6)	0.80	0.29
	Sintered	3.3519	4.38	12.36	6.38 (81.7)		
7.5%	Green	3.3671	4.62	12.70	5.76 (74.5)	0.64	0.18
	Sintered	3.3457	4.44	12.50	6.14 (79.5)		
10%	Green	2.9980	4.14	12.70	5.72 (74.7)	0.56	0.13
	Sintered	2.9812	4.00	12.56	6.02 (78.6)		

Appendix V

316L stainless steel

Temperature (°C)	Compaction Pressure (MPa)		Height (mm)	Diameter (mm)	Axial shrinkage(%)	Radial shrinkage(%)
1250	200	Green	7.5	12.7	1.87	1.89
		Sintered	7.36	12.46		
	300	Green	5.8	12.7	1.72	1.10
		Sintered	5.7	12.56		
	400	Green	4.3	12.7	1.40	1.26
		Sintered	4.24	12.54		
	600	Green	8	12.7	2.00	0.79
		Sintered	7.84	12.6		
1400	200	Green	6.34	12.7	3.79	2.83
		Sintered	6.1	12.34		
	300	Green	5.5	12.7	3.64	4.72
		Sintered	5.3	12.1		
	400	Green	5.74	12.7	4.88	4.72
		Sintered	5.46	12.1		
	600	Green	5.78	12.7	4.84	3.94
		Sintered	5.5	12.2		

434L stainless steel

Temperature (°C)	Compaction Pressure (MPa)		Height (mm)	Diameter (mm)	Axial shrinkage(%)	Radial shrinkage(%)
1250	200	Green	8.9	12.7	2.70	5.51
		Sintered	8.66	12.0		
	300	Green	5.8	12.7	1.72	4.72
		Sintered	5.7	12.1		
	400	Green	8.5	12.7	1.18	3.94
		Sintered	8.4	12.2		
	600	Green	8.7	12.7	0.23	3.15
		Sintered	8.68	12.3		
1400	200	Green	5.32	12.7	2.26	2.36
		Sintered	5.2	12.4		
	300	Green	3.7	12.7	7.03	7.87
		Sintered	3.44	11.7		
	400	Green	5	12.7	6.00	7.87
		Sintered	4.7	11.7		
	600	Green	4.54	12.7	5.29	5.98
		Sintered	4.3	11.94		

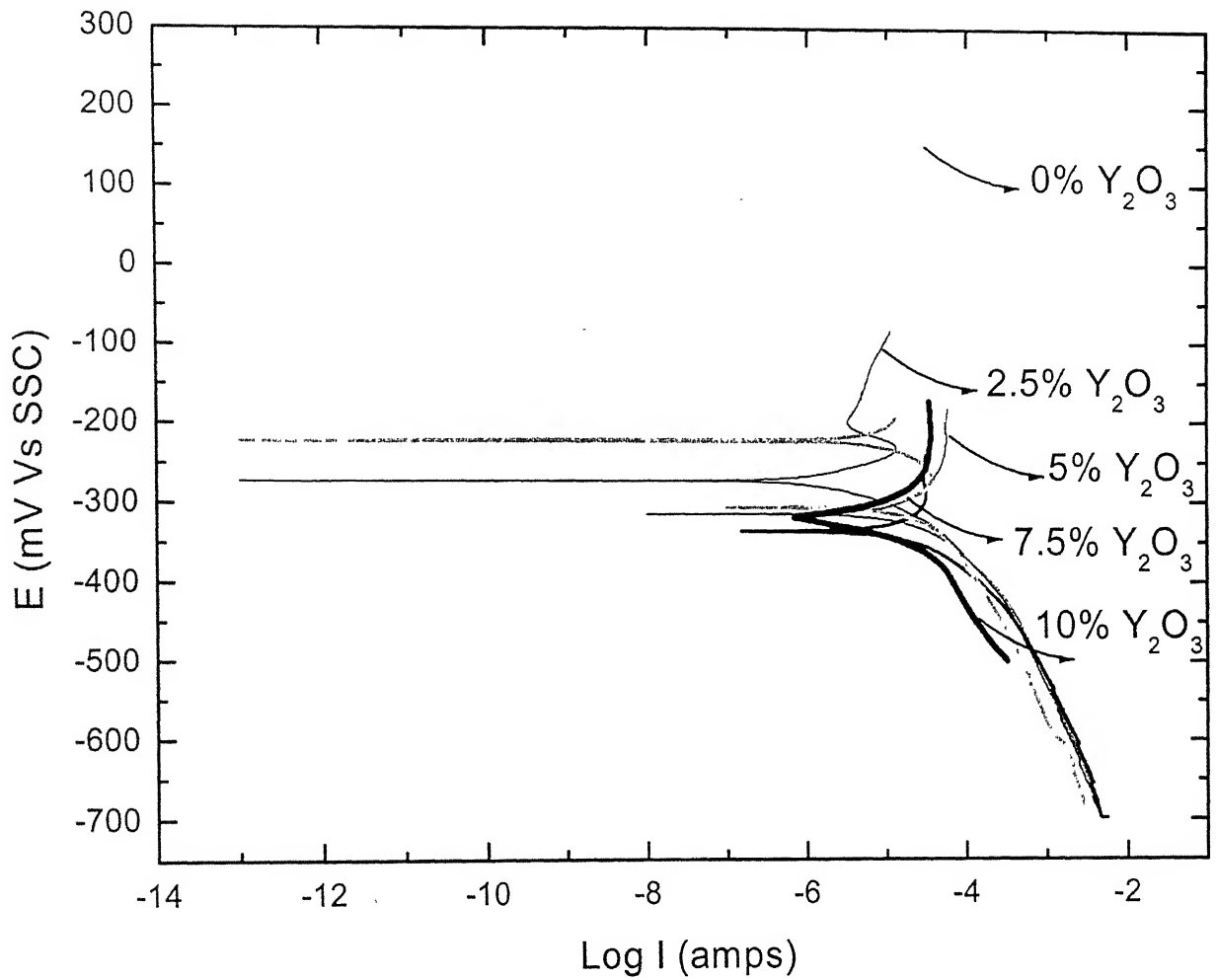
316L stainless steel composites

Temperature (°C)	Ytria percentage		Height (mm)	Diameter (mm)	Axial shrinkage(%)	Radial shrinkage(%)
1250	0	Green	5.00	12.7	2.00	1.57
		Sintered	4.9	12.5		
	2.5	Green	4.22	12.7	2.37	1.10
		Sintered	4.12	12.56		
	5	Green	4.10	12.7	3.9	0.79
		Sintered	3.94	12.6		
	7.5	Green	5.24	12.7	2.67	0.31
		Sintered	5.10	12.66		
	10	Green	5.16	12.7	2.33	0.31
		Sintered	5.04	12.66		
1400	0	Green	4.24	12.7	5.66	3.62
		Sintered	4.00	12.24		
	2.5	Green	4.24	12.7	5.19	2.36
		Sintered	4.02	12.4		
	5	Green	4.3	12.7	4.19	1.73
		Sintered	4.12	12.48		
	7.5	Green	3.4	12.7	5.88	1.10
		Sintered	3.2	12.56		
	10	Green	4.2	12.7	1.43	0.79
		Sintered	4.14	12.6		

434L Stainless steel compsites

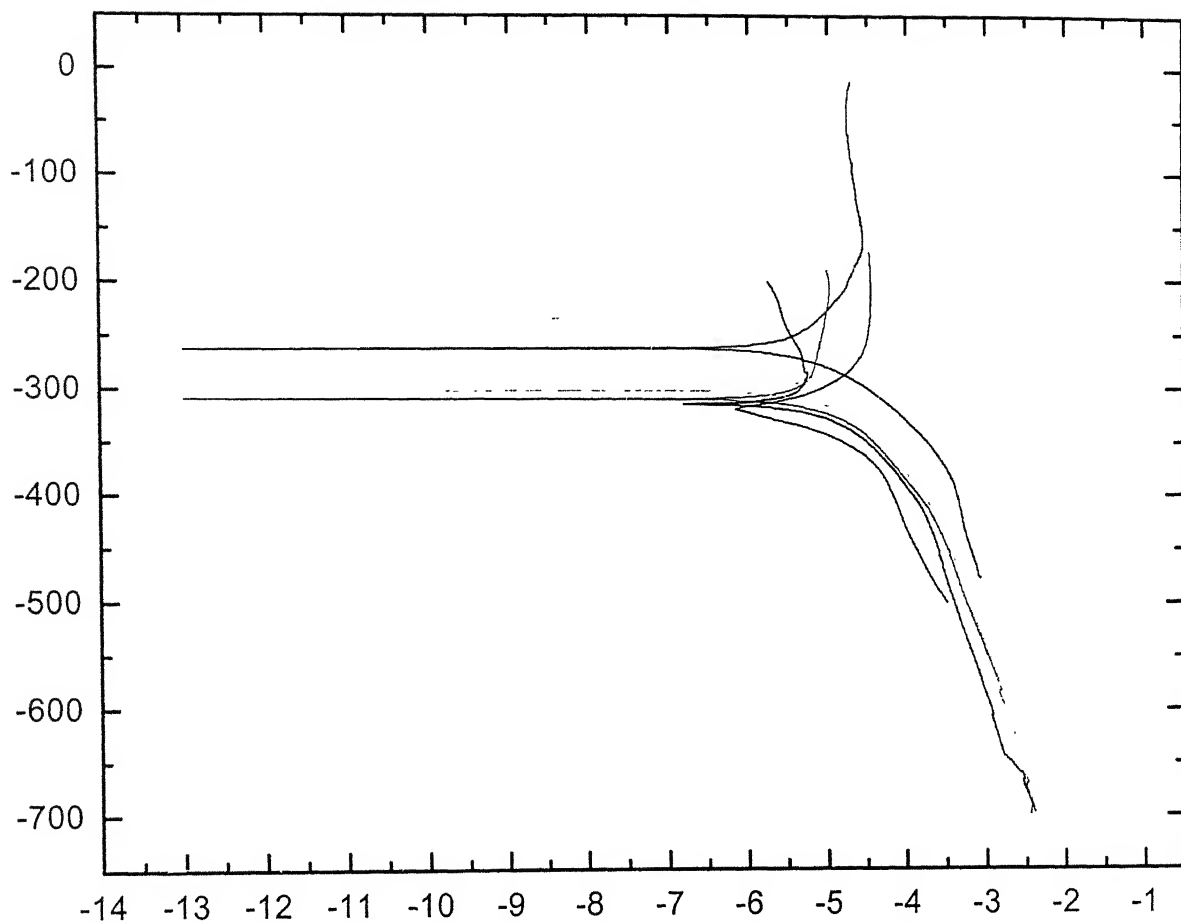
Temperature (°C)	Ytria percentage		Height (mm)	Diameter (mm)	Axial shrinkage(%)	Radial shrinkage(%)
1250	0	Green	4.19	12.70	2.63	2.99
		Sintered	4.08	12.32		
	2.5	Green	3.40	12.70	3.53	1.57
		Sintered	3.28	12.50		
	5	Green	4.70	12.70	4.26	0.79
		Sintered	4.50	12.60		
	7.5	Green	5.80	12.70	1.72	0.47
		Sintered	5.70	12.64		
	10	Green	5.90	12.70	6.78	3.15
		Sintered	5.50	12.30		
1400	0	Green	4.80	12.70	6.25	6.46
		Sintered	4.50	11.88		
	2.5	Green	4.42	12.70	6.79	5.51
		Sintered	4.12	12.00		
	5	Green	4.58	12.70	4.37	2.68
		Sintered	4.38	12.36		
	7.5	Green	4.62	12.70	3.90	1.57
		Sintered	4.44	12.50		
	10	Green	4.14	12.70	3.38	1.10
		Sintered	4.00	12.56		

Appendix VI



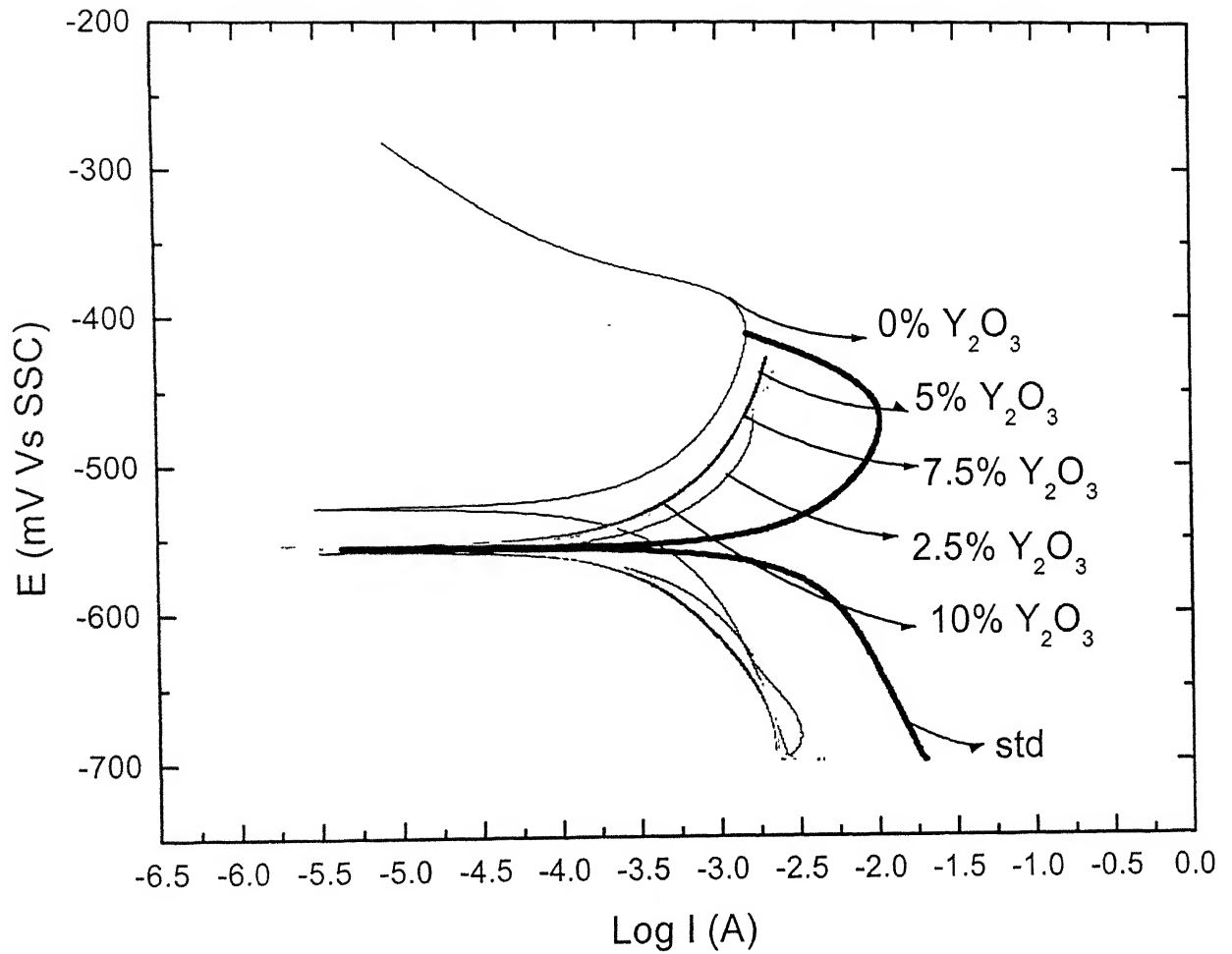
Tafel curves for 316L stainless steel composites sintered at 1250°C compacted at a pressure of 600MPa.

Appendix VII



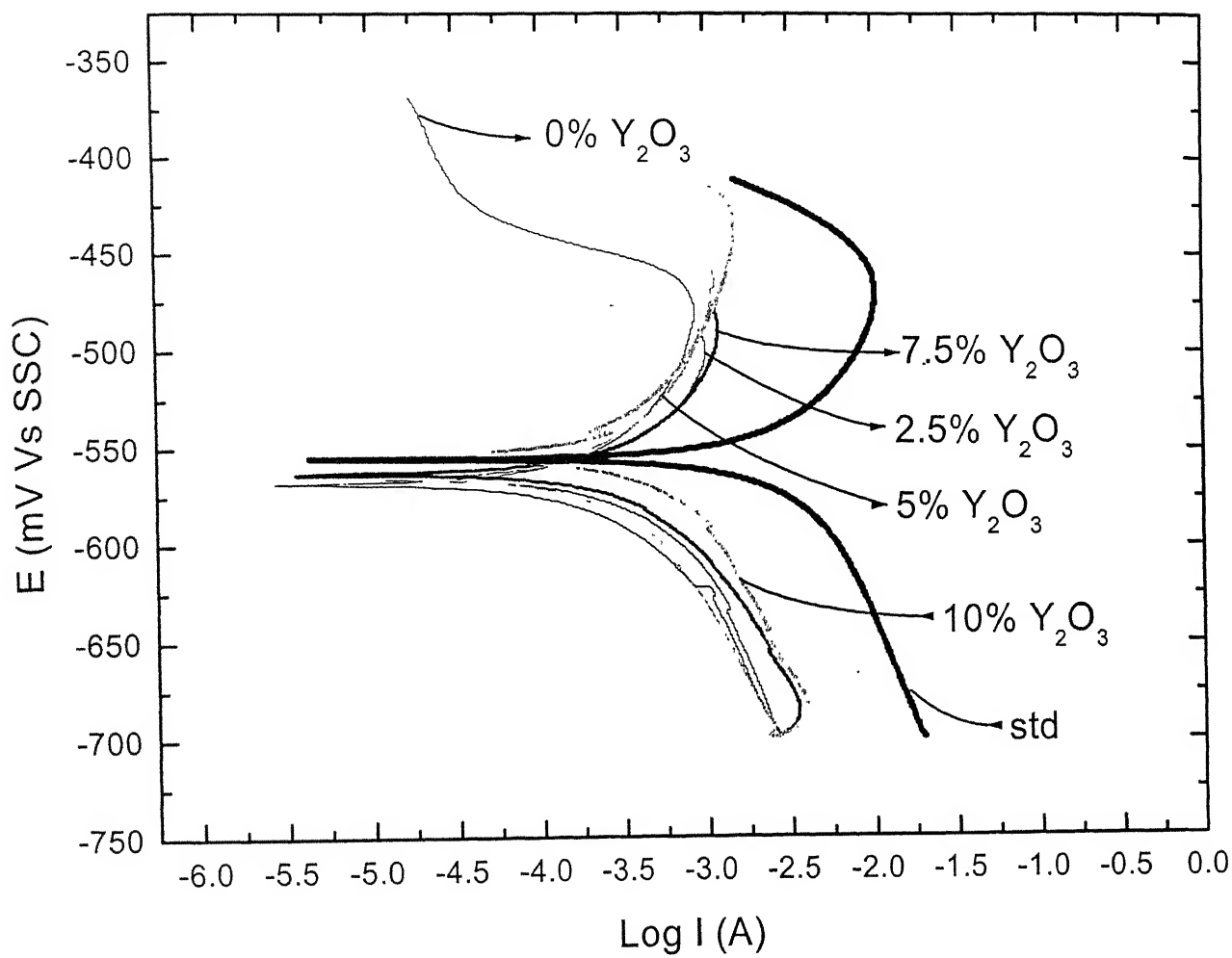
Tafel curves for 316L stainless steel composites sintered at 1400°C compacted at a pressure of 600 MPa.

Appendix VIII



Tafel curves for 434L stainless steel composites sintered at 1250°C compacted at 600 MPa pressure.

Appendix IX



Tafel curves for 434L stainless steel composites sintered at 1400°C compacted at 600 MPa pressure.

A

141869



A141869